In Vitro Investigation of Cell-Free Layer Formation in Microchannels: Dependency on the Red Blood Cell Aggregation and Field of Shear

Omemah Rajab Gliah

Thesis submitted

in partial fulfillment of the requirements for the

Doctorate in Philosophy degree in Chemical Engineering

Department of Chemical and Biological Engineering

Faculty of Engineering

University of Ottawa

Statement of Ethics Approval

The research involves human subjects. The experimental work was done in compliance with the ethics committee of the University of Ottawa. File #: H11-13-06.

Abstract

Red blood cells (RBCs) form approximately 40 to 45% of the human blood volume, and their behaviour and characteristics are the main determinant of blood properties, such as viscosity. RBCs are deformable species and stack together under low shear rate to form aggregates or rouleaux. Flowing RBCs migrate away from the wall leaving a cell-depleted layer known as the cell-free layer (CFL). This layer contributes to the blood viscosity and exchange between the RBCs and the target cells: a thinner CFL enhances the exchange process by reducing the diffusion distance. The formation of this CFL, however, is not yet completely understood.

The goal of this study is to improve the understanding of the formation of the CFL in the micro-flow. This was accomplished by studying the effects of changing both the flow rate and the microchannel geometry on blood flow in microchannels.

In this work, 10% hematocrit human blood suspensions were prepared in native plasma and flowed through poly-dimethylsiloxane (PDMS) microchannels of 100 µm x 34 µm cross-section. Investigation of the flowing cells was performed by using micro particle image velocimetry (µPIV) coupled with a high-speed camera. First, the high-speed camera images were processed with customized Matlab programs to detect and measure the CFL thickness and the RBC aggregates sizes. Second, the blood flow velocity profiles were measured using µPIV in order to determine the actual flow rate, the RBCs' centerline velocity, and the shear rate.

The results showed that the increase in both flow rate and shear rate significantly reduced the CFL thickness and RBC aggregates size. Comparison of the upstream and downstream measurements in the bifurcating microchannel showed that the change in microchannel geometry did not significantly influence CFL thickness and RBC aggregate size, while within the daughter branches, RBCs tended to flow close to the inner wall resulting in an undetectable CFL at the inner wall and in a larger CFL at the outer wall of the branch. These *in vitro* results quantitatively relate CFL thickness and RBC aggregate size at different shear rates. The findings are of immediate interest regarding the understanding of microcirculation and improved designs of microchips.

Keywords:

Microcirculation, microfluidics, blood, non-Newtonian fluid, flow rate, velocity, wall shear rate, micro particle image velocimetry (µPIV), high-speed camera.

Acknowledgements

I thank all those who contributed to the success of this research and made it a valuable source to enhance the knowledge in the fields of blood rheology and microfluidics.

First, I would like to thank my supervisor Dr. Marianne Fenech for her professional guidance over the years. She was always available to answer my inquiries and overcome the obstacles I encountered throughout this experimental journey. I would like to deeply thank Dr. Fenech's research group for their collaborative environment. I would like to sincerely thank Dr. Michel Labrosse for his generous cooperation and supervision. I would like thank Dr. Rym Mehri and Dr. Laura Haya for their comments and valuable discussions. I would like to express my thanks to the University of Ottawa machine shop staff, especially Leo Denner for his technical support throughout my experimental work. I would like to present my special thanks to Carleton University microfabrication laboratory staff Angela McCormick and Rob Vandusen for the fabrication of the microchannels mold.

I also would like to express my gratitude to my husband Amen Shkab and lovely kids (Retaj, Sadeq, Rua, Rana, and Rahaf) for their support and patience along all the years of my post graduate studies. I would like to present my gratitude, appreciation and respect to my parents Mr. Rajab Gliah and Mrs. Zainab Huwaidy, who encouraged me to pursue my studies and go forward.

Finally, thanks to the Libyan Ministry of High Education and Scientific Research for granting me a post graduate scholarship. Also, thanks to the Natural Sciences and Engineering Research Council of Canada (NSERC) for the research funding, the Canadian Foundation for Innovation (CFI) and Ontario Research Funds (ORF) for the experimental infrastructure funding.

Table of Contents

List of Figures

List of Tables

List of Symbols

Symbol	Definition
A	Cross-sectional area of the microchannel (μm^2)
AI	Aggregation index
$\Phi(m, n)$	Cross-correlation function
dp	Diameter of the fluorescent particle (μm)
D_h	Hydraulic diameter (μm)
dt	Time between two frames (s)
$F(y, z)$	Expected 3D velocity profile (mm/s)
G	Pressure drop (Pa/m or $kg/m^2.s^2$)
h	Depth of microchannel (μm)
H	Hematocrit (%)
$I(x, y)_{binary}$	Binary image intensity
$I(x, y)_{min}$	Minimum image intensity
$I(x, y, t)_{original}$	Original Image intensity
k	Shape factor of the velocity profile
l	Length of the microchannel (mm)
M	Magnification
n	Index of refraction
NA	Numerical aperture
P	Aggregate perimeter (μm)
Q	Flow rate in the channel (μL/hr)
Q_{prog}	Programmed flow rate by the pump (μL/hr)
Q_{calc}	Calculated flow rate (μL/hr)
R^2	Coefficient of determination or R-squared
Re	Reynold number
r	Cell radius (μm)
T	Threshold
u	Velocity (mm/s)
u_{ave}	Average velocity (mm/s)
$u_{\max}$	Maximum velocity (mm/s)
$u(y, z)$	Theoretical 3D velocity profile (mm/s)
w	Width of the microchannel (μm)
x	Position along the channel length (μm)
y	Position across the channel width (μm)
z	Position across the channel depth (μm)
γ	Shear rate (s^{-1})
γ_w	Wall shear rate (s^{-1})
μ	viscosity of blood (Pa.s or kg/m.s)
ρ	Density of blood (kg/m^3)
τ	Shear stress (Pa or $kg/m.s^2$)
λ	Wave length (nm)
ε	Minimal intensity (%)

List of Abbreviations

Abbreviation	Definition
ASP	Aggregation Shape Parameter
CCD	Charged Coupled Device
CFL	Cell-Free Layer
DOC	Depth of Correlation
DI	Deionized Water
ESR	Erythrocyte Sedimentation Rate
MAI	Microscopic Aggregation Index
NO	Nitric Oxide
O_2	Oxygen
PBS	Phosphate Buffered Saline
PDMS	Poly-dimethylsiloxane
PIV	Particle Image Velocimetry
RBCs	Red Blood Cells
WBCs	White Blood Cells
2D	Two-Dimensional
3D	Three-Dimensional
µPIV	Micro Particle Image Velocimetry

Chapter 1

Introduction

1.1 Motivation

Understanding blood flow behaviour is of great interest towards biomedical and biofluids applications, as well as in the fields of hemorheology and hemodynamics. The main function of blood in the body is the delivery of oxygen and nutrients as well as the removal of waste, such as carbon dioxide and urea. It consists mainly of red blood cells (RBCs), white blood cells (WBCs), platelets and plasma, with RBCs occupying 40- 45% of the blood volume. Due to its complex composition, blood is considered one of the most challenging fluids to study and understand [1].

As RBCs are the most abundant of the blood cells, they have a significant influence on the rheological properties of blood. Normal RBCs deform, enabling them to pass through very small blood vessels with diameters even smaller than those of the RBCs themselves. They also tend to stack in two or three dimensions forming aggregates or rouleaux. In blood circulation, RBCs tend to migrate away from the vessel wall toward the centerline, leaving a cell-depleted region known as cell-free layer (CFL). The CFL is known to influence blood rheological properties as well as some physiological processes [2]. Its influence is more pronounced at the microcirculation level. The CFL decreases the local viscosity and lowers the flow resistance [3]. As the CFL is located between the RBC core and the vessel wall where molecules are exchanged between the blood and body tissues, this CFL influences molecular exchange processes such as oxygen delivery and carbon dioxide and nitric oxide removal.

The flow rate is a key factor governing the blood flow by changing the local shear rates. Shear rate (defined as the change of the velocity between adjacent fluid layers) strongly influences the RBC aggregation and migration, and consequently, CFL formation and blood viscosity. Low shear rates promote RBC aggregation and hence the CFL formation, while high shear can damage or even destroy the RBCs. Both the migration of RBCs (which forms the CFL) and RBC aggregation are responsible for the two phase formations in blood flow [4].

In large vessels, the blood cells are very small compared to the size of the vessel, so blood can be treated as a Newtonian fluid of single phase. At the microscale, however, the size of blood cells

is comparable to the vessel size and their presence influences blood behaviour; blood must therefore be considered a non-Newtonian fluid of two phases [1].

Further research into the complex behavior of blood is still needed at the microscale level. Of particular interest are the mechanisms involved in the formation of the CFL. This process is not yet fully understood; its investigation is complicated due to the many physical influences on the CFL formation and the small scales required for the measurements.

Several researchers investigated the CFL *in vivo* in animal studies [5–7], while other studies [8–10] attempted to mimic the CFL *in vitro* using microfluidic devices to further elucidate this phenomenon and explore its influence on rheological processes. There is, however, only limited quantitative information available in the literature. It is known that CFL formation depends on flow conditions, RBC properties, as well as the shape and dimensions of the blood vessels [7]. RBC aggregation enhances the formation of the CFL. This CFL and RBC aggregation are key factors influencing the rheological behaviour of blood in microcirculation. Previous research on CFL formation has showed conflicting results regarding the influence of the flow rate on the CFL thickness, and further investigation is necessary to clarify the relation between flow rate and CFL formation at different network scales and geometries. This experimental work is dedicated to investigating the influence of blood flow rate and microchannel geometry on CFL thickness at conditions (i.e. flow rate, diameter and hematocrit) close to those that exist in microcirculation. This work is also dedicated to establishing a relationship between the formation of CFL and the RBC aggregate size at the micro scale.

Flow conditions that inhibit the formation of the CFL are preferable for facilitating the exchange process between the RBCs and tissue or organ cells. Geometries that provide good blood mixing flow are preferable, as good mixing ensures adequate exposure of RBCs to exchange media such as endothelial cells or tissues. The microchannel bifurcation affects the distribution of the RBCs as well as the hematocrit, which may be associated with changes in the RBC aggregation and CFL formation. It is hypothesized that the microchannel bifurcation disturbs the blood flow, reducing RBC aggregation and consequently the CFL formation. A thinner CFL facilitates the exchange process and also increases the local blood viscosity. Employing good microchannel networks along with optimum flow rates can improve the blood flow characteristics and enhance the gas exchange and nutrient and drug delivery rates.

In the last two decades, there has been an exponential increase of interest in the field of microflows and lab-on-a-chip applications. Figure 1.1 shows the growth in the number of publications in those fields over the past 16 years.

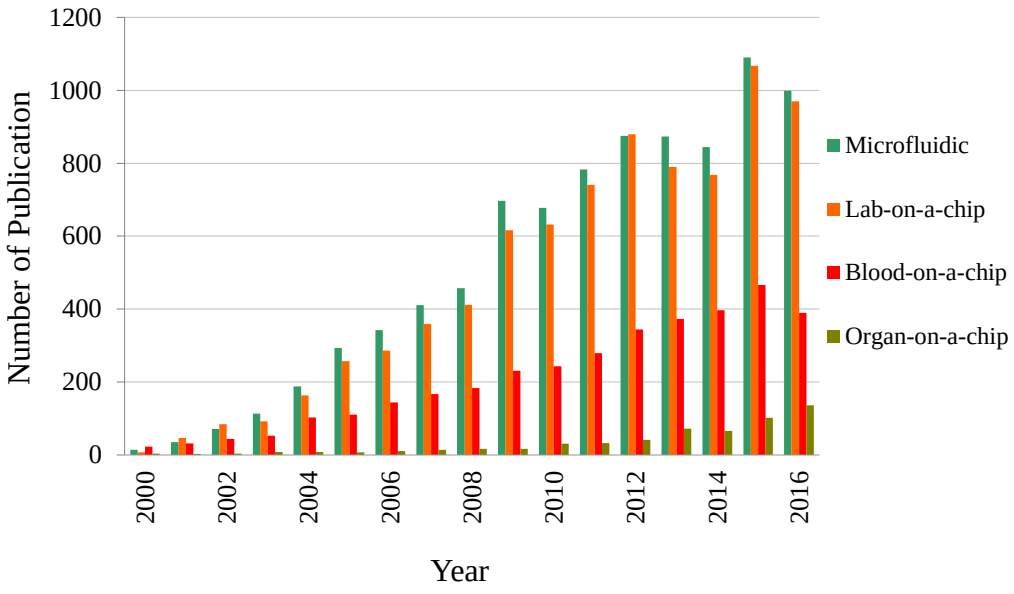

Figure 1.1: The rise in the publication in microfluidics, lab-on-a-chip, blood-on-a-chip and organ on-a-chip. These data are from the PubMed national library. The rise in publication demonstrates the increasing activities and interests in the respective fields.

Understanding the formation of the CFL is crucially needed in blood microfluidics applications since this CFL influences blood properties, flow resistance as well as exchange processes. Furthermore, there is growing interest in plasma separation from blood in the blood-on-a-chip and lab-on-a-chip communities. Plasma separation is an important step in many diagnostic tests such as blood-gas and electrolytes tests [11].

In particular, this study contributes to the understanding of the effects of both flow rate and microchannel geometry on the CFL formation. It also provides insight into the effects of flow rate and geometry on the RBC aggregate size. Furthermore, the outcomes of this work help to clarify the relationship between the CFL thickness and RBC aggregate size for a range of shear rates.

1.2 Research Objectives and Statement

The ultimate objective of this experimental work is to quantify the influence of the flow rate, the wall shear rate, and microchannel bifurcation on CFL formation. Specifically, the objectives are to:

1. quantitatively measure CFL thickness, adjacent to the wall in microchannels of different geometries, for a range of flow rates,
2. determine the relationship between RBC aggregate size and CFL thickness,
3. quantify the effects of shear rate on CFL thickness and aggregate size,
4. quantify the effects of bifurcating channel geometry on CFL thickness and aggregate size.

The measurements were performed under constant flow conditions for three different flow rates. To study the geometry's influence, three different microchannels geometries were used: one straight microchannel and two bifurcating microchannels having different bifurcating angles. All channels were fabricated with poly dimethyl siloxane (PDMS). Micro-particle image velocimetry (μPIV), coupled with a high-speed camera, was utilized to record images of the flowing blood, in order to determine the CFL thickness, the size of the RBC aggregates and the velocity profile. Human blood suspensions of 10% hematocrit (RBCs volume concentration) were tested within the three different microchannels, each at three different flow rates. The hematocrit value was chosen to mimic the physiological hematocrit in microcirculation, which is much lower than in the macrovessels.

The sets of experiments were performed as follows:

1- Cell-free layer quantitative measurement on both sides of the straight microchannels and at different locations of the bifurcating microchannel (before, within and after the bifurcation), for three different flow rates.

2- RBC aggregate size measurement for the same range of flow rates and same microchannel geometries used in the CFL measurement.

3- Velocity profile measurement at the three different flow rates in the different microchannels, to calculate the wall shear rate, the actual flow rate (*vs.* the programmed flow rate) and the maximum velocity at the center of the microchannel.

This experimental work provides quantitative measurements of CFL thickness for blood flows in microchannels and explores the relation between this thickness and the flow rate and wall shear

rate. Additionally, this research clarifies the effects of the microchannel bifurcating geometry on the CFL formation. Further measurements were made to measure RBC aggregate size and correlate it to CFL thickness.

The results for CFL and RBC aggregates will improve the understanding of how specific factors influence CFL, as well as what is its rheological relevance at the microcirculation level. Specifically, an understanding of the influence of blood flow rate and the resulting shear rates within physiological ranges is essential to improving knowledge about both CFL and aggregate formation. Furthermore, an investigation of the influence of vessel geometries on CFL and RBC aggregation will provide detailed information that may lead to improve designs and performance of many treatment and diagnostic tools involving blood flow and analysis, such as extracorporeal membrane oxygenation devices. The results may also be used towards improving lab-on-a-chip and organ-on-a-chip applications. Furthermore, the results may be used to implement a mathematical module into hemodynamical studies.

The research undertaken through the present study has resulted in the following manuscripts:

- Cell-Free Layer Formation in the Microchannel, in preparation.
- Flow Rate Dependency of Cell-Free Layer Thickness in Micro Blood Flow *In Vitro*, in preparation.
- The Influence Red Blood Cell Aggregation on the Formation of Cell-Free Layer in Micro flow at Low Shear Rate, in preparation.

1.3 Thesis Structure

The thesis is structured as follows:

Chapter 1 provides an introduction to the research, motivation, objectives and research statement.

Chapter 2 contains background information about blood properties and flow characteristics, in particular in the microcirculation. This chapter also covers the literature review about *in vitro* studies investigating blood rheology in microchannels, specifically those that investigated the formation of CFL, RBC aggregate size measurement, and measurement of the flow profile.

Finally, the chapter highlights the need for a better understanding of CFL and relating its formation to RBC aggregate size and applied shear rate.

Chapter 3 presents the materials and experimental set-up used in this work, as well as a detailed description of the data processing methods used.

Chapter 4 describes the experiments made for CFL measurements, presents and discusses the results. CFL thickness measurements were performed in straight and bifurcating microchannels and at three different flow rates.

Chapter 5 provides a detailed explanation about the experiments of RBC aggregation detection in microchannels, and the influence of RBC aggregation on CFL formation adjacent to the microchannel wall. RBC aggregates were assessed in blood flow in straight and bifurcating microchannels at three different flow rates.

Chapter 6 presents the experimental work on the velocity profile measurements to evaluate the shear rate at both sides of the microchannels and calculate the actual flow rate. The velocity profile measurements were performed on deionized (DI) water and 10% H human blood. The velocity profile measurements were made at the same flow rates and in the same microchannel geometries as used for the measurements of CFL and RBC aggregation. This chapter relates the wall shear rate results to CFL formation and RBC aggregation results.

Chapter 7 summarizes the study's conclusions and its contribution to biomedical applications. Specific applications that can benefit from the study's findings, such as the design of a blood oxygenation device, are described. Recommendations are given for future work that can be performed to further improve microfluidic applications.

Chapter 2
Background and Literature Review

This chapter covers background information about blood characteristics and hemorheology at the microscale. It also provides detailed explanations of previous studies and proposed methods in blood microflow. Specifically, it details studies that investigated the formation of the CFL, detected RBC aggregate size, and those that measured the flow velocity profile along with the shear rate.

2.1 Blood Composition

Blood is a non-Newtonian (i.e. whose viscosity is dependent of shear rate) suspension, consisting of 40-45% formed elements (by volume), namely red blood cells, white blood cells, and platelets. Red blood cells are involved primarily in oxygen transport from the lungs to the cells in the entire body. White blood cells are involved primarily in phagocytosis and immune responses. Platelets are involved in blood clotting [1,3,12,13]. The remaining 55% of blood consists of plasma. In addition to oxygen transport and immune function, blood has other functions including: nutrition and drug delivery; waste product removal and transfer to the kidneys and liver; and body temperature regulation. Most people have 4.5-6L of blood in their body which makes up 6-8% of their body weight [3,12,13]. The density of whole blood is approximately 1,060 kg/m^3.

2.1.1 Red Blood Cells

Red blood cells (RBCs) or erythrocytes are biconcave and have no nucleus, which improves their ability to carry oxygen. RBCs consist mainly of hemoglobin. They transport oxygen from the lungs and release it while squeezing through the organ's capillaries [1,12]. A typical human red blood cell has a disk diameter of approximately 8 μm and a thickness at the thickest point of about 2 μm and a minimum thickness in the center of about 1 μm. Figure 2.1 illustrates the geometry of the red blood cell. The functional lifetime of a RBC is approximately 125 days. Healthy adult humans have roughly 5 million red blood cells per ml of whole blood, varying with hematocrit, or the volume percentage of RBCs in whole blood [3,12,13]. RBCs comprise about one quarter of the

total number of cells in the human body. They are continually moving, being transported by the blood flow in the circulation system.

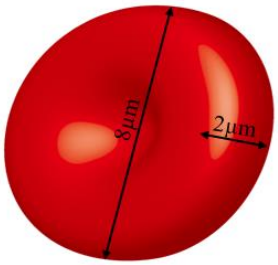

Figure 2.1: The shape and size of the red blood cell.

2.1.2 Plasma

Plasma is a transparent, amber-coloured liquid that normally holds the blood cells in suspension. It is mostly water (90% by volume). The remaining 10% contains dissolved proteins, glucose, clotting factors, mineral ions, hormones and nutrients. Blood plasma is a Newtonian fluid (its viscosity is constant with shear rate), and has a density of approximately 1025 kg/m^3, and viscosity ranging from 0.0015-0.0017 Pa.s at room temperature. The protein content in plasma causes its viscosity to be higher than that of water. [3,13,14].

2.2 Blood Characteristics

2.2.1 Hematocrit

Hematocrit (H) is defined as the volume percent of the blood occupied by the red blood cells. Since the red blood cells are delivering the oxygen and carbon dioxide between the lungs and the body tissues, the hematocrit is an important parameter. The systemic human hematocrit ranges from 40-45% [1,3,13], while in the microcirculation the hematocrit is much lower [15], less than 20%.

2.2.2 Viscosity

Unlike plasma, whose viscosity is independent of shear rate, whole blood is a non-Newtonian fluid, and its viscosity ranges between 0.003-0.006 Pa.s (3-6 cP). Blood viscosity referred to as the apparent viscosity depends on temperature, vessel diameter, hematocrit, and shear rate. The apparent viscosity of blood, defined as the ratio of the shear stress to the rate of shear, shows a precipitous decrease with decreasing vessel diameter, reaching a minimum at diameters of about

5–7 μm, corresponding to the diameter of capillaries. This trend is known as the Fahraeus-Lindqvist effect [12,14]. This effect can be explained by the migration of the RBCs toward the center of the vessel leaving a cell-depleted layer of plasma near the wall, which has a lower viscosity than whole blood [14]. Figure 2.2 shows the change of apparent viscosity as a function of tube radius for a hematocrit of 40%. Figure 2.3 illustrates the relation between blood viscosity and its hematocrit. For shear rates greater than 100 s^{-1}, blood behaves like a Newtonian fluid, where its viscosity becomes constant at a value of approximately 0.004- 0.005 Pa.s (4- 5 cP).

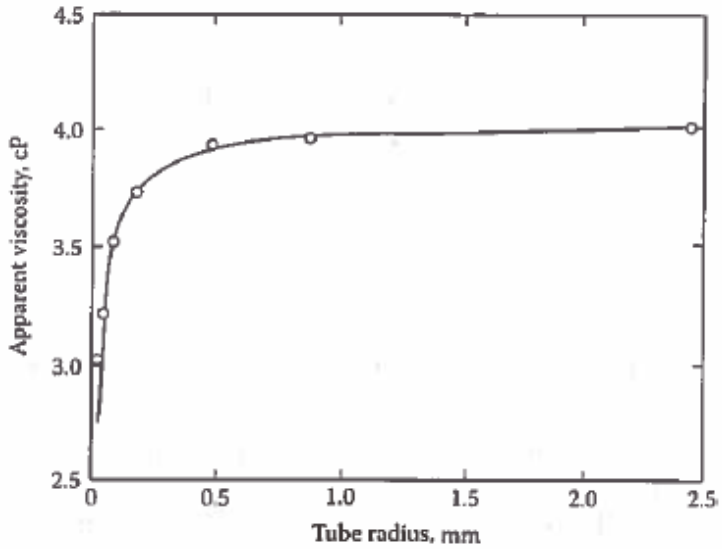

Figure 2.2: Apparent viscosity of blood as a function of tube radius at 40% hematocrit [14].

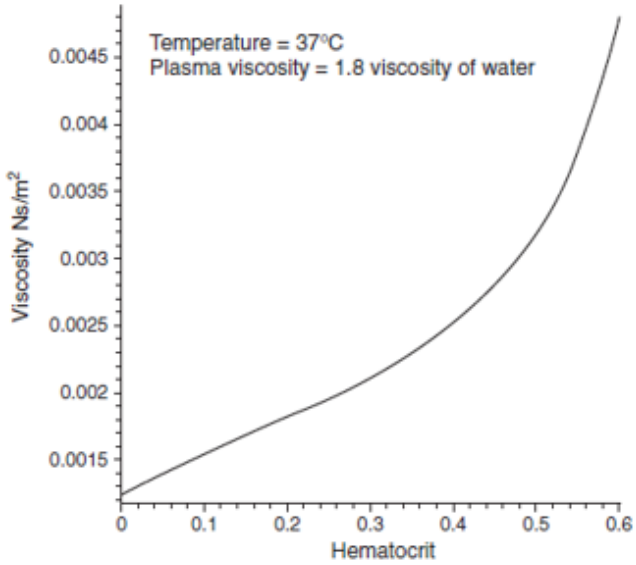

Figure 2.3: Blood viscosity as a function of hematocrit [13]. Hematocrit values are in decimal format, where 1.0 =100%.

2.3 Hemorheology

Hemorheology is defined as the science of the deformation and flow of blood and its formed elements (i.e., RBCs, WBCs, platelets). This field investigates properties of blood such as the viscous behaviour of blood in microcirculation. The rheological properties of blood are dependant on shear rate, and on the dimensions and geometry of the vessel network [12]. Normal RBCs deform when they traverse the capillaries. The deformability of RBCs is defined as the degree of their shape change in response to an applied force. RBCs tend to orient themselves with the flow streamlines. They behave elastic bodies, and their shapes reversibly change when the deforming forces are removed [3,12]. In microcirculation, where the vessel diameters are smaller than the RBC size, RBCs deform and pass individually through the microvessels, enabling them to come closer to the exchange surface and exchange larger amounts of gases and nutrients. Figure 2.4 shows RBCs deforming in a capillary[16].

An important rheological property of RBCs is their tendency to aggregate into linear arrays in which they are arranged like stacks of coins. These linear aggregates then interact with others to form three-dimensional structures. RBCs can reversibly disaggregate under the influence of shear forces. Increased shear reduces aggregation, by breaking up aggregates, whereas lower levels of shear promote aggregation [3]. RBC aggregation causes greater axial migration of the aggregates, which subsequently results in a larger cell-free layer (CFL) at the wall [12,17]. RBC aggregation additionally affects the distribution of WBCs and platelets [12,17]. RBC aggregation is an important marker in the clinical assessment of patients [18]; it is linked to some pathological conditions such as diabetes [17], cardiovascular diseases, genetic disorders and chronic diseases [19]. RBC deformation and aggregation affect blood flow in large and small blood vessels including in the microcirculation [3].

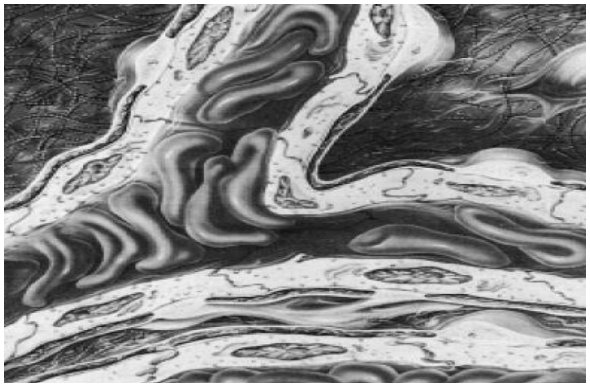

Figure 2.4: RBC deformation in microcirculation [3].

2.4 Microcirculation

In the human vascular system, blood flows from the heart via arteries, which branch and narrow into arterioles; these arterioles branch further into capillaries. After the tissue has been perfused (meaning blood is delivered to the capillary bed in the tissue), capillaries join and widen to become venules and then widen more to become veins, which return blood back to the heart [13]. Table 2.1 provides reference values for the vessel diameter, the corresponding average velocity u_{ave}, shear rate γ, and Reynold number Re in the human vascular network [20].

Table 2.1: Reference values for the vessel diameter (d), average velocity (u_{ave}), shear rate (γ), and Reynold number (Re) in the human vascular network [20].

Vessel	***d* (mm)**	**u_{ave} (m/s)**	**γ (1/s)**	**Re**
Aorta	25	0.4	130	2500
Arteries	4	0.45	900	450
Arterioles	0.05	0.05	8000	0.5
Capillaries	0.008	0.001	1000	0.002
Venules	0.02	0.002	800	0.01
Veins	5	0.1	160	125
Vena cave	30	0.38	100	2800

Microcirculation is the flow of blood in the body's vessels with diameters equal or less than 100 μm [12]. Here, the hematocrit is much lower than the systemic hematocrit [15,21] and can be even less than 5% in the capillaries [21]. In the human body, there are tens of thousands of microvessels per gram of tissue; these include arterioles, metarterioles, capillaries and venules. In fact, all of the cells in the body are close in scale to microvessels. Microcirculation is involved in the exchange of gases, water, nutrients, hormones, and metabolic waste products between blood and body cells [12,13]. Fluid flows through microvessels are usually characterized by low Reynolds numbers and are laminar [1,22]; for example, in small microvessels, where the diameters are less than 100 μm and the flow velocities are lower than 1 cm/s, the Reynolds number Re is less than 1 [23,24].

Capillaries make up the smallest blood vessels in the body. Their walls are only one cell thick (0.5 μm). They consist of highly permeable endothelial cells. These microvessels are 5-10 μm in diameter. The capillary walls have thin slits, or pores, between adjacent endothelial cells, approximately 6-7 nm wide, which allow water, oxygen and carbon dioxide molecules as well as the most water-soluble ions to diffuse easily through them. These capillary pores have different

sizes in different organs. There are about 10 billion capillaries in the body; having an average length of about 1 mm each, they provide about 500 m^2 of total surface area. Together, they contain approximately 500 ml of blood (roughly one-tenth of the system's total volume!). Capillaries connect arterioles and venules [13]. In general, the transfer of oxygen from RBCs to tissue cells is the greatest in the capillaries, however, it has been observed that a significant portion of oxygen transfer to tissues also occurs in the arterioles and venules [25]. Figure 2.5 illustrates a schematic of a typical microvascular bed.

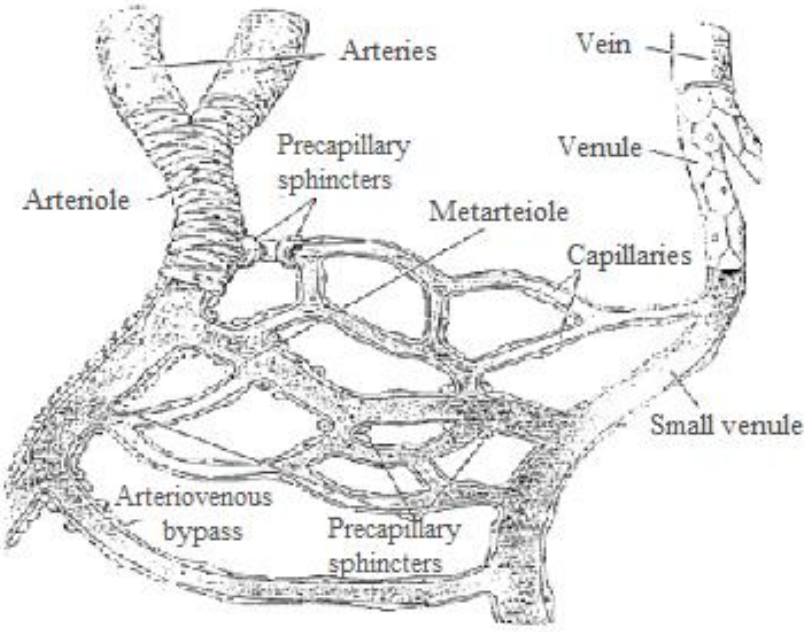

Figure 2.5: Schematic diagram of blood vessels in the microcirculation [14].

Oxygen transfer to the tissue bed can be affected by the local behaviour of RBCs. For example, it is reasonable to assume that when RBCs stack together forming an aggregate, their exchange surface area decreases, lowering their oxygen carrying capacity and limiting the gas exchange process. In addition, the blood's capacity for carrying oxygen is linearly proportional to its hematocrit, and the latter is strongly dependant on the network geometry [26]. Higher hematocrit, however, also causes increased blood viscosity and, consequently, higher flow resistance. This increase may, in turn, cause a reduction in blood flow rate and therefore a reduction in tissue perfusion as well [3,26].

2.5 Microfluidic Devices

Information about CFL is important to understand blood flow *in vitro* and improve the design and the performance of several microfluidic devices. These devices, which consist of fluid channels on the micron scale [27], are utilised in several biomedical applications such as for patient diagnosis, patient monitoring, and drug delivery. Abbott's i-STAT device (Abbott Point of Care Inc., New Jersey, USA) is an example of a microfluidic device used to analyze blood for clinical diagnoses [28]. Microfluidic devices are also used in the fields of "lab on a chip" and "organ on a chip", for example the design of an artificial lung [29,30]. The use of microfluidic devices for biomedical research has significant advantages since the required volume of fluids is very small (several nanoliters), as is the required amount of reagents and analytes. This is especially significant in the case where expensive reagents are required [27].

Microfluidic devices can be created using microfabrication techniques [31]. Typically, these devices are fabricated from glass, silicon and polymers, or combinations of these materials. Glass has well-defined surface chemistries and high optical transparency [32], however glass microchannels are not ideal to study the blood flow. This is due to the glass rigid nature which imparts the walls of glass microchannels with different properties from microvessels: the walls are not elastic [33]. Hence, polymers and elastomers are more attractive for microfluidic devices fabrication. Examples of some polymers commonly used are polystyrene, polypropylene, polymethyl methacrylate and polydimethylsiloxane (PDMS).

Amongst these polymers, PDMS has very useful properties for microfluidic applications [32]. PDMS elastomer is elastic, biocompatible, optically transparent, gas permeable and inexpensive. PDMS is also easy to mold into sub-micrometer features, and bonds easily to PDMS replica and glass slides [32,33]. Although PDMS has several advantages, its surface is hydrophobic; however this can be improved by plasma treatment. Plasma surface modification utilizes gases, such as oxygen or nitrogen, which dissociate and interact with the substrate surface, forming chemical functional groups [32]. This results in a tight bonding between the two surfaces. PDMS channels have been successfully used to study microscale blood flows in many studies [9,34,35].

Blood flow characteristics in microfluidic devices are not yet entirely understood, and there is a critical need for better understanding blood phenomena at the microscopic level [31], in particular the formation of CFL. Even though the flow in microchannels is mostly laminar, blood microflows exhibit non-Newtonian characteristics. This makes both numerical analysis as well as experimental

measurement of these flows challenging [36]. The study of flows in microfluidic devices can be further complicated by the nature of blood (e.g. it's multiphase characteristics), the small scales of measurements required, and added difficulties achieving accuracy in data processing (e.g. due to the opacity of RBCs) [33,37].

2.6 The Cell-Free Layer

As blood flows into microvessels, erythrocytes (RBCs) tend to migrate away from the vessel walls toward the vessel centerline. This migration leads to the formation of two phases: an RBC core flowing at the center and a cell-depleted layer or a cell-free layer (CFL) next to the vessel wall [4,8,38]. The CFL thickness is defined as the distance between the vessel or microchannel wall, and the boundary of the RBC core [5,8].

The migration of RBCs and subsequent formation of CFL are governed by hydrodynamic interactions between the RBCs and channel walls, which referred to as a lift force that acts on cells, and by the cell–cell interactions or collisions which results in shear-induced diffusion [39,40]. The lift force drives RBCs to flow away from the walls toward the channel or vessel center [39,41,42]. According to Hudson (2003) who studied the droplet migration, the migration velocity u_{mig} away from the wall is proportional to the squared magnitude of shear rate or the velocity gradient (γ) and proportional to the 4th power of cell radius r (of either individual RBCs or aggregates), i.e. $u_{mig} \propto \gamma^2 * r^4 / y^2$ [42,43], where y is the distance from the wall to the center of the cell. The cell–cell interactions, in contrast, lead to RBCs dispersion and flow toward the wall [5,39]. The shear-induced diffusion D is also proportional to the shear rate and the cell radius, i.e. $D \propto \gamma * r^2$ [42,43]. Figure 2.6 shows a schematic diagram of the lift force or cell-wall interaction (cw) and cell-cell interaction (cc).

The gradient in the shear rate and presence of the wall lead to an asymmetry of forces acting on RBCs which causes a radial motion of RBCs in the direction of higher velocity (i.e. toward the vessel center) [40,44]. In other word, the RBCs migrate from the high shear region at the wall to the lower shear region at the vessel center. The velocity of the radial migration is greatest near the wall and decreases toward the axis [45]. The balance between the lift force and the force due to shear-induced diffusion results in a net force on the cells acting radially inward resulting in the formation of an RBC core surrounded by CFL [39,40].

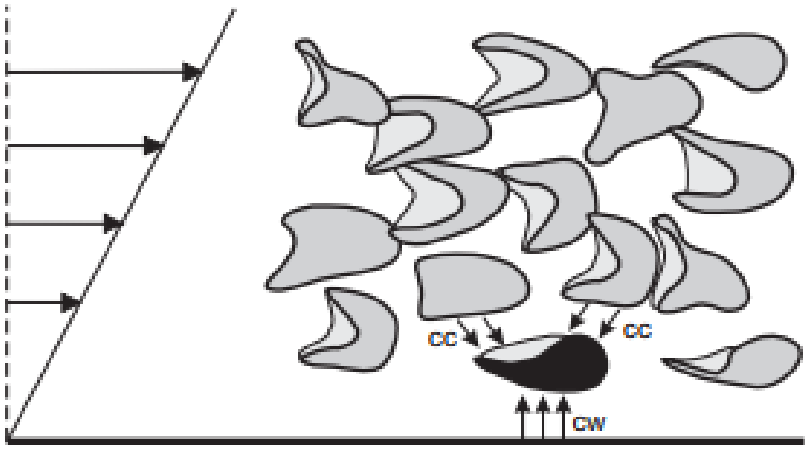

Figure 2.6: Schematic diagram of the force balance between the lift force or cell-wall interaction (cw) and cell-cell interaction (cc) [42].

The deformability of the cells also influences the net forces acting on them, and their resulting motion. Figure 2.7 illustrates the migration of the deformable RBCs in comparison with hardened HRBCs and rigid spheres in low and high shear rates. At low shear rate, Figure 2.7 shows that the deformable RBCs migrate toward the center due to the radial hydrodynamic force, while the hardened HRBCs and rigid spheres move axially without any migration.

At the high shear rate, where the inertial forces become important, both deformable and rigid particles have axial migration, however the rigid spherical particles migrate in both directions: the particles near the wall migrate toward the centre, whereas the ones at the centre migrate toward the wall [37,45], these cells move toward an equilibrium radial position approximately 0.6r from the axis, where r is the vessel radius [45].

The RBCs migration towards the channel center increases with increased particle size and deformability, velocity gradient, and radial distance from the axis [44,45]. The thickness of the resulted CFL is a function of several parameters including hematocrit (volume concentration of RBCs), RBC aggregation, flow rate, and vessel or channel diameter [39,46]. Figure 2.8 illustrates the RBCs flow and CFL in the microcirculation [1].

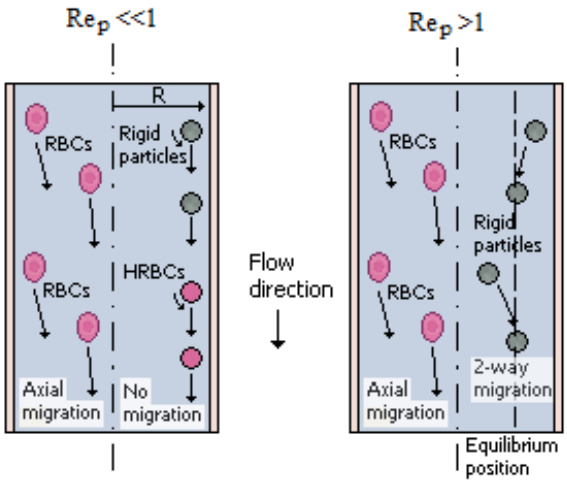

Figure 2.7: Schematic illustration of migration differences between healthy RBCs, hardened HRBCs and rigid spheres in the centre of a capillary. Re_p is the particle Reynolds number [47].

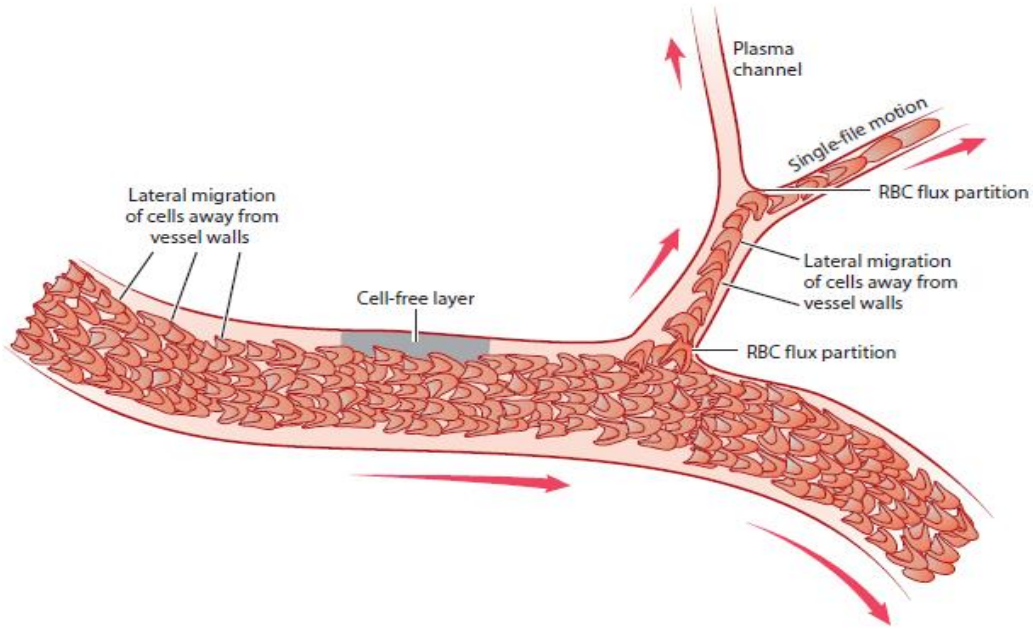

Figure 2.8: Blood flow in microcirculation. RBC concentrated at the center region and CFL formed adjacent to the vessel wall [1].

Even though the formation of the CFL has been of great interest over many years, there has been relatively limited information available about this phenomenon. This is mainly due to the complicated nature of the flow, which make its study difficult; specific challenges include: (i) the multi-physical influences on the CFL formation, (ii) the small scale of the investigation; and (iii) the complexity of the blood as a working fluid [33,37].

Several studies have focused on investigating the CFL *in vivo*, while other studies have attempted to mimic the CFL *in vitro* using microfluidic systems, in order to further clarify this phenomenon and explore its influence on the rheological processes. It was shown that the CFL influences many rheological phenomena, such as apparent blood viscosity and wall shear stress, as well as gas exchange [2,46]. It may also influence nutrient and medicine delivery. These influences will be discussed in the following.

The CFL is important in the microcirculation as its thickness is significant with respect to the diameter of microvessels, whereas, in larger vessels, the CFL thickness becomes negligible with respect to the vessel diameter, and consequently has a much smaller effect on the flow [38]. Initially, the CFL is believed to lubricate the blood flow by reducing the friction between the RBCs and the endothelial cells – the CFL has a lower viscosity compared to the RBC core. It follows that a thicker CFL results in lower apparent viscosity of flowing blood and consequently lower flow resistance [2,38]. Moreover, the CFL influences the exchange processes by adding an extra barrier to the gas exchange between the RBCs and the target cells [2,5]. For instance, the CFL reduces nitric oxide (NO) scavenging from the endothelium to RBCs [2,46]. Furthermore, the respiration process, mainly oxygen delivery and carbon dioxide removal, is affected by the thickness of the CFL, this is particularly important in blood oxygenation [48]. Similarly, in several medical devices such as a point-of-care diagnosis chip, the separation of plasma from whole blood is an important and critical step in medical diagnostics [4]. Knowledge of how the CFL develops can be used to inform and improve the methods used for this plasma separation.

Other key factors that influence the blood flow in the microcirculation are RBC aggregation and deformation, the distribution of RBCs inside and between channels, the vessel geometry and the blood flow rate. It has been well established that RBC aggregation reaches its maximum at low shear rates, causing the blood viscosity to increase. It was also found that RBC aggregation influences the migration of RBCs and hence, the CFL formation [3].

As discussed, blood cells in the microcirculation are not evenly distributed. This influences the local rheological properties such as the local hematocrit, the apparent viscosity, and the velocity profile [12,21]. Fedosov et al. 2010 and Kim et al. 2007 showed that differences in the upstream flow condition can cause the CFL to form asymmetrical on both sides of the flow path [6,38]. Additionally, blood behaviour at the microscale is affected by the vessel's shape and dimensions; for example, the bifurcating geometry of blood vessels influences the formation of the CFL [4,9].

A bifurcation also changes the hematocrit distribution from the mother vessel to the daughter branches [3,38]. Other work presented by Pinto et al. 2015 showed that the CFL thickness is not strongly influenced by the microchannel bifurcation for either diverging or converging bifurcations. Ishikawa et al. 2011 and Li et al. 2012 compared the CFL thickness between the inner and the outer walls of the bifurcation. RBCs tended to collide with the inner wall of the bifurcation where no CFL was detected, while RBCs tended to flow away from the outer wall forming a clear CFL. Novais et al. 2014 reported that a contraction in a microchannel causes an increase of the CFL thickness. Lastly, changes in the blood flow rate are associated with changes in the shear rate at the wall, thus affecting RBC aggregation properties [2,5], and hence the formation of the CFL. Applying a high flow rate lowers the tendency of RBCs to aggregate and this reflects the changes in the viscosity; conversely, employing a lower flow rate within the physiological values in microcirculation allows the RBCs to aggregate. Despite these observations, the influence of blood flow rate on the CFL formation is not yet clearly defined. Fedosov et al. 2010 and Ong et al. 2010 concluded that a the CFL thickness reduces with increasing flow rate [5,38], however, Novais et al. 2014, showed that no clear effect was detected [8], and Sampaio et al. 2015 revealed a nonlinear increase of the CFL width with increasing the flow rate [49]. In other words, the existing studies of flow rate effect on CFL thickness have contradicting results. It should be mentioned that the *in vivo* studies of CFL thickness, such as those by Ong et al. 2010 and Kim et al. 2007, reported the systemic hematocrit of about 40%, but their CFL measurements were performed in the arterioles where the hematocrit level is much lower. These *in vitro* studies were performed at conditions that do not reflect the physiological blood flow in microcirculation, while the *in vivo* ones reported the systemic level of hematocrit which is much higher than locally found in microcirculation.

Figure 2.9 shows data from previous *in vitro* studies of the CFL, plotted versus the average flow velocity and channel diameter. The data was extracted from graphs of Novais et al. 2014 [8], Pinto et al. 2015 [10], and Sampaio et al. 2015 [49]. This figure shows that the CFL width or thickness depends on the employed flow rate or velocity, hematocrit and vessel or microchannel size. Sampaio et al. 2015 performed the CFL measurements at the systematic hematocrit (40%) and in small microchannel (less than 100 μm in diameter), while Novais et al. 2014 and pinto et al. 2015 worked with channels of larger diameter (150 μm- 180 μm). Figure 2.9 shows that there is an essential need to preform CFL measurements at the physiological range of the microcirculation,

where H< 20%, the diameter is less than 100 µm and for a lower range of flow rates. It is important to study CFL formation under lower flow rates because, *in vivo*, reduced flow rates enhance the gas exchange and nutrient and drug delivery rate between RBCs and its surrounding cells.

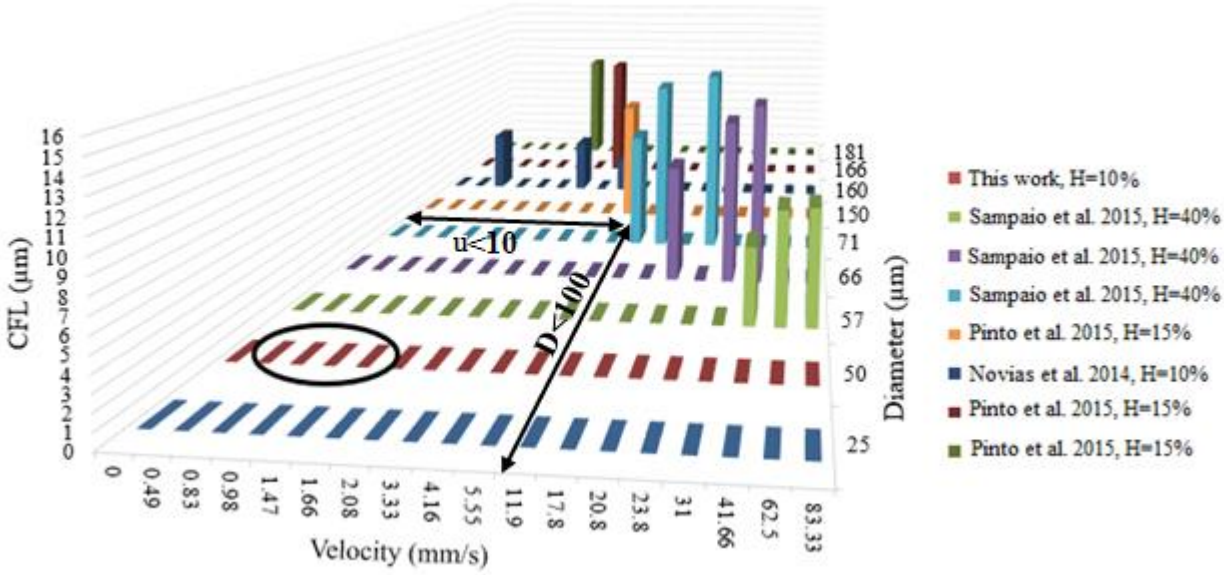

Figure 2.9: Comparison of the CFL thickness (µm) as a function of both the average velocity (mm/s) and microchannel diameter (µm), for previous *in vitro* studies of; Novias et al. 2014 [8], Pinto et al. 2015 [10], and Sampaio et al. 2015 [49]. The area between the axis and the arrows indicates the needed range for CFL measurements. The oval points to the intended range of the CFL measurements in this work, using 10% H human blood.

Considering previous measurements of CFL thickness, which were performed *in vitro* and *in vivo*, as well as by simulation, CFL data were collected from literature [4–10,38,39,48–52] and plotted as a function of the pseudo-shear rate (γ) as shown in Figure 2.10. The pseudo-shear rate was calculated as:

$$\gamma = u_{ave} / d \qquad (2.1)$$

where, u_{ave} is the average velocity and d is the vessel diameter [5]. It has to be mentioned that these different studies were performed using either human or animal blood samples, either in the presence or absence of aggregation, and under different conditions of hematocrit, vessel diameter, vessel shape and flow rate.

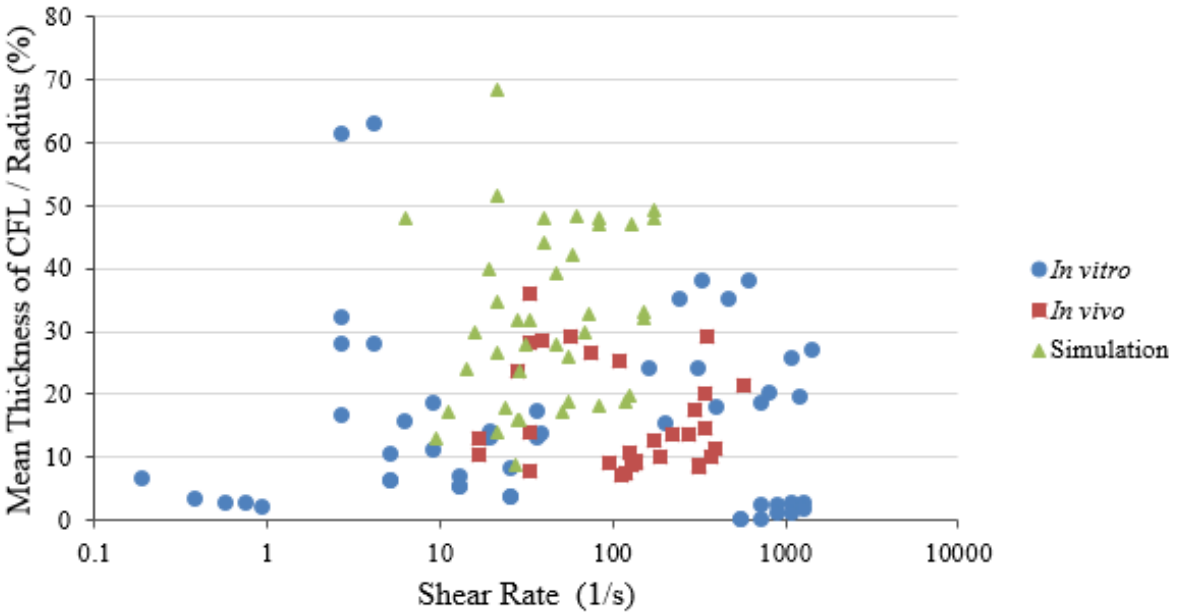

Figure 2.10: The mean CFL thickness / radius (%) as a function of the pseudo-shear rate (s^{-1}) for previous *in vitro* and *in vivo* studies which were performed under different conditions of: blood type, hematocrit, vessel diameter, vessel shape and flow rate. The *in vitro* studies (●) include those of Novais et al. 2014 [8], Ishikawa et al. 2011 [9], Pinto et al. 2015 [10], Rieper et al. 2014 [48], Sampaio et al. 2015 [49], Lauri et al. 2016 [50], Sherwood et al. 2012 [51], and Cerdeira et al. 2009 [52]; the *in vivo* studies (■) include those of Ong et al. 2010 [5], Kim et al. 2007 [6], and Maeda et al. 1996 [7]; and the simulation studies (▲) include those of Li et al. 2012 [4], Fedosov et al. 2010 [38] and Katanov et al. 2015 [39]. All data is available in Appendix A.

There is no clear trend observed for the shear rate effect on the CFL results, as shown in Figure 2.10. Low shear rate impacts the CFL differently if compared with the high shear rate. It is hypothesized that the indistinct effect of the shear rate is attributed to the added influence of RBC aggregation on the CFL, which occurs only under low shear conditions.

There is no study in the literature that correlates the mechanism of the CFL formation to the applied shear rate considering the size of RBC aggregates. The present experimental work aims to understand the link between the formation of CFL, RBC aggregate size, and the applied shear rate. This experimental work was performed under different conditions than were used in previous studies. The CFL was measured at blood hematocrit levels that occur in microcirculation (less than 20%). Also, the blood velocity range matched those found in the capillaries and venules, which is reported in literature to be about 2 mm/s [20]. Moreover, the three microchannel geometries used in this study each had a hydraulic diameter of about 50 µm, which is roughly equivalent to those of microvessels.

2.6.1 CFL Thickness Measurements

In the literature, CFL measurement is typically performed using a high-speed camera system [10,53]. The use of a high-speed camera requires illuminated RBCs. The captured images can be processed either manually or automatically in order to evaluate the thickness of the CFL.

2.6.1.1 Manual Image Processing

The CFL thickness can be measured manually by using an image analysis software such as ImageJ. The trajectory of an individual peripheral flowing RBC can be tracked with the MTrackJ plugin for ImageJ. First, the centroid of the peripheral RBC is automatically computed, and then its *x* and *y* coordinates are obtained. The RBC trajectory is determined from the history of the *x*-*y* data. The MTrackJ plugin also detects the position of the adjacent wall. The distance between RBC trajectory and the adjacent wall is calculated and represents the CFL thickness [10,53,54]. Figure 2.11 shows the RBC core, the trajectory of a peripheral flowing RBC and the wall.

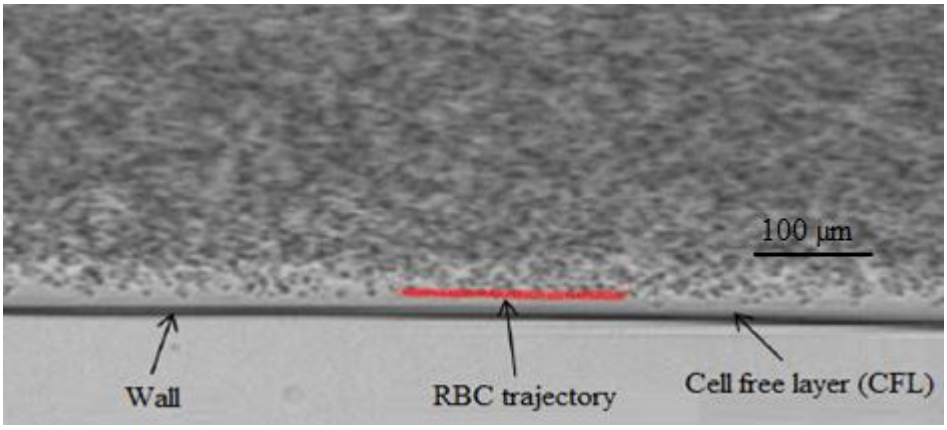

Figure 2.11: A trajectory of RBC flowing around the periphery region of RBC core [53].

This manual method of measurement is not appropriate when detailed information about the spatial and temporal variations of the CFL is required. Also, the manual tracking can be time consuming, biased, and performance dependent, which may result in low reliability of the measurement [2].

2.6.1.2 Automated Image Processing

A- Histogram Based Thresholding Algorithm

To overcome the limitations of manual image processing, Kim et al. 2006 proposed a simple, effective and consistent method for CFL determination by adopting computerized image processing technique [55]. This method is based on the light intensity of the images. Figure 2.12 shows the digital images resulting from this process.

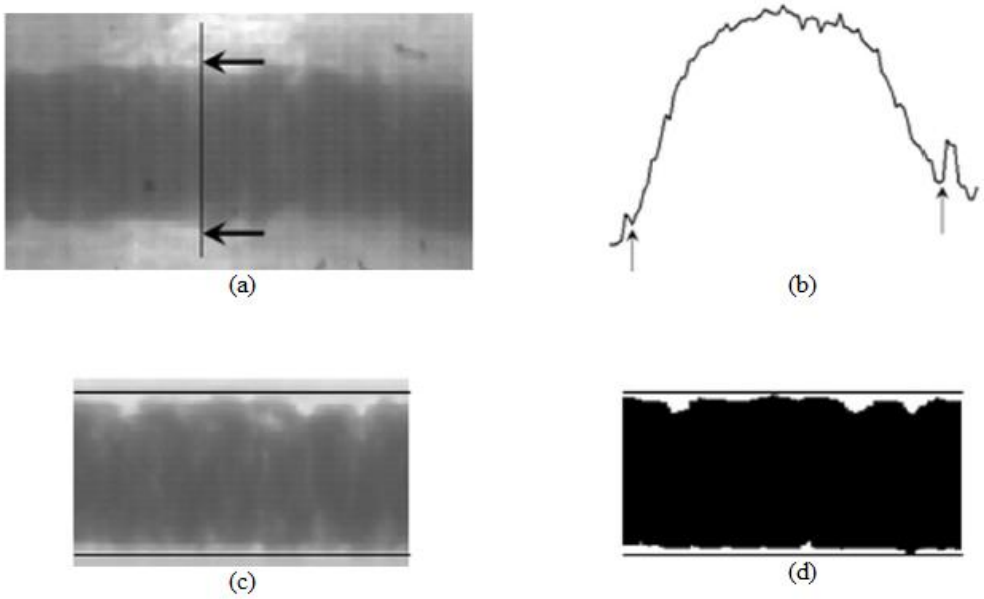

Figure 2.12: Computer-based method for cell-free layer width determination. (a) Grayscale images for RBC flowing into a venule. (b) The profile of light intensity along the analysis line. (c) Grayscale image. (d) Binary image. The location of vessel wall is represented by arrows in (a) and (b) and by solid lines in (c) and (d) [55].

First, the high-speed camera images are converted to gray scale images. To reduce noise, a median filter is applied to each image. Next, an analysis line is identified across the vessel at the desired location (Figure 2.12 (a)). To identify the vessel wall, the light intensity profile is obtained along the analysis line and an initial peak in intensity, transitioning from dark to light over two adjacent pixels, indicates the location of the inner vessel wall, as shown by the arrows in Figure 2.12 (b). After the wall identification step and accumulation of all sequential images, the light intensity profile along the analysis line is used to produce a single grayscale image, as shown in Figure 2.12 (c). The grayscale image is then converted into a binary image based on a certain thresholding value, as shown in Figure 2.12 (d). Finally, from the binary image, the CFL thickness

is calculated in pixels as the distance between the vessel wall and the dark region representing the RBC core [2,55].

To better measure the CFL width, several histogram-based thresholding algorithms were used. Although this method is simple and easy to implement, its result is not highly accurate, especially when the sizes of the objects (e.g. RBCs) and the background are significantly different. Additional treatment may be required (e.g. digital image contrast enhancement) to improve the image contrast.

B - Grayscale Method (Edge Detection)

The light intensity can significantly influence the image contrast, especially if the measurement is performed on an arteriole located in a deep tissue, for which the light must pass through the intermediate tissue. In such cases, a faint shaded region close to the vessel wall may be detected and the histogram-based method is insufficient [56]; Ong et al. 2011 proposed an alternate method called the grayscale method [56], which accounts for this faint shaded region. This grayscale method, which is based on the edge detection, detects the local boundaries between the CFL and RBC core as well as that of the inner vessel wall without binarization of the grayscale image. A comparison between the histogram-based method and the grayscale method concluded that the gray scale method could overcome the overestimation of the CFL (due to the presence of the faint gray region) and provide more accurate CFL width [56].

Using the grayscale method, the analysis line is first drawn perpendicular to the vessel axis at a location where the inner vessel wall is clearly distinct from the background as shown in Figure 2.13 (a). Then, the inner wall location is identified by comparing the light intensity between two successive pixels along the analysis line, as shown in Figure 2.13 (b). The location of the inner vessel wall is identified as the point at which the local maximum light intensity begins to decrease. In Figure 2.13 (b), the location of the maximum increase in the light intensity defines the boundary between RBC core and the CFL region. The CFL thickness is calculated as the distance in pixels between this boundary and the vessel wall.

Next, the intensities along the analysis line are determined for the consecutive frames and these are combined to reconstruct a 2D image with the abscissa corresponding to the vessel radius and the ordinate corresponding to time (Figure 2.13 (c)).

Using this method, the resulting CFL thickness may incorrectly include part of the RBC core region. To correct for this, the averaged intensity of the prospective CFL region is calculated, and any pixel in the faint gray region having lower intensity than this average is considered to be part of the RBC core. The outline of the RBC flow obtained by the grayscale method is shown in Figure 2.13 (d) [56].

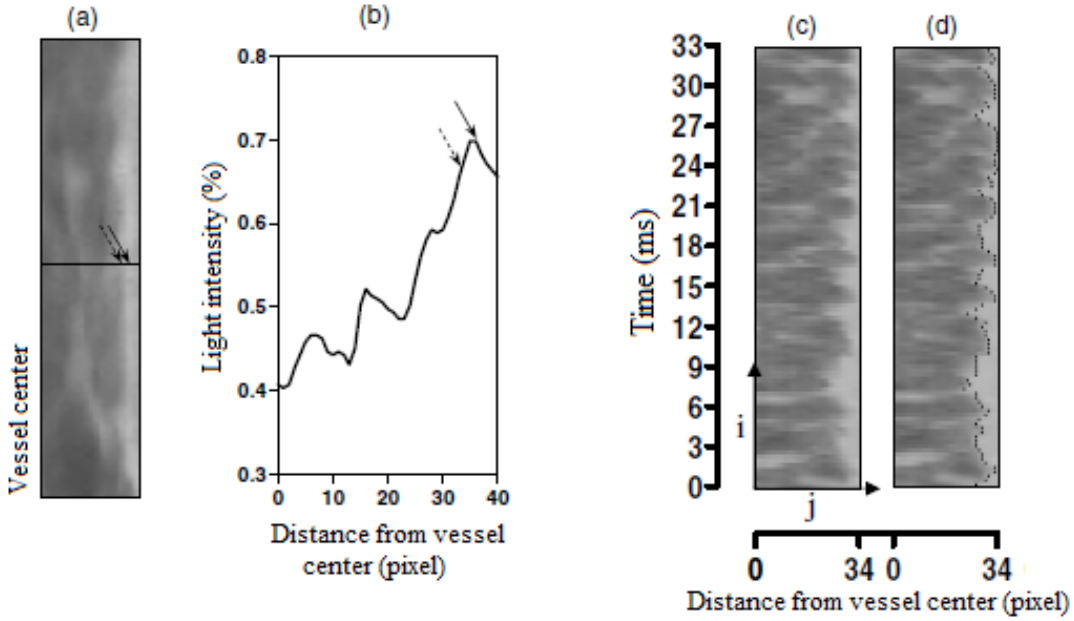

Figure 2.13: Digital image analyses for cell-free layer width determination. (a) Image of flowing RBC in an arteriole of ID= 28.4 μm, with the location of the analysis line. (b) Intensity-profile along the analysis line shown in (a). The solid arrow indicates to the location of the luminal vessel wall whereas the dashed arrow indicates to the location of the maximum intensity rise. (c) Reconstructed image at analysis lines from 100 successive frames for 33 ms. (d) Outline of the RBC flow determined by the grayscale method [56].

The methods described here are able to detect and measure the CFL thickness either manually or automatically. For a given experiment, the image processing method should be chosen to best match the image quality and the experimental conditions, specifically the magnification objective, the inner vessel diameter, the image contrast, and the image resolution [2]. Considering the microchannel size and the blood concentration used in this recent study, an image processing method was developed in order to detect and measure the CFL thickness. This method is based on the image light intensity. Detailed explanation is presented in the next chapter.

2.7 Red Blood Cell Aggregation

Under low shear conditions and in the presence of plasma proteins, deformable RBCs bridge together and form aggregates (rouleaux) in blood [21]. Figure 2.14 shows a representative assortment of human RBC aggregates in native plasma [57].

The RBC aggregation is dependent on the local flow conditions, the concentration of plasma proteins as well as the mechanical properties of the RBCs, themselves. The mechanism of RBC aggregation can be explained by the surface adsorption of long-chain macromolecules such as fibrinogen and dextran by the adjacent RBCs membrane. This adsorption cross-links these RBCs leading them to bridge together. Due to the deformability of the RBC, multiple bridges can be formed maximizing the area in close contact forming a rouleau.

Figure 2.14: RBC aggregates in blood plasma at stasis, small round particles are platelets [57].

Another potential mechanism explaining aggregate formation is that a reduction in the concentration of macromolecules in the vicinity of RBCs due to the imbalance between the loss of polymer configuration entropy and the adsorption energy. This difference in concentration causes a reduction the local osmotic forces; this, in turn, causes the inter-cellular fluid to move away, thereby pushing the RBCs together and enhancing their tendency to bridge together [19,44]. The RBC aggregation phenomena is a revisable process in which RBCs disaggregate when the local shear becomes sufficiently high [3]. RBC deformation and aggregation, along with its volume concentration (hematocrit) all influence the blood viscosity (and consequently the flow resistance) [21]. RBC aggregation is normally present in humans and in many athletic animals, but not in sedentary animals [5,44]. In athletic species, the increase in flow rate from rest to maximal

exercise is high, requiring a large difference in the blood apparent viscosity and hence higher capacity of RBC aggregation in order to regulate the resistance and the hydraulic pressure [58]. The property of aggregating red blood cells was first described by John Hunter in 1786, who considered aggregation to be related to a pathological condition, since it was observed in some diseases [44] and was known to alter the blood transport properties. Indeed, increased levels of RBC aggregation are observed in pathological conditions including diabetes, Alzheimer's disease, sickle cell anaemia, as well as in rheumatological conditions [17].

It was advocated that both RBC aggregation and the blood flow rate are responsible for the radial migration of RBCs toward the vessel centerline and the resulting CFL formation near the vessel wall.

2.7.1 Red Blood Cell Aggregation Measurements

It has been established that the measurement of RBC aggregation is essential in order to understand blood flow behaviour under physiological and pathological conditions [17]. The relative magnitude of RBC aggregation can be studied quantitatively by measuring a number of parameters including: the rouleaux formation rate, the average number of RBCs within an aggregate, or the force required to bridge adjacent RBCs.

2.7.1.1 The Erythrocyte Sedimentation Rate (ESR)

The erythrocyte sedimentation rate (ESR) method is based on the natural separation of blood into layers of plasma and RBCs by gravity. Edmund Biernacki first introduced this method in 1897 when he observed that fibrinogen influences the rate at which RBCs settle (a.k.a. the sedimentation rate). The main factors that influence the ESR are the properties of the RBCs themselves and the plasma proteins [57,59], which can both be affected by states of inflammation and tissue injury [57,59]. As normal RBCs have negatively charged ends, they repel one another, thus slowing the sedimentation process. Large RBC aggregates tend to settle faster than smaller ones, meaning that any factors that influence aggregation consequently also influence sedimentation.

The ESR test is performed by placing an anticoagulated whole blood sample in a test tube, and measuring the level of separated plasma after 60 minutes [59]. Since it was first developed by Fahraeus and Westergren in 1920, the ESR method has become widely used as a clinical diagnosis tool [57,59]. Figure 2.15 illustrates an ESR Westergren test for two different blood samples [59].

Normal clinical values for Westergren ERS are ≤15 mm/hr for adult males and ≤20 mm/hr for adult females, noting that the ESR value increases with age. An ESR value greater than 50 mm/hr indicates a high probability of disease [59].

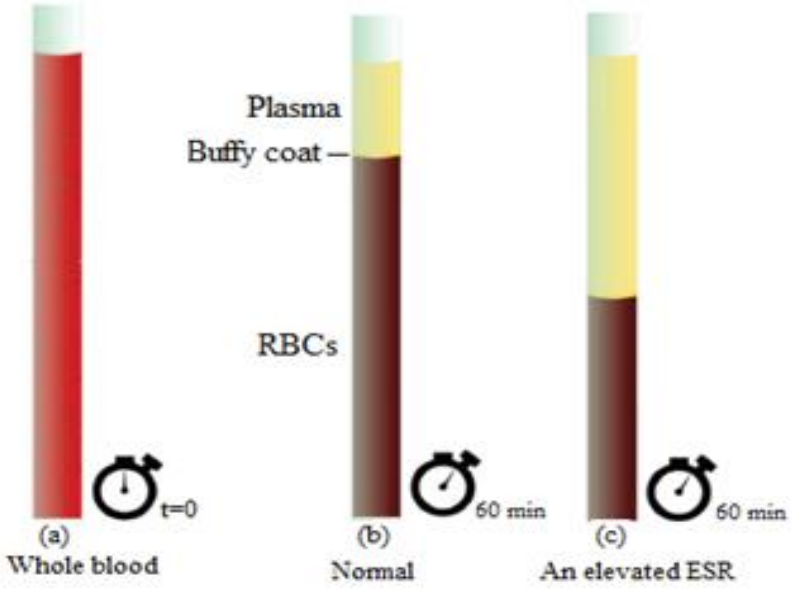

Figure 2.15: The ESR Westergren test. (a) whole blood sample is aspired in Westergren tube, (b) A normal ESR, < 20 mm plasma, (c) an elevated ESR [59].

2.7.1.2 The Microscopic Aggregation Index (MAI)

For the microscopic aggregation index (MAI*)* method, a resting blood sample is visually tested the under a microscope. In this method, suspensions of 1% RBCs (by volume) are prepared in aggregating and non-aggregating media and placed into a hemocytometer chamber (a device for counting blood cells), for 10-15 minutes. The MAI is then calculated manually as the ratio of the number of aggregates to the number of single RBCs counted in both the aggregating and non-aggregating media [60]:

$$\mathrm{MAI} = \frac{Agg._{counts}}{RBC_{counts}} \qquad (2.2)$$

where, the $Agg._{count}$ is the aggregates count in the aggregating medium, while the RBC_{count} is the RBCs count in the non-aggregation medium. Even though the MAI method provides a good indication about the RBC aggregation, the method of manually counting is time consuming and subject to error. Furthermore, the MAI method offers no information about the rate of aggregation.

2.7.1.3 Automated Measurements Image Analysis

The pitfalls of manual counting in the MAI method can be overcome by using image analysis techniques. Using such techniques, images for resting or flowing RBCs can be captured and digitally processed to provide quantitative information on the number of single RBC and the aggregates. Also, information about the aggregate shape, size and distribution can be derived. The RBC images and videos can be used to monitor and study the kinetics of aggregation as well as the disaggregation characteristics under various shear stress conditions [61]. Jayavanth and Singh (2004) studied RBC aggregation during gravitational sedimentation, using a video microscopic system. To quantify the aggregation process, the captured images were processed to measure the projected aggregate area (PAA), the projected aggregate perimeter (PAP) and the sedimentation completion time (SCT) [62]. Figure 2.16 illustrates the images after implementation of the different image processing steps.

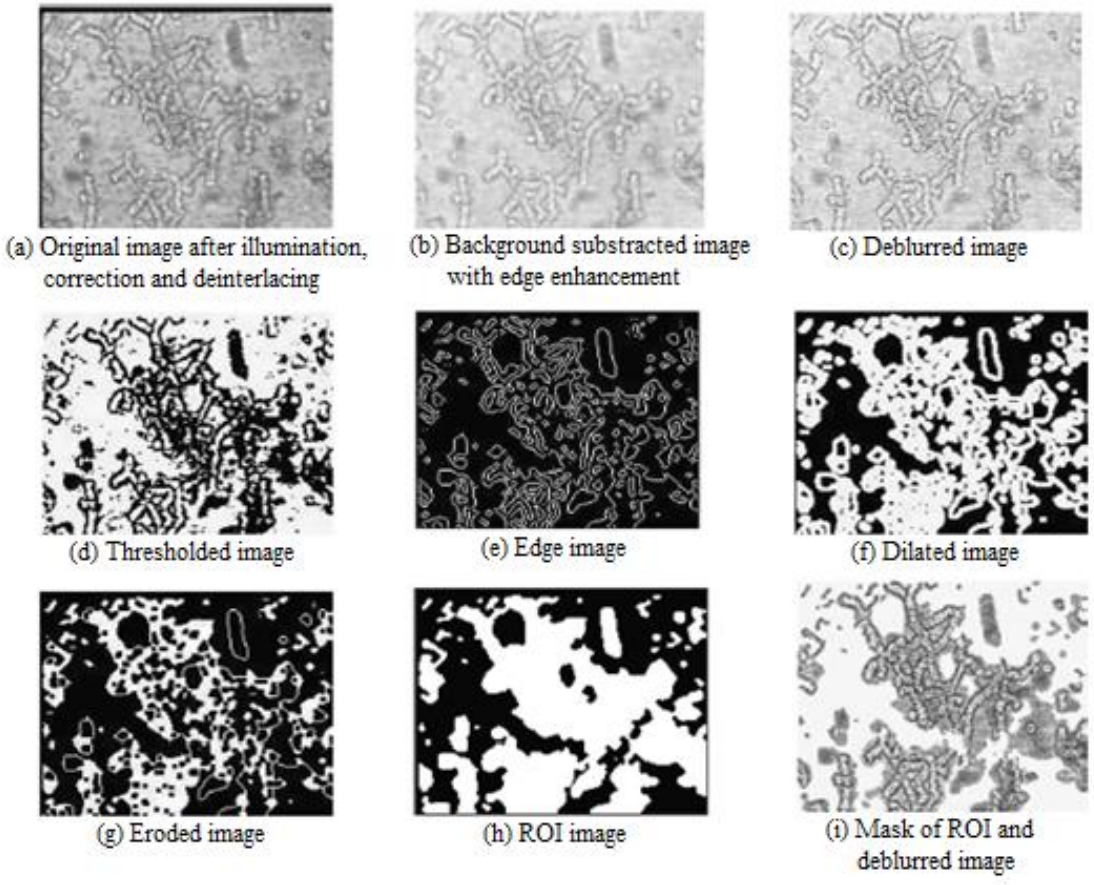

Figure 2.16: Sequence of images processing steps. (a) Original image (illuminated, corrected and de-interlaced, (b) image with background subtraction and edge enhancement, (c) de-blurred image, (d) threshold of the image, (e) edge image, (f) dilate of the image, (g) eroded image, (h) ROI image, (i) ROI mask and de-blurred image [62].

Foresto et al. (2000) characterized the aggregation morphology by a dimensionless parameter called the RBC aggregate shape parameter (ASP), which they defined as [63]:

$$ASP = \frac{4\pi A}{P^2} \qquad (2.3)$$

where, A is the aggregate projected area and P is aggregate perimeter. It should be noted that the ASP value is greatest for a spherically shaped aggregate, (ASP = 1), while it is lower for a cylindrically shaped aggregate (ASP < 1), and decreases with increasing aspect ratio (i.e. for longer cylinders).

2.7.1.4 Syllectometry Method

The aggregation index (AI) is determined using an optical detection based on the intensification of light transmitted through RBC aggregates [64]. Higher aggregation leads to form larger spaces between the aggregates (rouleaux) allowing more light to pass within the gaps separating aggregates. For precise measurement of RBC aggregation, RBC aggregates should be completely disaggregated prior to measurement by applying a high shear rate for few seconds. Shin et al 2009 [64] used a rotating stirrer for 10 seconds in a microchip in order to disaggregate the RBC aggregates. After stopping the rotating stirrer, the dispersed RBCs start to form aggregates. The intensity of the light transmitted through the blood sample is recorded over time, as shown in Figure 2.17.

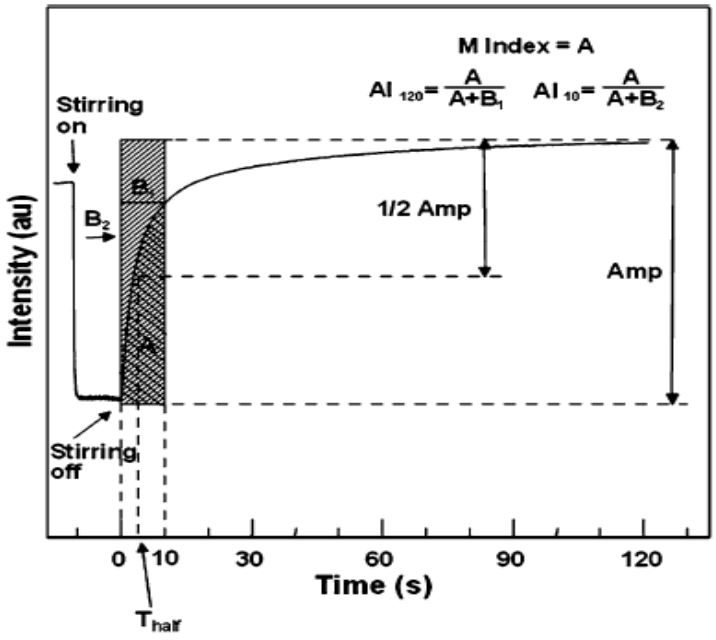

Figure 2.17: Syllectogram and aggregation indices [64].

In Figure 2.17, M-index represents the area below the syllectogram over 10 seconds, indicating the degree of the aggregation within 10 seconds. The amplitude (AMP) represents the difference between the minimum light intensity and the light intensity at either 10 s or 120 s, indicates to the extent degree of RBC aggregation. The half time (T_{half}) is the required time to reach a half light intensity of (minimum intensity + AMP), indicating the typical time constant to reach the half level of aggregation.

The aggregation index (AI) is then calculated as the ratio of the area below the syllectogram curve (*A*) to the total area (*A*+*B*) over either a 10 second or 120 second time-period (AI_{10}, AI_{120}), indicating the normalized degree of RBC aggregation. In the present study, a 120 second time period was used.

Among the above mentioned methods for measuring the RBC aggregation, in the present study, the AI of the whole blood samples was measured based on the light transmission techniques using a RheoScan AnD300 aggregometer (Rheomeditech, Inc., South Korea), and the aggregate size was determined using image analysis technique. A detailed description is presented in the next chapter.

2.8 Shear Rate in Blood Rheology

The shear rate is an important parameter influencing RBC properties such as RBC aggregation and deformation, which reflect changes in the formation of CFL and hence the blood viscosity. Shear rate γ can be defined as the change of the flow velocity between adjacent fluid layers [65].

$$\gamma = du / dy \qquad (2.4)$$

where, *u* is the velocity in flow direction and *y* is the distance from the wall [66]. As the fluid flows in a vessel or a channel, its velocity increases, on average, from zero at the wall to a maximum value at a certain distance from the wall [67]. The shear rate is maximum at the wall and decreases toward the centerline of the vessel and is zero where the velocity is maximum [68,69].

In vivo, the average shear rates are higher in small vessels like the arterioles and capillaries, and lower in large arteries and venules. Values of shear rate for several vessels in human circulatory system were presented previously in Table 2.1.

It is important when modeling microvessel flow *in vitro*, that the shear rate be matched to physiological ranges to ensure that flow conditions are close to those occurring *in vivo*. Too high of shear rate can damage or even destroy RBCs and release their hemoglobin to the plasma (a

condition called hemolysis); *in vivo* this limits the transportation of oxygen to the target organ or tissue resulting in an anemic condition. Elevated levels of shear can also activate the platelets in blood [70], which initiates thrombus formation [71]. Higher shear rates also cause RBCs to become more deformable lowering the blood viscosity [20]; sheared RBCs release adenosine triphosphate (ATP) which is believed to regulate the RBCs deformability and maintain their surface area to volume ratio [3]. At high shear rates, the ATP induces the release of nitric oxide (NO) from nearby endothelial cells. NO causes relaxation of smooth muscles and dilate the vessel walls in order to regulate the blood pressure [16]. Conversely, low shear rates allow RBCs to form large aggregates (rouleaux). This aggregation disrupts the blood flow and increases the apparent viscosity [18,66]. However, increasing the shear rate forces RBCs to reversely disaggregate and hence the viscosity is reduced [18,66].

In previous studies, shear rate has been calculated from the velocity profile measured by µPIV [5,34,35]. Details about the µPIV technique will be presented in the next section. Anastasiou et al. 2010 calculated the wall shear rate using the slope of the velocity profile near the vessel wall, and recommended using at least two, and ideally three velocity measurements near the wall as shown in Figure 2.18 [66].

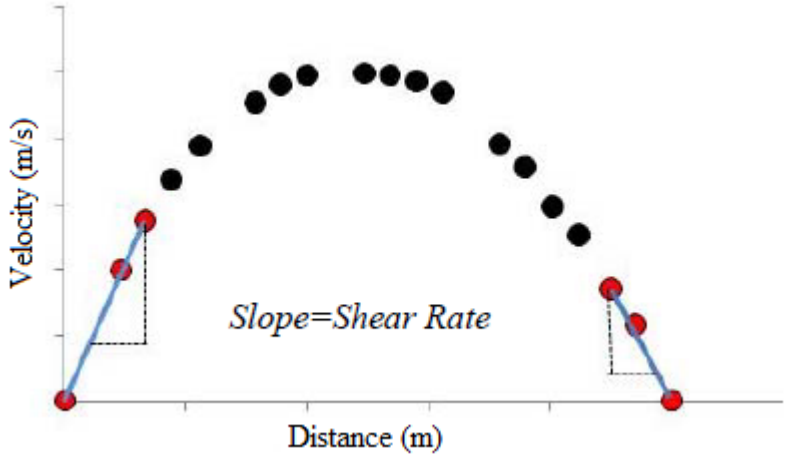

Figure 2.18: Wall shear rate calculation from velocity data [66].

Furthermore, from the velocity profiles essential information such as the maximum velocity at the vessel center and the blood flow can be found. Velocity and flow rate measurements are useful for monitoring perfusion level. Specifically, information about the RBCs' central velocity is important in cases which involve exchange between RBCs and the surrounding tissues.

2.9 Micro-Particle Image Velocimetry for Research in Blood Rheology

Developed by Santiago in 1998, micro-particle image velocimetry (µPIV) has been an important technique used in many *in vivo* and *in vitro* studies of microfluidic flow to measure important parameters such as shear rate [72]. µPIV is a flow visualisation technique which requires tracer particles in order to track the fluid flow inside the microvessel or microchannel. It determines the displacement of these particles using a cross-correlation technique. These tracer particles are either naturally present particles like RBCs or they can be artificially introduced (e.g. polymer spheres) [74]. A typical µPIV system consists of a microscope (upright or inverted) equipped with the proper optics, an illumination source, a digital camera, a computer, a microfluidic device, and a dichroic mirror to direct the light toward the digital camera [74]

Several researchers have used the µPIV to study blood flow *in vivo*. Bishop et al. 2001 studied the effect of RBC aggregation on velocity profiles in venules under control and reduced flow, and concluded that aggregation blunts the velocity profile and increase the flow resistance [73]. Due to the complexities of the microvascular networks, other researcher investigated the blood flow *in vitro*, in which conditions can be better controlled or designed for, such as the vessel size, flow rate and hematocrit. Pitts and Fenech, 2013 compared the velocity profiles of 10% H porcine blood flowing in a PDMS microchannel. Those profiles were produced by µPIV using both a high-speed camera and a pulsed camera. RBCs were used as tracer particles with the high-speed camera while fluorescent micro-particles were used with the pulse camera. The direct comparison suggested that the use of the pulsed camera with the fluorescent micro-particles provided higher maximum velocity, higher shear rate and more accurate wall shear rate [35].

In this study, the µPIV is used in order to measure the velocity profile and then determine the actual flow rate and shear rate. The later will be related to the measurements of CFL and the size of RBC aggregates.

2.10 Conclusion

The study of the rheology and the dynamical flow characteristics of blood is very important for understanding and predicting blood flow properties at the micro level, as well as for clinical diagnosis, and patient monitoring [31]. The hemodynamic properties of blood is influenced by different parameters such as the blood flow rate, hematocrit (H), RBC aggregation and the size and

the shape of the blood vessel. Of particular importance is the formation of CFL at the microscale as this CFL affects blood viscosity and adds an extra barriers to the gas exchange, waste removal and nutrient and drug delivery processes occuring at the microcirculation.

To our knowledge, no previous study has quantified CFL thickness and related it with the size of RBC aggregates and the shear rate at the wall. In this research, we will investigate the formation of CFL under low shear condition. Based on the theory of droplet migration in the two phase flow, we hypothesis that, at low shear rates, cell-cell interactions between RBCs are reduced, decreasing cell diffusion and increasing their migration toward the center, resulting in a larger CFL thickness. Additionally, RBC aggregation which occurs only at low shear rate levels [21] effectively increasing the RBCs' particle size. We also hypothesis that these larger clumps of cells experience stronger lift forces, also increasing their net motion towards the centre and increasing the CFL thickness. As the shear rate increases, large aggregates are broken up into smaller ones. This reduction in the aggregate size might lower their tendency to migrate toward the center, thus decreasing the CFL thickness.

When investigating the formation of the CFL, it is important to take into consideration the following parameters: the range of shear rate, the particle size (single or aggregating RBCs), the concentration of the RBC (H %) as well as the vessel diameter and geometry. The findings would lead to an improved understanding of blood flow characteristics in the microcirculation and could be used to enhance the design and performance of blood microfluidic devices, such as the artificial lung. Moreover, the findings can be implemented in mathematical modeling and simulation of blood flow.

Chapter 3
Materials and Methods

This chapter covers the materials, equipment and methodologies used in the experimental work in order to measure CFL thickness and RBC aggregate size, and determine the blood flow velocity profile and shear rate at the wall.

3.1 Microchannel Fabrication

3.1.1 Mask Design

Three different microchannels were designed: one straight microchannel and two bifurcating microchannels with 35° and 75° bifurcating angles, respectively. The intended dimensions of the channel cross-sections were 100 µm in width by 34 µm in height, so as to produce a representative hydraulic diameter (D_h) of 51 µm. D_h is calculated as follows [75]:

$$D_h = (4wh)/2(w+h) \qquad (3.1)$$

where, w and h are the channel width and height, respectively. The resolution of the microfabrication was on the order of ±2 µm. The mask was drawn using an AUTOCAD program [24]. The design was then sent to CAD/Art Services, Inc. to be printed on a transparency photomask. Figure 3.1 illustrates the three different microchannel designs and their cross- section.

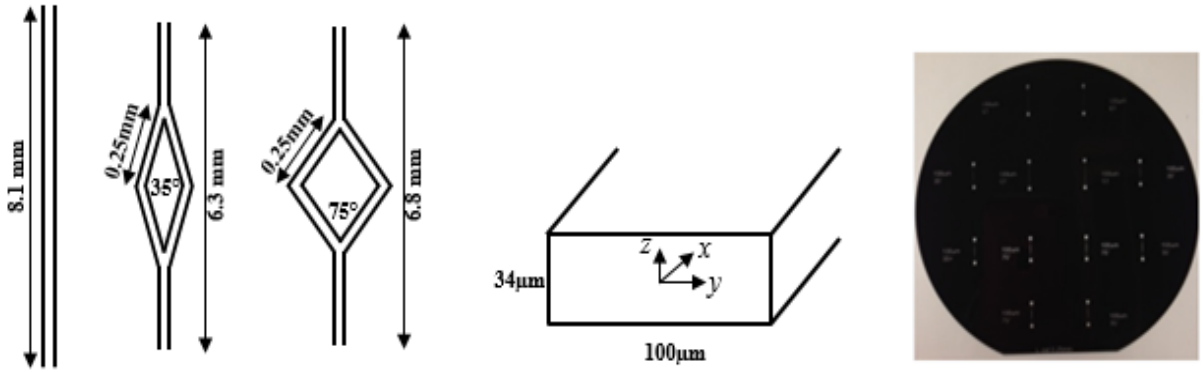

Figure 3.1: The blood microchannels design (left), their cross- section (center) and the printed mask containing 4 channels of each geometry with 100 µm wide (right).

3.1.2 Mold Fabrication

For accurate mold fabrication, soft lithography and SU8 photoresist was utilized [24,30,76,77]. The soft lithography method is described in detail as follows and illustrated in Figure 3.2.

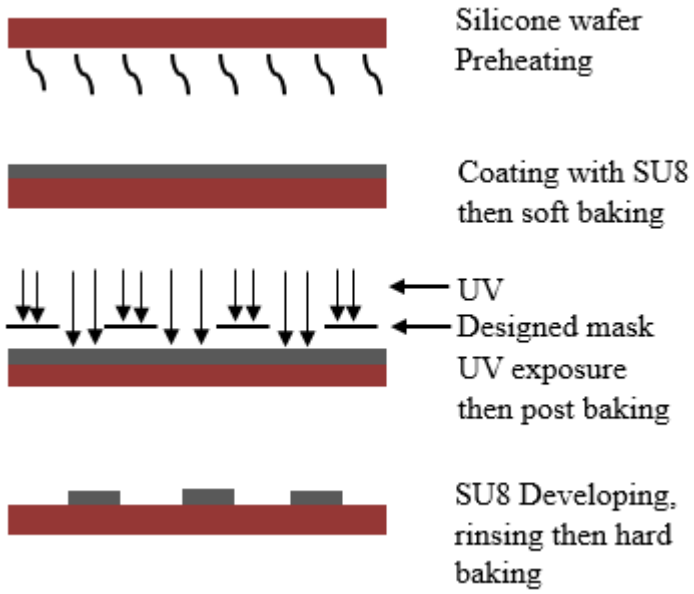

Figure 3.2: The fabrication process of SU-8 mold.

First, 4" silicon wafer was cleaned with hydrofluoric acid, and dried with compressed nitrogen. Then the silicon wafer was heated in an oven for 5 minutes at 200 °C to evaporate any solvents. After that, a coating of SU-8-10 photoresist was spun onto the wafer at 1000 rpm for 30 seconds to obtain the required thickness of 34. The thickness of the SU-8 layer was critical as it determined the height of the microchannels [78]. The coated wafer was soft-baked for 3 minutes at 65 °C followed by 7 minutes at 95 °C to remove solvent from the SU-8 photoresist. Then, the mask was aligned with and mounted onto the wafer and the assembly was exposed to UV light for 53 seconds. The UV light hardened the photoresist that was exposed by the mask. The optimal dose of UV exposure depends on the film thickness (thicker films require higher dosage) [78]. The exposed wafer was post-baked for 1 minute at 65 °C, then 3 minutes at 95 °C.

Under the fume hood, the wafer was dipped into SU-8 developer (MicroChem, USA) for 4.5 minutes, and agitated while developing. This step removed the excess of SU-8 while leaving the channel pattern that had hardened. The wafer was rinsed with isopropyl alcohol and deionized (DI) water and dried with compressed nitrogen. Finally, the patterned wafer was hard-baked at 180 °C for 10 minutes to stabilize the microchannel pattern.

3.1.3 PDMS Microchannels Fabrication

Poly-dimethylsiloxane (PDMS) is a soft polymer; its properties make it suitable for miniaturized bioassays [24,76,79].

To make the PDMS microchannel, a mixture of 10:1 PDMS elastomer and curing agent (Sylgard 184, Dow Corning, USA) was prepared and mixed under a fume hood for about 5 minutes [30,77,80,81]. The mixture was poured onto the patterned wafer and degassed under vacuum for 30 minutes in order to remove air bubbles. The PDMS mixture was cured using a hot plate at 60 °C for 90 minutes, and then left to dry for 24 hours. The dry silicon was then peeled away from the mold, revealing the formed microchannels. The resulting PDMS disc comprised 12 individual channels, which were each cut out and separated. Inlet and the outlet holes were punched into each microchannel, 1.5 mm in diameter. Using an oxygen-plasma system (Plasma Etch, USA) [82], each microchannel chip was bonded to a glass slide which enclosed the channel by creating a fourth wall. Figure 3.3: illustrates the processes of PDMS casting, curing and bonding to form the enclosed blood microchannels.

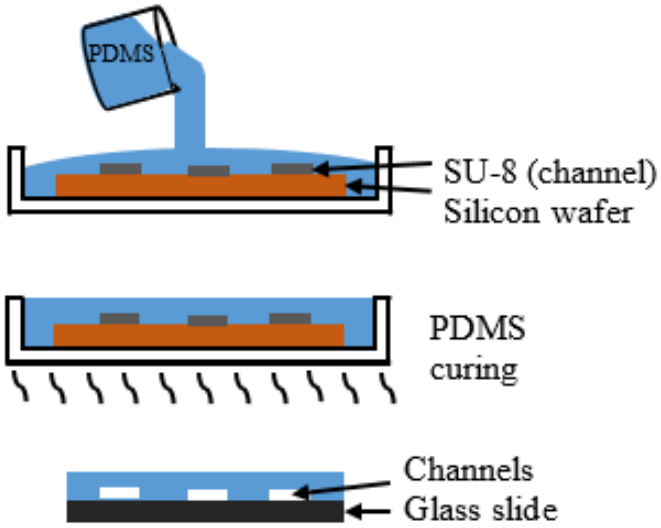

Figure 3.3: Steps to make PDMS microchannels.

3.2 Working Fluid Preparation

This experimental work involved working with deionized water (DI) and human blood. In order to work with human subjects, ethics approval was obtained from the Ethics Committee of the University of Ottawa - File number H11-13-06.

DI water was used as a Newtonian reference fluid for the velocity profile measurements. Fresh human blood samples were collected from healthy adults at an accredited clinic. To prevent coagulation, each blood sample was collected in heparinized tubes. The experiments were performed within 8 hours after blood collection at room temperature. First, the aggregation index (AI) of the whole blood was measured using a RheoScan-AnD 300 aggregometer (Rheomeditech, Inc., South Korea) by means of optical detection, using the light transmission technique [64]. Second, blood was centrifuged three times at 3000 rpm for 10 minutes, separating the blood into 3 layers: Plasma, buffy coat (which contains the platelets and white blood cells), and RBCs. After the first centrifugation, the buffy coat and plasma were separated from the RBCs. The buffy coat was separated and discarded in order to prevent blood from clotting, while the plasma was collected and saved. For the two successive centrifugations, phosphate buffer saline (PBS) was added to the remaining blood to ensure the removal of any remaining WBCs and platelets. The native plasma is filtered using 0.2 μm plasma filter (Nylon, Non-Sterile, Fisher Scientific, Ireland). The RBCs are then re-suspended in the filtered native plasma at 10% hematocrit (H). The hematocrit of the blood samples is verified by filling a capillary tube and centrifuging it in a microhematocrit centrifuge (CritSpin, Thermo Fisher Scientific Inc., China).

In order to perform the μPIV measurements, fluorescent tracer particles (Fluoro-Max, USA) with particle diameter 0.87 μm and density 1.06 g/cm^3 were mixed the working fluid (DI water or 10% H blood) at a concentration of 60 μL per 1 mL fluid.

3.3 Flow Visualization Set-up

The experimental set-up (Figure 3.4) consists of a micro-particle image velocimetry (μPIV) (La Vision MITAS) coupled with a high-speed camera. The μPIV utilizes a MITAS fluorescent microscope (La Vision, Gmbh, Germany) using an objective lens of either 20X or 40X (LD Plan-Neofluar, Zeiss, Germany) depending on the measurement type. The numerical aperture is 0.45 for the 20X lens and 0.65 for the 40X lens.

The fluorescent microscope is mounted on a three axis (*x*-*y*-*z*) movable stage, controlled via Davis Imaging Software (LaVision Gmbh, Germany); this enables preforming measurements at any location in the microchannel.

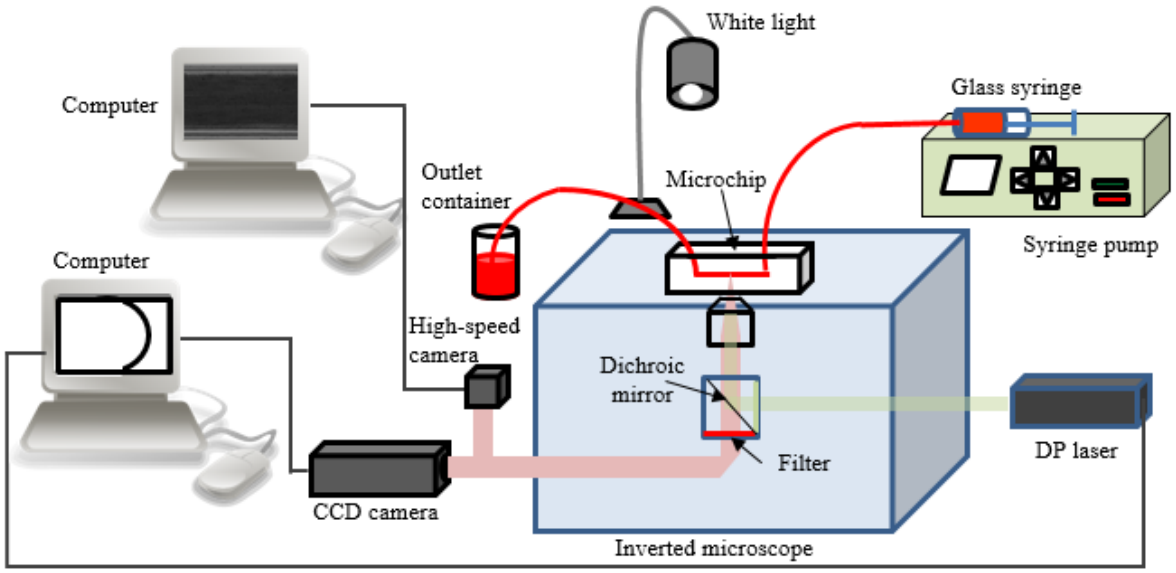

Figure 3.4: The micro-particle image velocimetry (μPIV) with a high-speed camera.

The μPIV uses a charged coupled device (CCD) camera (LaVision, Gmbh, Germany) and a Nd:YAG laser source (New Wave Research, USA) which emits a wavelength λ= 532 nm. The laser, which was used to excite the fluorescent particles, was controlled by programmable triggering unit. A dichroic mirror is used to direct the laser toward the measurement location in the channel.

For the CFL measurements, a near infrared high-speed camera (Graftek Imaging, Inc., Austin, TX, USA) and a white light source were used to illuminate the field. The high-speed camera records at 160 frames per second. A red filter was employed to enhance the contrast of the RBCs or the red fluorescent particles.

Both the CCD and high-speed cameras were mounted on a dual camera port; this port enables directing the light path to only one of the two cameras. All the system components are controlled by two computers, one computer for the μPIV and the other for the high-speed camera.

The working fluid was drawn into a 25 μL glass syringe (Hamilton, USA) which was mounted in the syringe pump, and positioned so that it was at the same level as the microchannel in order to prevent or reduce settling of the RBCs. The working fluid is injected into the microchannel of 34 μm x100 μm at the employed flow rate via a precision syringe pump (Nexus3000, Chemyx Inc., USA) at one of the three programmed flow rates, 6 μL/hr, 12 μL/hr, or 18 μL/hr.

3.4 Experimental Measurements

3.4.1 Measurement of Cell-Free Layer Thickness

For the measurements of the CFL thickness, the high-speed camera enables visualisation of the red blood cells in the flow. Initially, the choice of the objective lens magnification is made based on the type of investigation. A 40X magnification objective lens is chosen for this application. Calibration of the objective lens is essential to ensure that the CFL thickness measurements are as accurate as possible. The resolution using the 40X objective lens is 8.48 pixel/micron. The prepared blood sample of 10% H (10% RBCs and 90% native plasma) is drawn in a glass syringe and injected into the microchannel at fixed flow rate (6 µl/hr, 12 µl/hr, or 18 µl/hr) by using a precise syringe pump. The microchannel is then mounted on the movable stage.

The focus was adjusted until the microchannel walls appeared sharpest and the RBC core defined, 500 images were recorded. Each captured image was 2040x1088 pixels in size, equivalent to a 240x130 µm field of view. Figure 3.5: shows an image for the blood flow within a microchannel, captured at 160 frame/s and 0.7ms exposure time.

The images from each recording were processed using a MATLAB program which detected the CLF region, between the microchannel wall and the RBCs core based on the image pixel intensity. The program also calculated the area of the CFL region, which it divided by average calculated length to compute the average width or thickness of the CFL.

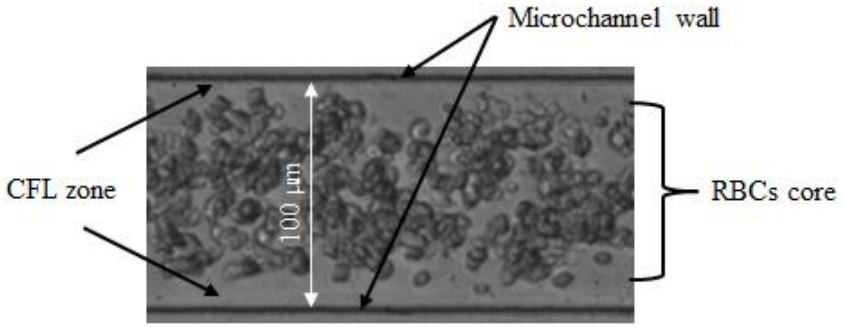

Figure 3.5: High speed camera image of blood flow into a microchannel. RBCs are concentrated in the central region and a CFL is developed near the wall.

The flow chart in Figure 3.6 depicts the processing steps. For each record, between 50 and100 images, denoted $I_{original}$ (Figure 3.6 (a), were superimposed in a stack. For each pixel coordinate in the field of view, the pixel in the stack having the lowest intensity was chosen to build the new image, I_{min}:

$$I_{min}(x,y) = Minimum\ (I_{original}(x,y,t)) \qquad (3.2)$$

where, x, y and t represent the position of the pixel in space (in x and y directions) and in time (number of image in the stack).

The resulting image I_{min} provides a clear visualization of the RBC core (darkest region in the image), the microchannel walls, and the CFL as shown in Figure 3.6 (b).

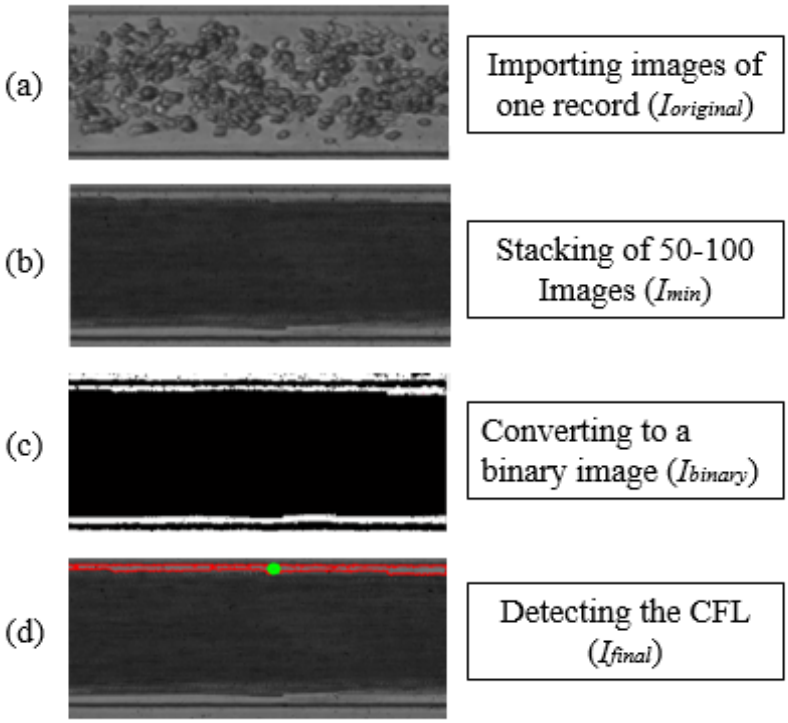

Figure 3.6: Flowchart of the MATLAB image processing code to detect the CFL thickness. (a) The original high-speed camera images, (b) minimum intensity of the stacked images, (c) converted binary image, (d) identified CFL boundary superimposed on the minimum intensity image. The green circle marks the center of mass of the CFL.

This minimum intensity image is then converted into a binary image, I_{binary} (Figure 3.6 (c)), based on a global threshold value T as follows:

$$I_{binary}(x,y) = \begin{cases} 1 & if\ \ I_{min}(x,y) > T \\ 0 & if\ \ I_{min}(x,y) \leq T \end{cases} \qquad (3.3)$$

where, the global threshold T, was adjusted for each set of images to obtain a dark region corresponding to the RBC core in image I_{min}. The CFL area was then identified as the space between the microchannel walls and the RBC core on either side of the channel.

To confirm that the CFL region was correctly identified, the boundaries of the CFL were superimposed onto the minimum intensity image (I_{final}) as shown in Figure 3.6 (d). The average

CFL thickness was calculated as the measured CFL area in squared-pixels divided by the CFL length in pixels. The CFL thickness in pixels is then converted to micrometers based on the image resolution.

3.4.2 Measurement of RBC Aggregate Size

RBC aggregate size detection is performed using the same images which were captured with the high-speed camera (Section 3.4.1).

The 500 captured images of each record were processed with a MATLAB program that detected RBC aggregates based on image pixel intensity. The program calculated their areas and categorized the aggregates by their size. Figure 3.7 shows a high speed camera image for the blood flow into a microchannel, where the RBC aggregation can be clearly seen.

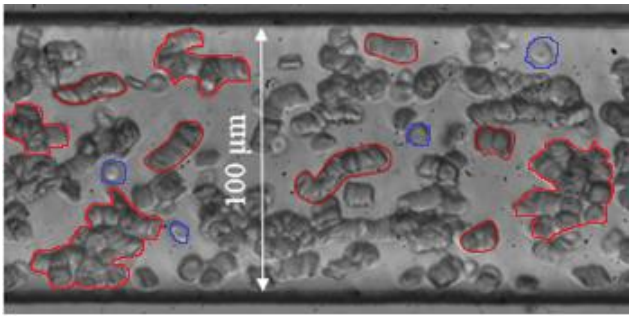

Figure 3.7: A high speed camera image, of blood flowing into a microchannel, showing individual RBCs (blue) and RBC aggregates of different sizes (red).

The size of the window captured is about 240x130 µm^2, allowing the visualization of several aggregates. The flowchart in Figure 3.8 depicts the processing steps. First, each original image, $I_{original}$ (Figure 3.8 (a), was cropped, then all 500 pictures were averaged to generate the image background, (Figure 3.8 (b)). The background image was then subtracted from the original image (Figure 3.8 (c)). This step helps reduce the background noise of the image that comes from impurities on the optic lens and microchannel fabrication. The subtracted image, $I_{subtracted}$ was converted into a binary image (black and white) I_{binary} (x; y) according to a set threshold T as follows:

$$I_{binary}(x,y) = \begin{cases} 1 & if \ \ I_{subtracted}(x,y) > T \\ 0 & if \ \ I_{subtracted}(x,y) \leq T \end{cases} \qquad (3.4)$$

The threshold T, was chosen for each test based on the visual assessment of the aggregate detection. The binary image was then dilated to improve the detection of the aggregate edges

(Figure 3.8 (d)). Due to variation of the light distribution, converting the subtracted image into a binary image sometimes resulted in an incomplete detection of the aggregates.

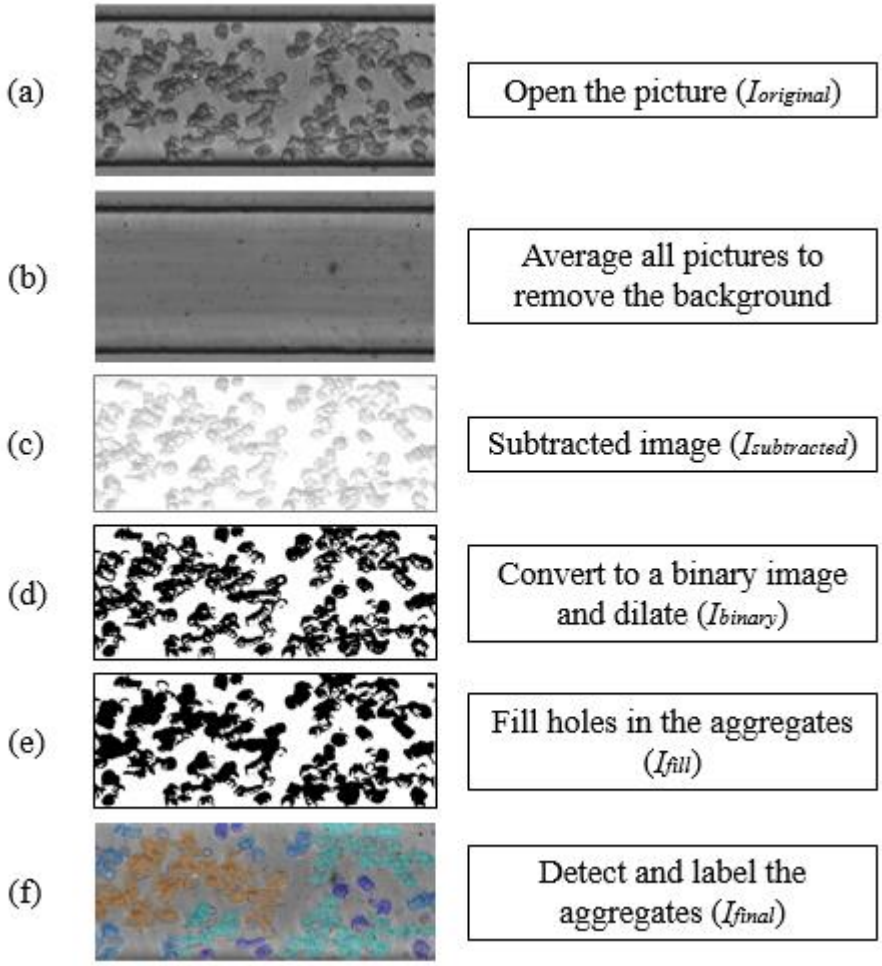

Figure 3.8: Flowchart of the MATLAB image processing code to detect the aggregate size of flowing RBCs into a microchannel. (a) The original high-speed camera image, (b) background image, (c) subtracted image, (d) binary image, (e) enhanced image, (f) final image showing color labeled aggregate based on their size.

In such situations, the missing areas, or "holes", were filled so that the full aggregate size could be estimated; the corrected images were denoted I_{fill} (Figure 3.8 (e)). The aggregates were then detected and labeled based on their size. The labeled image was converted into a red-green-blue (RGB) image for enhanced visualization. The processed image was superimposed on the original image in order to verify the consistency of the image processing. This final image, I_{final}, is shown in Figure 3.8 (f). The colour coding in this image was based on the detected aggregate sizes in

pixels and uses the “jet" colour map. Table 3.1 provides the range of the aggregate area and the corresponding colour in the image.

Table 3.1: The colour coding for detecting aggregates based on their area.

Aggregate area (μm^2)	Colour
>100	
100-499	
500-999	
1000-1499	
1500-1999	
2000-2999	
>3000	

For each image the average aggregate size was calculated from the sizes of all RBC aggregates in the image. The average sizes for one test are shown in Figure 3.9. These were then averaged for the full recording. The aggregate areas were detected in pixels and then converted to μm^2 based on the calibration factor.

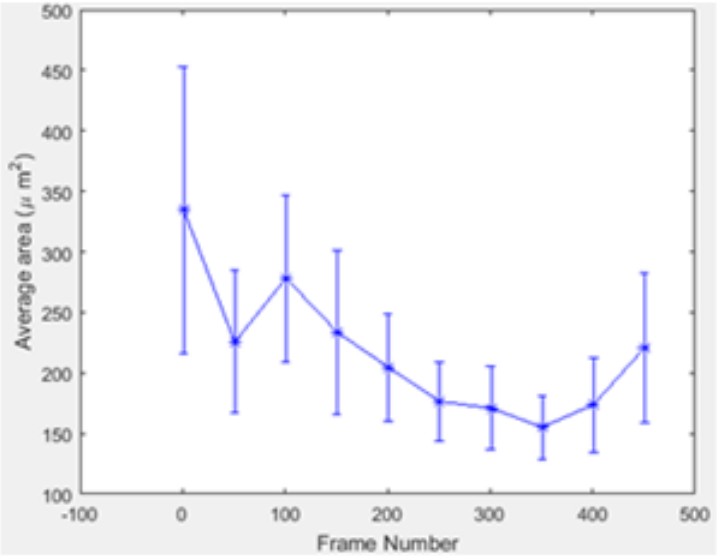

Figure 3.9: The average aggregate size for one test of 500 images. The bars represent the standard deviation.

3.4.3 Measurement of 2D Velocity Profile

The flow velocity was measured with the µPIV. For measuring the velocity profile, a 20X magnification objective lens was used. From the velocity profiles, the maximum velocities, actual flow rates, and wall shear rates were determined. The image resolution using the 20X lens was 4.18 pixels/micron. The fluid sample, (either DI water or 10% H blood), was seeded with

fluorescent particles and gently mixed. The seeded sample was drawn into a 25 µl glass syringe and injected into the microchannel at fixed flow rate (6 µl/hr, 12 µl/hr, or 18 µl/hr) via the syringe pump. The microchannel was placed on the movable stage, and the laser was triggered to illuminate the fluorescent particles. The stage was positioned to locate the center-plane of the channel; it was necessary to make the measurements at the centre-plane so that the maximum fluid velocity would be recorded. In order to ensure preforming the measurement at the center-plane location, the velocity measurements were made at different planes across the microchannels by traversing the measurement plane in discrete steps via the stage control. Furthermore, those velocity profiles from different planes combined to provide a 3D reconstruction profile of the flow. An example of a 3D reconstruction profile for DI water will be presented in Chapter 6.

For each of the tested flow rates, the time interval between the two successive images (*dt*) was adjusted so that the fluorescent particles traveled between 5-10 pixels between the successive images. For each test, 100 pairs of images were recorded. Figure 3.10 shows the CCD camera images for the tracer particles flowing within the microchannel in both DI water and in 10% H blood.

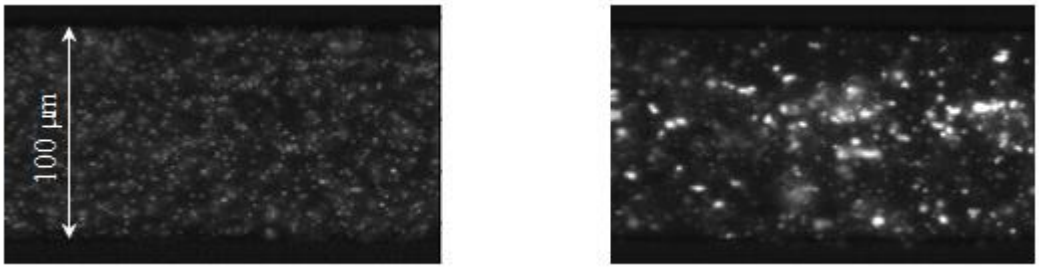

Figure 3.10: CCD camera images for the tracer particles flowing within the microchannel in: DI water (left) and 10% H blood (right).

When using DI water the tracer particles were distributed evenly. While using blood, due to the presence of RBCs, the particles tended to clump together. These clumps tended to migrate toward the walls, resulting in a lower particle concentration at the channel center and causing particles to stick to the channel walls [83]. Also, as the RBCs were much larger than the tracer particles, some particles were partially hidden from view by the RBCs resulting in blurry particle images.

3.4.3.1 Processing of Fluorescent Images

The images were then processed using a cross-correlation algorithm [83] which determined the particle displacements between two successive images. The 2D cross-correlation (Φ_{CC}) is given by the equation:

$$\Phi_{CC}(m,n) = \sum_{x=1}^{P} \sum_{y=1}^{Q} f(x,y) g(x+m, y+n) \qquad (3.5)$$

where, m and n are the displacement components, P and Q are the sizes of the interrogation window in x and y directions respectively, and f and g are the functions of image intensity [84].

The interrogation window size and shape were chosen such that each window contained sufficient numbers of tracer particles (~10). The correlations were made using multiple passes, using an initial interrogation window size of 64 × 64 pixels followed by 32× 32 pixels for subsequent passes. An overlap of 50% was used between neighboring interrogation windows to improve the accuracy. Oval-shaped windows were used (of a ratio 4:1), with their long dimension aligned with the flow, in order to achieve a higher vector resolution. The time between frames (*dt*) is about 700 µs, 1200 µs, 2200 µs for programmed flow rates of 18 µl/hr, 12 µl/hr, and 6 µl/hr respectively.

Two cross-correlation methods were applied in this work, depending on the working fluid and the image quality. For the measurements made with the DI water, the cross-correlation was applied to the raw images, as they contained sufficient numbers of bright particles. This procedure is illustrated in Figure 3.11.

For the experiments using blood, as explained previously, the RBCs reduced the quality of the images. Following Pitts et al. 2012 recommendations [83], the images were pre-processed to improve the accuracy of the measurements by image overlapping. For these measurements, cross-correlation was performed on the overlapped images, using the maximum particle intensities. This step compensated for the insufficient number and intensity of particles, and produced a pair of images having sufficient numbers of tracer particles. Figure 3.12 illustrates the cross-correlation process for the experiments using 10% H blood.

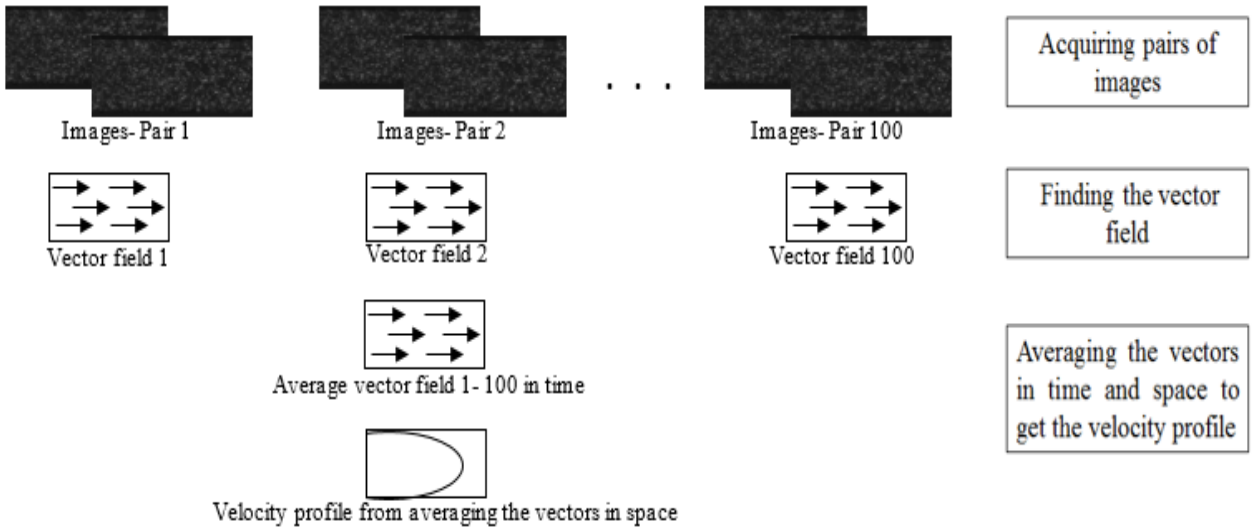

Figure 3.11: Flowchart of the cross-correlation image processing to find the velocity profile.

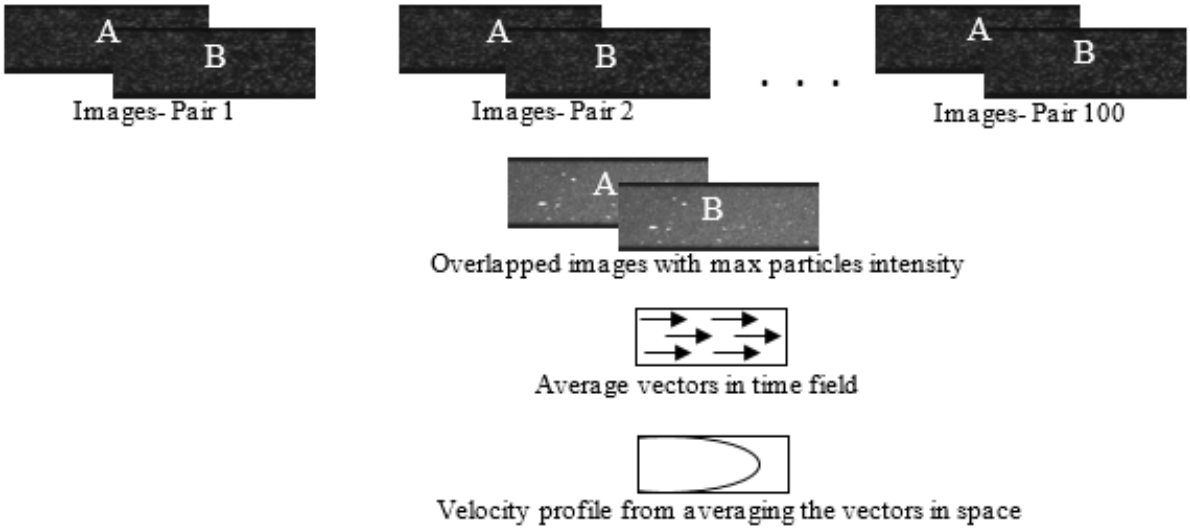

Figure 3.12: The cross-correlation steps to find the velocity profile by image overlapping.

Velocity vectors were calculated from the displacements determined by the cross-correlation. These were then averaged in time (for 100 pairs of images) and space (across the length of the visualization window) to give a representative 2D center-line velocity profile. Figure 3.13 shows the velocity field obtained from the µPIV system, for 10% H RBCs suspension flowing at 18 µL/hr.

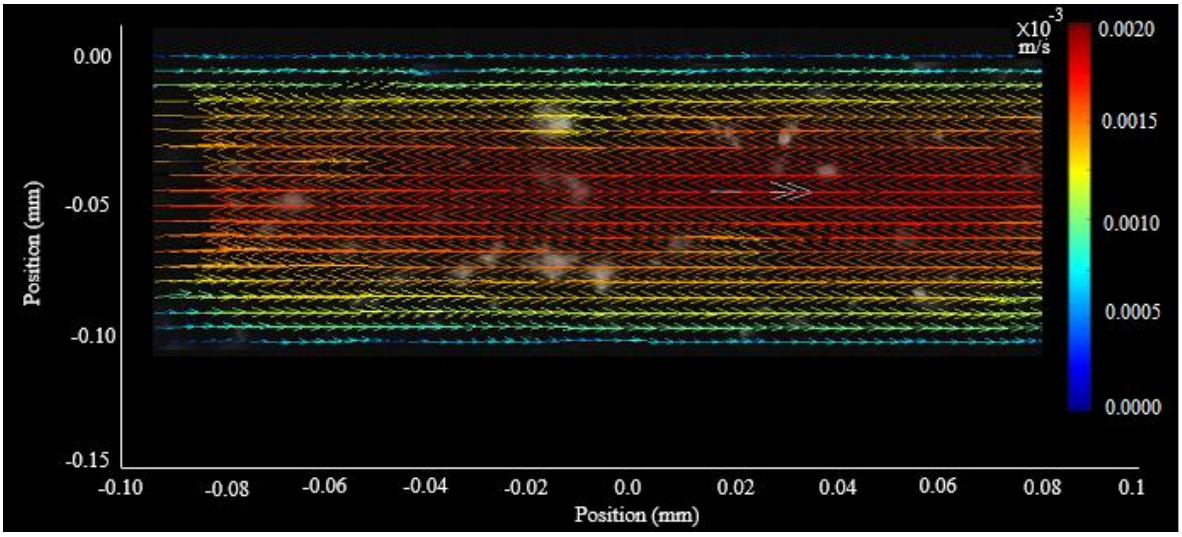

Figure 3.13: Velocity vector field obtained from the µPIV, for 10% H RBCs suspension flowing at 18 µL/hr.

In order to evaluate and validate the fluorescent image processing, 3D theoretical Newtonian velocity profile was calculated by applying Poiseuille's law for a rectangular channel [85]:

$$u(y,z)=\frac{4G}{\mu w}\left[\sum_{n=1}^{\infty}\frac{(-1)^{n+1}}{\beta^{3}}\left(1-\frac{\cosh\beta y}{\cosh\beta\frac{b}{2}}\right)\cos\beta x\right] \tag{3.6}$$

where, β is defined as:

$$\beta=(2n-1)\frac{\pi}{w} \tag{3.7}$$

where, G is the pressure drop (pressure per unit length), μ is the kinematic viscosity, w (y-direction) is the width, b (z direction) is the height. This 3D theoretical velocity profile is shown in Figure 3.14 (a)

For a rectangular microchannel with low aspect ratio (w≈h) the pressure drop can be calculated according to the pump flow rate as Eq. 3.8 [86]:

$$\Delta p=R_f Q=\left(\frac{12\mu l}{wh^{3}}\left[1-\frac{h}{w}\left(\frac{192}{\pi^{5}}\sum_{n=1,3,5}^{\infty}\frac{1}{n^{5}}\tanh\left(\frac{n\pi w}{2h}\right)\right)\right]^{-1}\right)Q \tag{3.8}$$

where, R_f is the fluidic or hydrodynamic resistance of the channel (Pa.s/m^3), Q is the total fluid flow (m^3/s), μ is the viscosity of the fluid (Pa.s), l, w, and h are the length, total width, and the height of the channels (m).

The measured velocities are expected to be lower than the ideal velocity that would result from the programmed flow rate by the pump (theoretical). This is due to the compliance in the system and the deformation of the PDMS channel.

By finding the ratio between the 2D theoretical (Newtonian) velocity profile and the 2D experimental measured velocity profile at the center of the microchannel as depicted in Figure 3.14 (b), a correction can be applied to the latter and used to estimate the 3D experimental velocity profile, according to the equation:

$$F(y,z) = u(y,z)\frac{u_{\exp}(y,z=0)}{u(y,z=0)} \qquad (3.9)$$

where, *F(y, z)* is the expected experimental profile, *u(y, z)* is the theoretical velocity obtained in Eq. 3.6, *u(y, z=0)* is the middle theoretical profile, and $u_{exp}(y, z=0)$ is the experimental centre-plane velocity in the flow direction [83].

The corrected velocity profile, called the "3D extended profile", is shown in Figure 3.14 (c). The actual flow rate Q_{calc} can then be calculated by integrating this 3D extended velocity profile across the *y* and *z* directions as:

$$Q_{calc} = \int_{y=-\frac{w}{2}}^{y=+\frac{w}{2}} \int_{z=-\frac{h}{2}}^{z=+\frac{h}{2}} F(y,z)\,dydz \qquad (3.10)$$

Also, the shear rate at the wall can be calculated from the experimental 2D velocity profile at the center-plane of the microchannel, as shown in Figure (3.14 d).

The calculated flow rate from the velocity profiles is compared with the programmed flow rate by pump to ensure accuracy of the experimental measurements. The average velocity was then calculated from the following equation [13]:

$$Q = u_{ave} * (w * h) \qquad (3.11)$$

where, *Q* is the flow rate, u_{ave} is the average velocity in the microchannel, and *w*, *h* is the microchannel width and height respectively. The average velocity was used to find the Reynolds number Re as [20,71]:

$$\mathrm{Re} = (\rho * D_h * u_{ave}) / \mu \qquad (3.12)$$

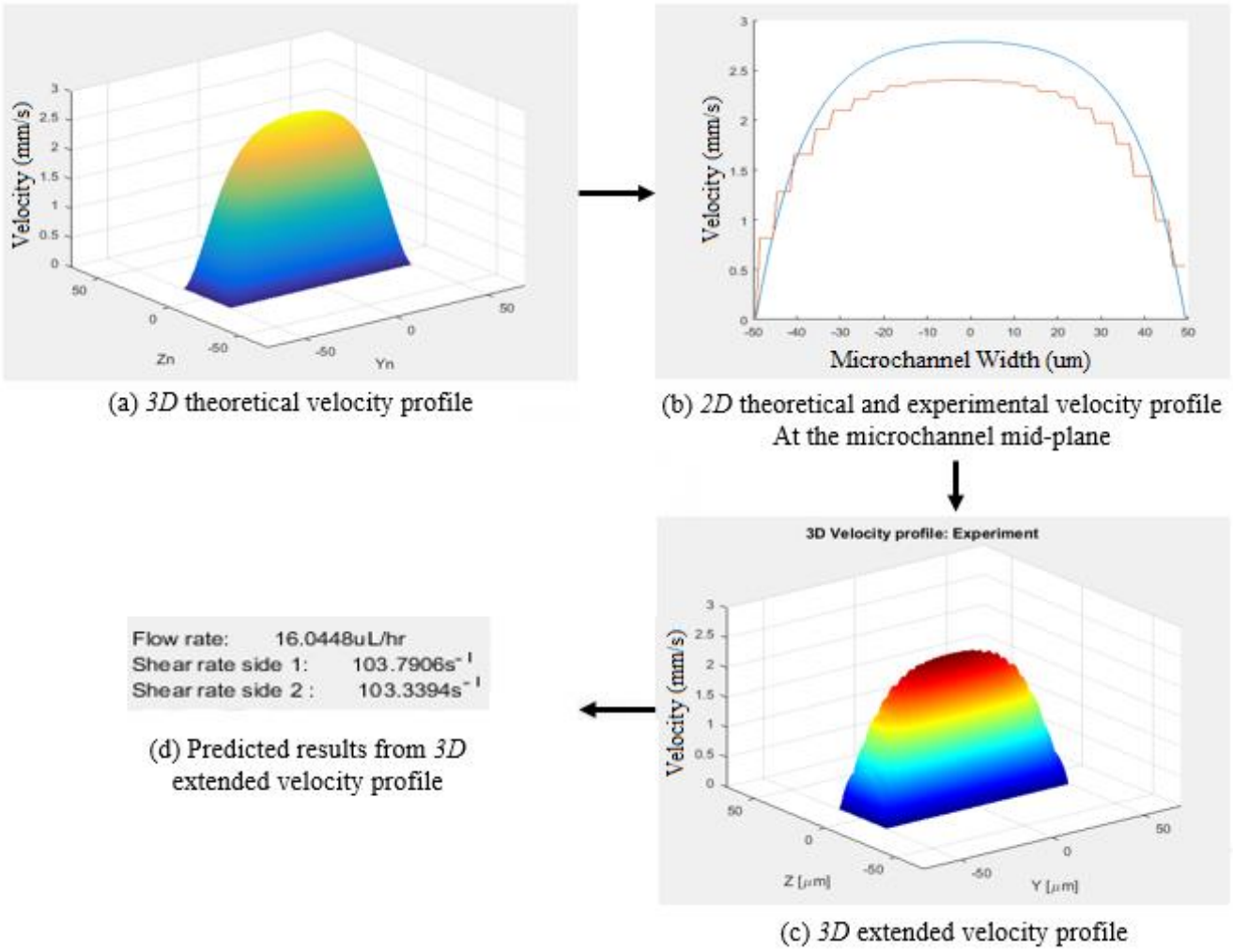

(a) *3D* theoretical velocity profile

(b) *2D* theoretical and experimental velocity profile At the microchannel mid-plane

(c) *3D* extended velocity profile

(d) Predicted results from *3D* extended velocity profile

Figure 3.14: Steps to build 3D velocity profile from 2D experimental velocity profile.

where, ρ is the fluid density (kg/m^3), D_h is the hydraulic diameter (m), u_{ave} is the average velocity (m/s), and μ is the fluid viscosity (Ns/m^2) [20,71]. The shear rate γ was calculated from the experimental velocity profile as [67]:

$$\gamma = \frac{du}{dy} \qquad (3.13)$$

where, u is the blood velocity close to the wall, y is the distance from the wall. Anastasiou et al. 2010 suggested that the wall shear rate (γ_w) calculation should consider at least two or three velocity values measured close to the wall [66], as shown in Figure 3.15. The estimated shear rate can be used to estimate the wall shear stress τ as [67]:

$$\tau = \mu * du/dy \qquad (3.14)$$

where, μ is the dynamic viscosity and *du/dy* is the shear rate or velocity gradient at the wall.

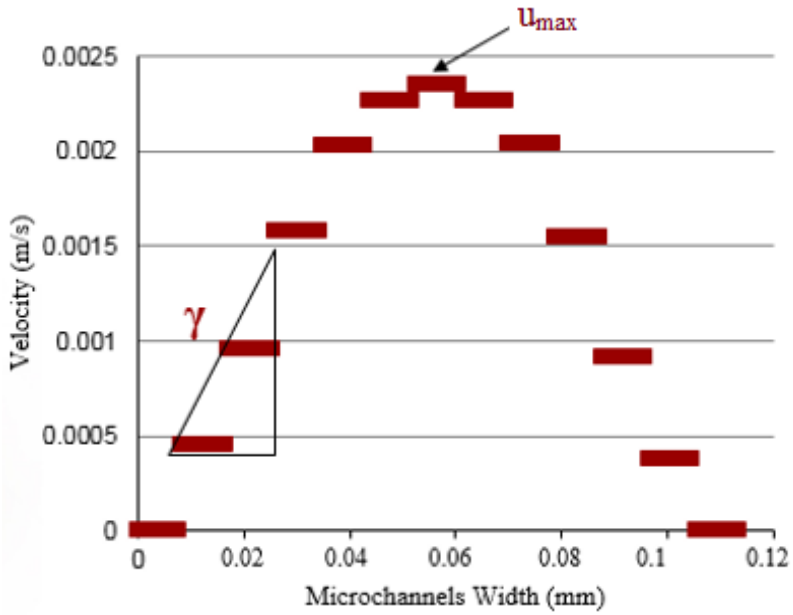

Figure 3.15: Estimation of wall shear rate using the center-plane experimental velocity profile.

In order to characterize the velocity profile, the shape factor *k* was used. This shape factor is the measure of the velocity profile's parabolic nature. For the parabolic profile of a Newtonian fluid, $k = 2$, and for blunt profile, $k > 2$ [44]. For the velocity measurements of these experiments, *k* was calculated by minimizing the difference between the two sides of the following equation [35]:

$$u_{\exp}(y, z=0) = u_{\max}\left[1-\left(\frac{|y|}{w/2}\right)^{k}\right] \qquad (3.15)$$

where, $u_{exp}(y, z=0)$ is the velocity (mm/s), $u_{\max}$ is the maximum velocity, y is the position perpendicular to the flow (mm), and w is the microchannel width (mm).

The shape factor depends on the microchannel aspect ratio *h/w*, where *h* is the microchannel depth and (*w*) is its width. Figure 3.16 displays theoretical velocity profiles, for a Newtonian fluid, using microchannels of different aspect ratio, at flow rate 18 µl/hr. Figure 3.17 shows the dependency of *k* on the microchannel aspect ratio for theoretical velocity profiles of a Newtonian fluid. The dashed line in this figure represents the aspect ratio of the microchannels used in the experimental work (~0.34), which produces $k = 4$.

In a straight microchannel the maximum velocity is expected to be at the centerline of the flow [51]. In a bifurcating microchannel, within the bifurcation, the velocity profile is dramatically skewed toward the inner wall, this is due to the centrifugal force caused by the change in the flow

direction. Also, the uneven distribution of the RBCs can result in a skewed velocity profile, and the presence of the RBC aggregation further increases the skewness [51]. The skewness of the velocity profiles (*S*) can be evaluated based on the definition proposed by Sherwood et al. 2012: as the distance between the location of the maximum velocity and the channel centerline, presented as a percent of the total channel width [51].

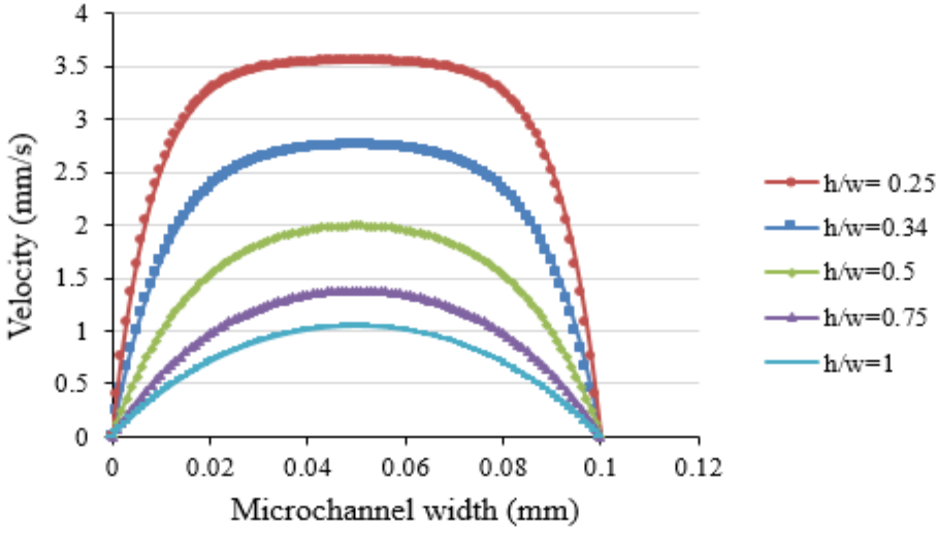

Figure 3.16: Theoretical velocity profiles for a Newtonian fluid, using 100 µm wide microchannels of different aspect ratio, at a flow rate 18 µl/hr.

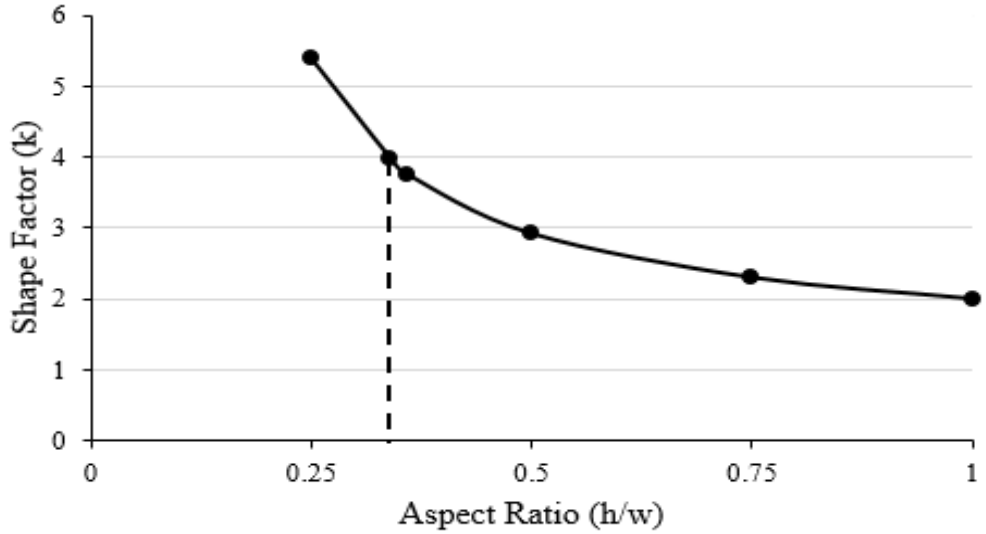

Figure 3.17: The shape factor for microchannel of different aspect ratio (h/w). The dependency of the shape factor, of theoretical velocity profiles for Newtonian fluid, on the microchannel aspect ratio (h/w). The dashed line represent the aspect ratio of the microchannel used in this experimental work (0.34).

3.5 Statistical Analysis

A two-way ANOVA followed by Tukey's multiple comparisons test was performed using GraphPad Prism (version 7.04, GraphPad Software, Inc., La Jolla, California, USA). The two-way ANOVA was conducted to examine the effects of the independent variables (flow rate, and blood donor) on the measurements of CFL thickness and RBC aggregate size. The same test was conducted to examine the effects of the change in the microchannel geometry and blood donor on the measurements. The probability $p < 0.05$ indicates a statistically significant interaction between the effects of independent variables on the measurements of the CFL thickness and RBC aggregate size.

Chapter 4

Cell-Free Layer Thickness Measurements

This chapter presents the results of the measurements made of the CFL thickness in microchannels having different geometries, and for different flow rates. First, a brief summary of the experimental procedure is described. The results are then presented along with a discussion of the CFL dependency on the flow rate and the microchannel geometry.

4.1 Experimental Set-up and Procedure

In this experimental investigation, three different microchannels were used: one straight microchannel and two bifurcating microchannels having bifurcating angles of 35° and 75°, respectively. The microchannels were initially designed with AutoCAD software, and fabricated from poly-dimethylsiloxane (PDMS) using soft lithography. Details of the design and fabrication process were presented in Section 3.1 and the microchannel geometries were illustrated in Figure 3.1.

Six samples of fresh human blood were collected from healthy adults at an accredited clinic, in compliance with the Ethics Committee of the University of Ottawa. The aggregation index (AI) of the whole blood was measured by an aggregometer (RheoScan-AnD 300) based on the light transmission technique [64]. The blood samples were cleaned and the RBCs were separated and re-suspended in the filtered native plasma at 10% hematocrit (H). This hematocrit is representative of physiological levels occurring in the microvessels (less than 20%). The procedures for blood sample collection and preparation were presented in Section 3.2.

Using the experimental set-up presented in Section 3.3 and shown in Figure 3.4, the blood samples were visualized and recorded while flowing through the rectangular microchannels. Using the high-speed camera [8,10], 500 successive images were recorded for each sample and at each flow rate. Blood of 10% H was injected into each rectangular PDMS microchannel at a constant programmed flow rate[1], by the precision syringe pump. Three different flow rates, which fall within the physiological range of microcirculation (6 µl/hr, 12 µl/hr and 18 µl/hr), were used. Figure 4.1 shows a typical image acquired for 10% H blood flowing into PDMS microchannel.

[1] The "programmed flow rate" is to be distinguished from the actual flow rate, which is lower than the programed one, as a result of the system compliance. The actual flow rate is estimated in Chapter 6.

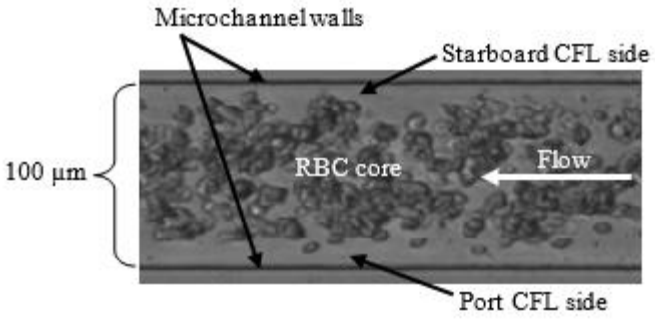

Figure 4.1: A high-speed camera image for RBCs flowing in a plasma suspension. The RBC core occupies the central region and the CFL exists at the sides of the microchannel.

The average expected velocity (u_{ave}) across the channel was calculated from the programmed flow rate (Q) and the microchannel cross-section area (A) as (Waite and Fine, 2007):

$$u_{ave} = Q / A \qquad (4.1)$$

The estimated average velocities in the microchannels were 0.5 mm/s, 1 mm/s and 1.5 mm/s, respectively. The Reynold Number (Re) was then estimated using Eq. 3.12 [75,86]. The corresponding Reynold numbers were estimated to be 0.017, 0.034 and 0.051 for flow rates of 6 µl/hr, 12 µl/hr, and 18 µl/hr, respectively. The viscosity (μ) was estimated at 0.00155 Ns/m^2 based on a viscosity curve for the employed hematocrit, and the blood density was assumed to be 1,060 kg/m^3 [13].

The apparent shear rate (γ_a) in a rectangular duct was estimated as [87]:

$$\gamma_a = (6Q / wh^2)(1 + (h/w))\, f^*(h/w) \qquad (4.2)$$

where, Q is the flow rate, w and h are the channel width and height respectively, and f^* =0.7091 is a geometric constant and function of the duct aspect ratio (h/w). The apparent shear rates corresponding to the programmed flow rates 6 µl/hr, 12 µl/hr, and 18 µl/hr, were estimated to be 28 s^{-1}, 56 s^{-1}, and, 84 s^{-1} respectively. Precise measured values of shear rate will be obtained using µPIV in Chapter 6.

The CFL measurements were performed at different locations in the channels: in the straight channel, at the midline, and the two bifurcating microchannels, before and after the bifurcation. All experiments were performed at room temperature. The image sequences recorded using the high-speed camera were processed using the MATLAB image processing toolbox using the techniques described in Section 3.4.1. Using the six different blood samples, between one and five measurements were made at each location in the microchannel for each flow condition.

Using a two-way ANOVA, a statistical analysis was conducted on the results comparing the CFL thickness under different flow conditions using different blood samples. In each microchannel, the CFL thickness was measured using blood samples from 6 donors at each flow rate, Q_1, Q_2 and Q_3. To determine the effect of the microchannel geometry, the CFL thicknesses were compared for the three microchannel geometries under the same flow condition.

4.2 Results and Discussion

4.2.1 CFL Thickness Assessment on the Opposite Sides of the Microchannels

It is known that CFL thickness is not constant and varies in time and location due to the deformation and complex motion of the RBCs [9,50]. Considering the average CFL thickness, however, provides typical information about this phenomenon. First, using the straight microchannels, CFL was measured on both sides of the microchannel for different flow rates. We will refer to the right side of the channel as "starboard", and to the left side as "port", for the channel orientation and flow direction shown in Figure 4.1. The results are presented in Figure 4.2.

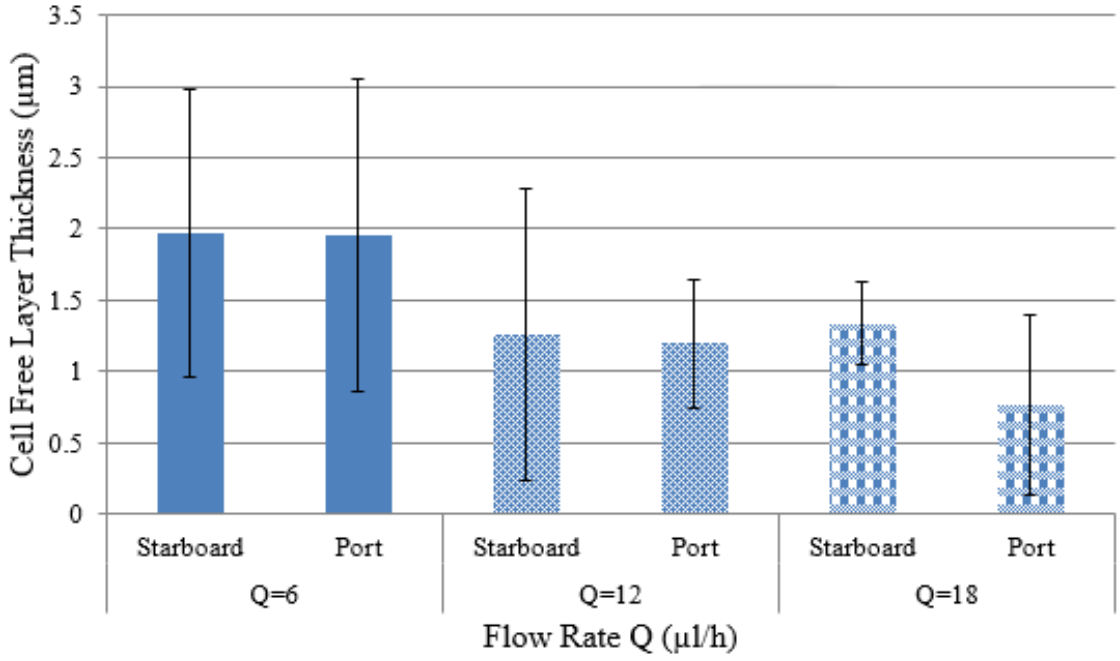

Figure 4.2: The CFL thickness (µm) versus the programmed flow rate Q (µL/hr) for the straight microchannels. Averages of 6 different blood samples are shown for each flow rate and for both sides of the microchannel (right side of the flow (Starboard) and left side of the flow (Port)).

Although we noticed a difference between the two sides for several experiments in the straight channel, there was no significant difference in CFL thickness between both sides for all flow rates; i.e., the CFL was effectively symmetric as shown in Figure 4.2. Therefore, the average CFL of both sides will be reported for the measurements made in the straight sections of the microchannels (for all three geometries).

4.2.2 Effect of Blood Flow Rate on CFL Thickness

The average CFL thickness of both sides of the microchannel wall was plotted for all different microchannel geometries at the different flow rates, as shown in Figure 4.3. It was found that, for all channel geometries, increasing the blood flow rate reduced the CFL thickness. The CFL thickness for the different flow rates were compared using a two-way ANOVA test. The statistic comparison showed a significant difference between different flow rates and revealed a significant effect of the flow rate on the CFL thickness.

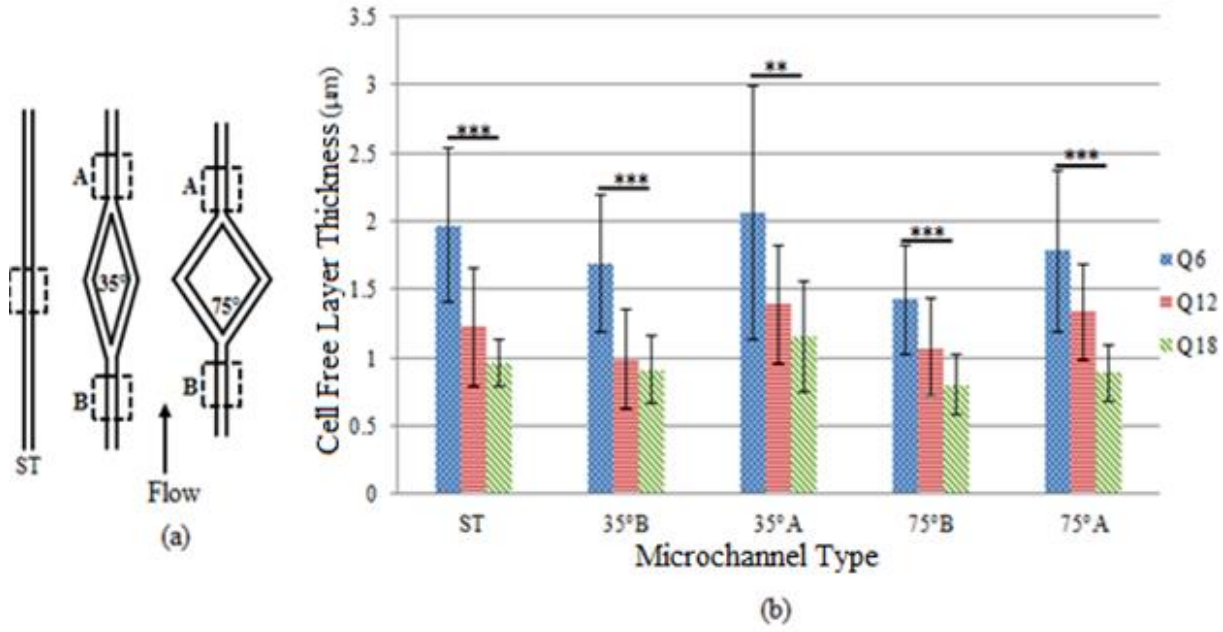

Figure 4.3: The average CFL thickness as a function of flow rate for the three different microchannel geometries at different locations. (a) The measurement positions in the three channels: the midpoint in the straight microchannel, and before (B) and after (A) the bifurcation for the two bifurcating microchannels. (b) The average CFL thickness of both sides of the microchannel wall (µm) for three different microchannels, (ST) straight, 35º and 75º bifurcating microchannels, at different programmed flow rates *Q* (µL/hr), (B) before the bifurcation, and (A) after the bifurcation. Results are averaged from 6 different blood samples, (**) P ≤0.05, (***) P ≤0.01.

This result is in agreement with the findings of previous studies [5,38,50], even though the experiments of [50] were made using 45% H blood samples, and the measurements of [5,38] were not performed in a rectangular cross-section microchannels.

We hypothesized that the reduction in CFL thickness could be explained by RBC aggregate formation and migration, which are affected by changes in the flow rate and hence, the corresponding shear rate. This theory will be discussed in details in Chapter 6, where the size of RBC aggregates will be measured and correlated to CFL thickness.

4.2.3 Effect of the Microchannel Geometry on CFL Thickness

The CFL measurement was performed at the midpoint of the straight microchannel. For the other two bifurcating microchannels, the CFL measurements were performed both before and immediately after the bifurcation, each over a length of 200 μm. The average CFL thicknesses (at both sides) for the three different microchannels geometries as shown in Figure 4.3, were compared using a two-way ANOVA test, for the same flow rates. The statistical comparison between those different microchannels geometries (all combinations) did not detect significant differences, meaning that the change of the microchannel geometry had no significant influence on the CFL thickness in the straight parts of the channels. This result corroborates the finding of Pinto et al. 2015 [10], which stated that the bifurcation has no strong effect on the CFL thickness. However, Pinto et al. 2015 used channel size of three folds larger than the one used in this work and used 15% H ovine blood with dextran instead of 10% H human blood in native plasma.

When comparing the average CFL thickness before and after the bifurcation, however, for all flow rates, an increase in the CFL thickness after the bifurcation was observed. This increase can be explained as follows: since the cross section in the bifurcation was equal to those upstream and downstream, the flow rate in the bifurcation was half of the mother microchannel flow rate, and different distributions of hematocrit resulted at the two branches. These changes could influence the RBC aggregation within the bifurcation. The multiple influences of all these factors could be the reason behind this increase after the bifurcation. Furthermore, at the very low Reynolds number used in the experiments, a liquid is expected to have a (reversible) creeping flow and an equivalent CFL upstream and downstream of the bifurcation. Here, the fact that CFL was not identical suggests the influence of RBC aggregation adding instability to the flow. Despite the

observed increasing trend, the statistical analysis comparing the CFL measurements before and after the bifurcation did not show a significant difference.

4.2.4 Effect of Bifurcation on CFL Formation

In the bifurcating channels, upstream of the bifurcation, the RBC core flowed at the channel center. At the bifurcating region, the RBC core was disturbed and split into two streams. The RBC density was high at the inner wall of the bifurcation and no CFL was observed there, while at the outer wall of the bifurcating branches the CFL was clear and was found to be larger than the CFL in the mother branch. This is illustrated in Figures 4.4 and 4.5. These asymmetry CFL observations are consistent with earlier studies [4,9], although this study was performed using blood samples of 10% H in native plasma, whereas dextran was used for Ishikawa et al. study [9], and a modeling study was performed by Li et al. [4]. Figure 4.4 shows the minimum intensity image and binary image at the bifurcation for 35° bifurcating microchannel. Figure 4.5 illustrates a quantitative measurement of the CFL thickness in the mother channel and at the outer wall of the bifurcation for the three different flow rates using 35° bifurcating microchannel. At the lowest flow rate (6 µL/hr), the difference between the mother and the daughter branches was not significant, since the CFL was already big in the mother channel, whereas at increased flow rate of 12 µL/hr and 18 µL/hr the difference was significant having $p < 0.01$. The same trend was observed when using the 75° bifurcating microchannel.

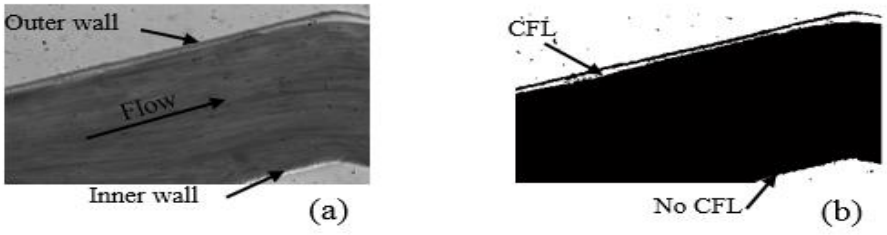

Figure 4.4: CFL formation at the bifurcation of the microchannel. The CFL formation at the microchannel bifurcation of 35º bifurcating angle: (a) the minimum intensity image and (b) the converted binary image.

The increase in the CFL thickness at the outer wall of the bifurcation can be explained by the reduction of the flow rate into the bifurcation, since the bifurcation and the mother branch have the same cross section. Lower flow rate reduces the RBC radial dispersion. This may cause the CFL to become thicker at the outer wall of the bifurcation, and persist slightly even after the bifurcation,

as was mentioned earlier in Section 4.2.3. The interpretation of the CFL at the bifurcation necessitates the knowledge of the velocity profiles and local shear. This aspect will be developed and discussed in chapter 6.

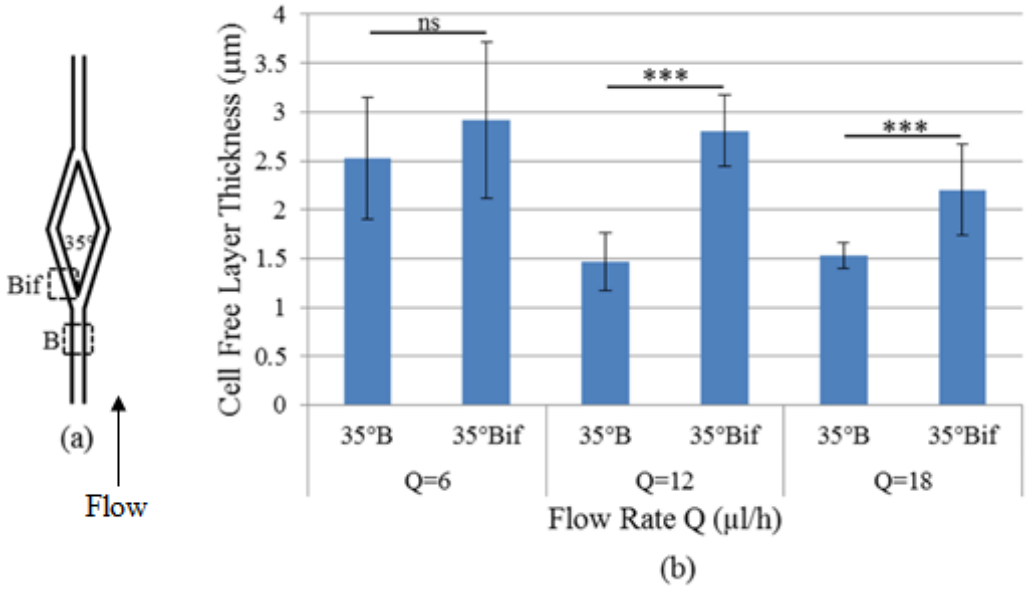

Figure 4.5: The CFL Thickness as a function of programmed flow rate in the mother and daughter branch of the bifurcating microchannel. (a) The microchannel with 35° bifurcating angle and the image recording positions. (b) The CFL thickness (µm) in the mother microchannel (35º B) and at the outer wall of the bifurcation (35º Bif) for the 35º microchannel at different flow rates *Q* (µL/hr), ns = not significant, (***) P ≤0.01.

4.2.5 Effect of RBC Aggregation on CFL Formation

The CFL thickness was plotted as a function of the aggregation index (AI) measured for the whole blood samples for each of the flow rates as shown in Figure 4.6. The AI measurements were made for four of the blood samples. On average, the CFL thickness increased with increasing AI as shown in Figure 4.6. This trend was expected, as it was anticipated that higher AI measurements of static whole blood would correlate with higher aggregability of the flowing blood suspensions, and we hypothesis that RBC aggregation enhances the RBC axial migration, which would lead to a wider formation of the CFL at the walls. These results are in agreement with the theory reported in several studies [21,49], revealing that more aggregation results in larger CFL adjacent to the wall.

The difference in cell-free layer thickness among the samples could be due to their different plasma viscosities [88], and the variation of plasma protein concentration among the samples, which can also affect RBC aggregation. In future studies, synthetic plasma could be used instead

of autologous plasma, in order to help equalize the aggregability between samples. The results would help to interpret and clarify the alteration of the CFL.

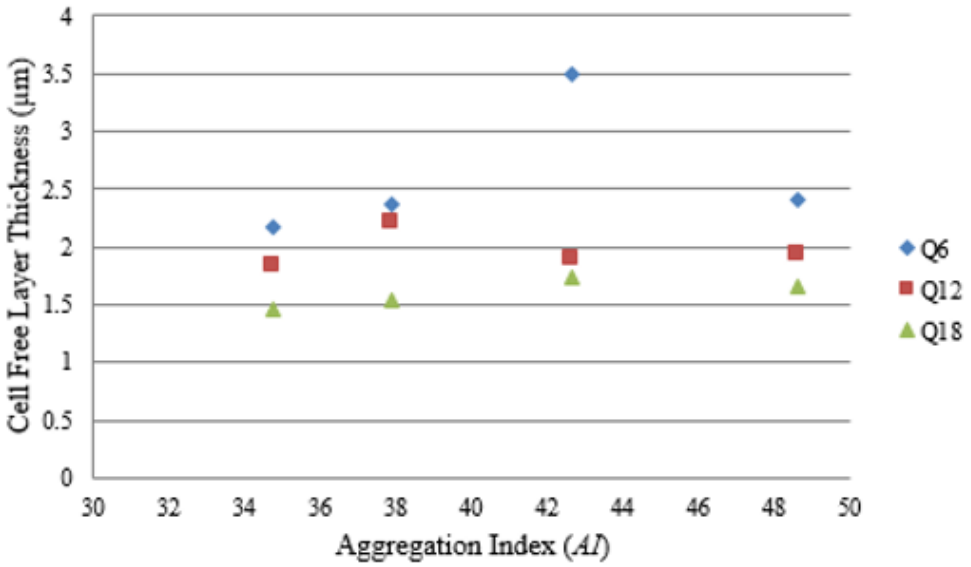

Figure 4.6: The CFL thickness as a function of the aggregation index (AI) for different blood samples, and three programmed flow rates *Q* (µl/hr) using the straight microchannel.

4.3 Conclusion

Using human blood suspended in native plasma at 10% H, the formation of a CFL was clearly identified from recorded images, and by using image-analysis techniques, the width of this layer was measured. The effects of flow rate and channel bifurcating geometry on the CFL thickness were investigated. The CFL thickness was significantly reduced with increasing the flow rate. The microchannel geometry did not impose significant influence on the CFL formation in the straight sections of the microchannels, while within the bifurcation, larger CFL thickness was formed at the outer wall of the bifurcation. The CFL thickness showed an increasing trend with increasing the aggregation index AI.

To better understand and clarify the relation between CFL formation and RBC aggregation, more investigation of RBC aggregation within rectangular microchannels is needed. The RBC aggregate size will be assessed at different flow rates and for different microchannel geometries using the same captured images used for the CFL investigation. This will be presented and discussed in the next chapter. The asymmetric formation of CFL at the bifurcation will be further discussed with respect to the complex field of shear. In order to do so, the velocity profile will be measured and will be presented and discussed in Chapter 6.

Chapter 5

Red Blood Cell Aggregate Size Measurements

This chapter presents the RBC aggregate size measurements for blood flowing under the same flow rates and microchannel geometries as used for the measurements of CFL thickness. The experimental procedure is concisely summarized here. The results determine the relationship between RBC aggregate size and CFL thickness.

5.1 Experimental Set-up and Procedure

Using the experimental set-up presented in the previous chapter (Figure 3.4), healthy human blood samples were collected from six different adult volunteers and visualized for the RBC aggregation investigation in rectangular cross-section microchannels. For each blood sample, the hematocrit and the aggregation index of the whole blood were measured using the microhematocrit centrifuge (CritSpin, Thermo Fisher Scientific Inc., China) and aggregometer (RheoScan-AnD 300; Rheomeditech, Seoul, Korea), respectively. All blood samples were cleaned and re-suspended in their native plasma at 10% H. The procedures for blood cleaning and preparation were described in detail in Section 3.2. Each RBC suspension was tested in the straight and bifurcating microchannels at three different programmed flow rates[2] by the pump: 6 µl/hr, 12 µl/hr, and 18 µl/hr, in order to study the effect of both flow rate and microchannel geometry on the RBC aggregate sizes. Blood was injected into the microchannel at the chosen flow rate using a syringe pump. The blood flow was recorded using a high-speed camera. A detailed description of the experimental set-up was presented in Section 3.3. The captured images were processed with a MATLAB program that detected and measured the RBC aggregate size. The image processing technique was described in depth in Section 3.4.2. Figure 5.1 shows high-speed camera images processed with MATLAB for 10% H blood suspension flowing at 6, 12, and 18 µl/hr. Each RBC aggregate was detected and colored based on its size. Aggregates of small sizes, less than 100 μm^2, are coloured in blue, aggregates ranging between 100 and 2,999 μm^2 are coloured in the increasing

[2] The "programmed flow rate" is to be distinguished from the actual flow rate, which is lower than the programed one, as a result of the system compliance. The actual flow rate is estimated in Chapter 6.

colour gradient according to the colour code listed in Table 3.1, while aggregates sizes of 3,000 μm^2 or larger are presented in red.

At the lowest flow rate 6 µl/hr, RBCs bridged together and formed large aggregates (Figure 5.1 (a)). In Figure 5.1 (b), where the flow rate was 12 µl/hr, RBCs formed smaller aggregates, and at the higher flow of 18 µl/hr, the RBCs had a lower chance to bridge together and form aggregates, and presented either as individual cells, or as very small aggregates comprised of several cells (Figure 5.1 (c)). The colour bar indicates the colours of aggregates based on their size range. The average RBC aggregate size for each geometry is then plotted versus the flow rate. For each geometry 10-15 tests were performed using 6 different blood samples (2-4 tests per sample).

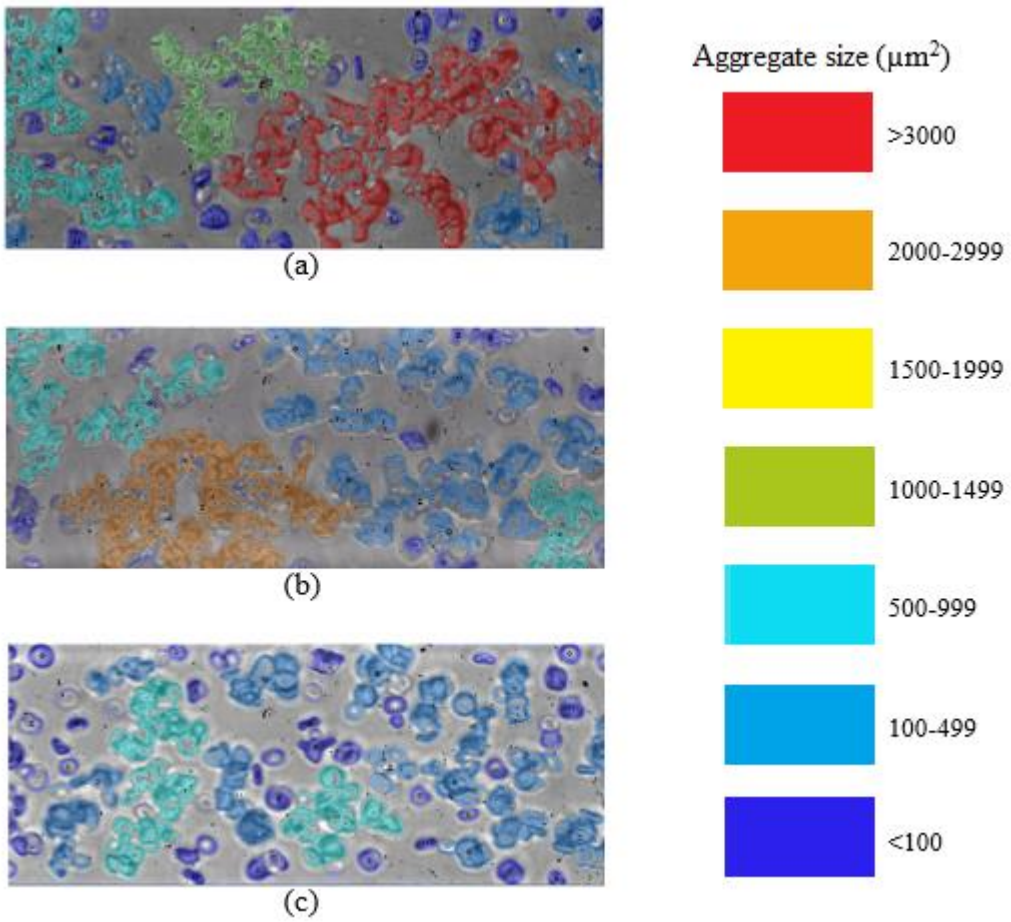

Figure 5.1: High speed camera images processed with MATLAB to detect the RBC aggregate size. Processed high speed camera images of 10% H RBCs suspension flowing at programmed flow rates (Q) of; (a) 6 µl/hr, (b) 12 µl/hr and (c) 18 µl/hr. The colour bar represents the colours used to detect different aggregates based on their sizes.

To find the average aggregate size for each flow rate and each microchannel geometry, 500 high-speed images were captured per recording. Ten images of each recording (every 50th image) were processed to assess the average aggregate size per image. The average aggregate sizes in these 10 images provides one measurement of the aggregate size per recording. The average aggregate size for one recording at the three different programmed flow rates; 6 µl/hr, 12 µl/hr, and 18 µl/hr is shown in Figure 5.2. For these recordings, the average aggregate size was 452 µm^2 at 6 µl/hr, 381 µm^2 at 12 µl/hr, and 204 µm^2 at 18 µl/hr.

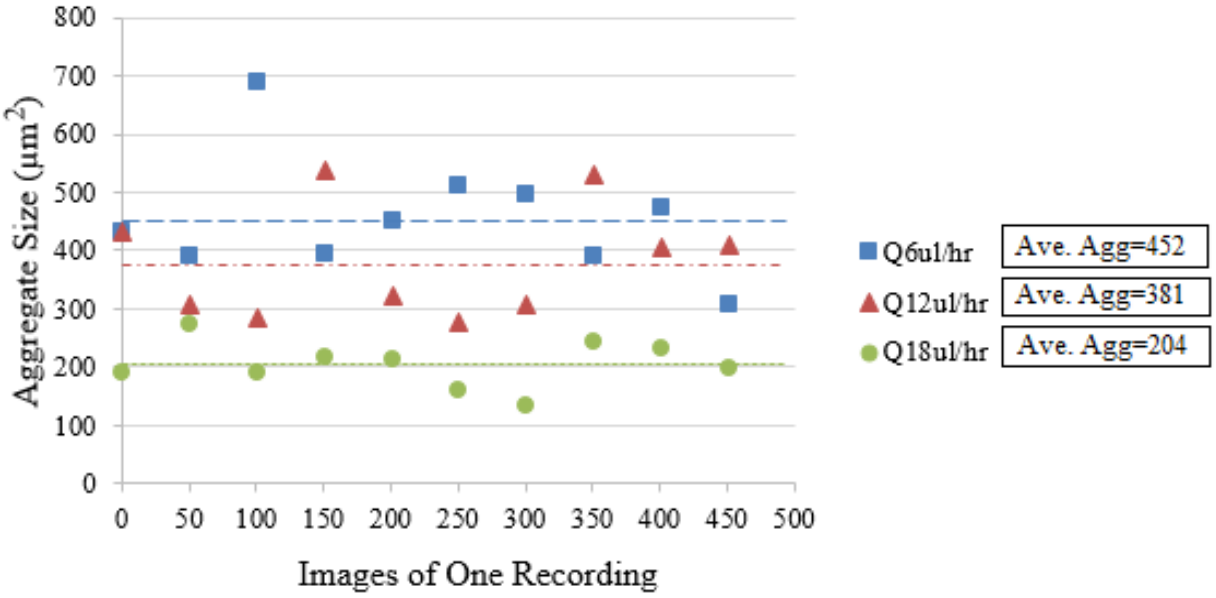

Figure 5.2: The average aggregate size (µm^2) for one recording in the straight microchannel (same blood sample), for programmed flow rates *Q;* 6 µl/hr, 12 µl/hr, and 18 µl/hr. The dashed lines indicate the averages of the 10 images for each flow rate.

5.2 Results and Discussion

5.2.1 Effect of Blood Flow Rate on RBC Aggregate Size

It is important to recognize that the plasma from different volunteers have different protein concentrations, and that variation in the protein concentration may affect RBC aggregation. Figure 5.3 illustrates the aggregate sizes averaged from 10-15 tests, from six different blood samples for the flows in the straight microchannels. The bars represents the maximum and the minimum sizes that were detected. At the lowest flow rate of 6 µl/hr, large RBC aggregate sizes were detected. The bars indicate that a wide range of aggregate sizes were found at this flow rate. This low flow rate allows RBCs to bridge together and form large aggregates. Increasing the blood flow rate to

12 µl/hr caused a reduction in aggregate size, and the bars indicate narrower range of aggregate sizes.

Comparing the aggregate sizes of 6 µl/hr and 12 µl/hr, the results show an average reduction in the aggregate size of 36% for the increasing flow rate. At the highest flow rate of 18 µl/hr, the sizes of aggregates became even smaller. Comparing the aggregate sizes of 12 µl/hr and 18 µl/hr, the results show an average reduction in the aggregate size of 16% with the increasing flow rate. It can be observed that the lower aggregation range is fairly consistent for all employed flow rates; i.e., there were very small aggregates or single cells found for even the lowest flow rates.

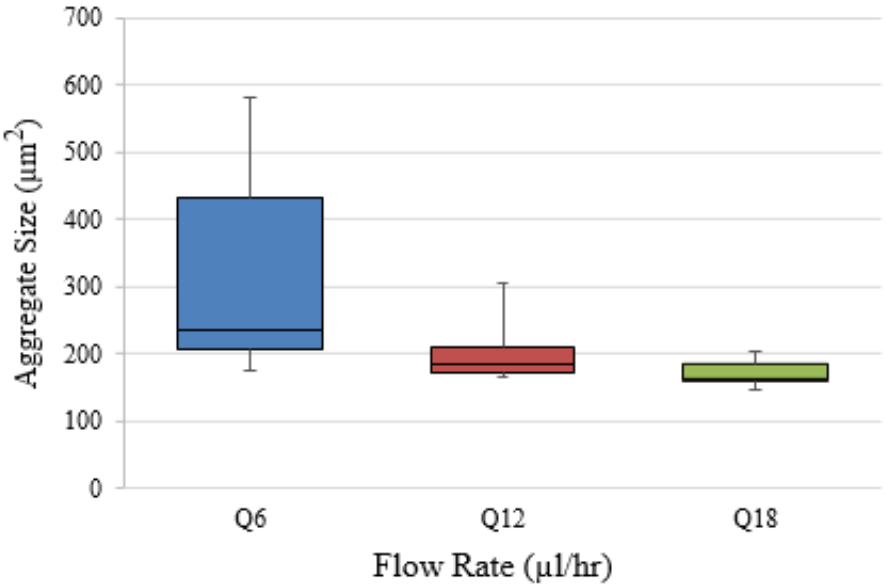

Figure 5.3: The RBC aggregate size (µm^2) as a function of the programmed flow rate *Q* (µL/hr) for the straight microchannels, for 6 different blood samples. The top and bottom whiskers represent the maximum and minimum aggregate sizes, respectively; the top and bottom sides of the box represent the first and third quartiles, respectively (i.e. the sizes for which 25% and 75% of the aggregates are less than or equal to); and the line inside the box represents the median of the aggregate sizes.

The distribution of the aggregate sizes for the three different programmed flow rates, considering all samples is shown in Figure 5.4. This figure illustrates that, at the lowest flow rate (6µL/hr) different aggregates were formed with 30% > 300 µm^2. Here, it is clearly shown that increasing the flow rate causes a reduction in the aggregate size. At programmed flow rates of 12 µL/hr, only 10% of aggregates exceeded 300 µm^2, and at the highest flow rate (18 µL/hr) only 2% exceeded 300 µm^2 and none exceeded 450 µm^2.

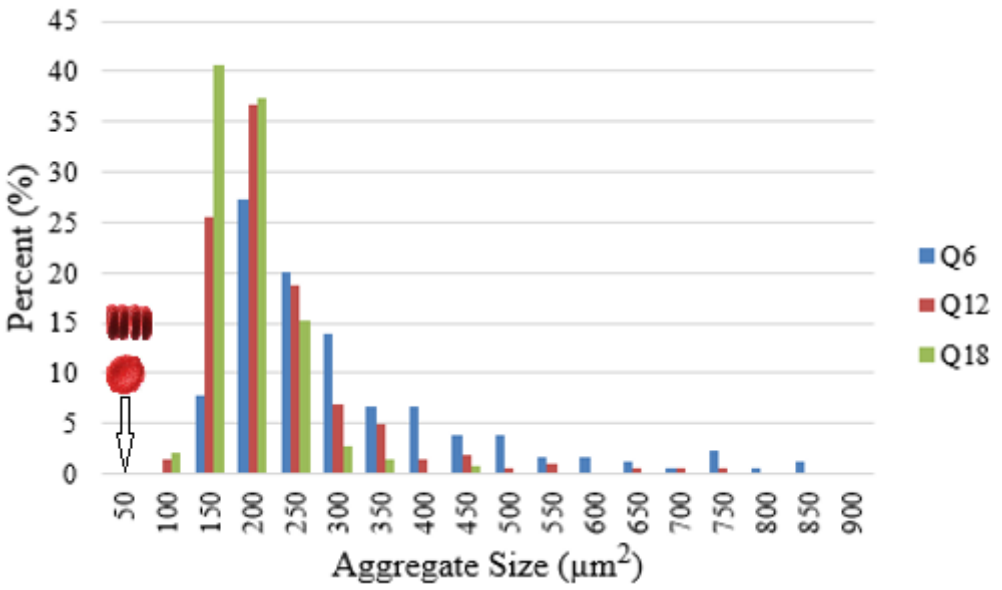

Figure 5.4: The average aggregate size distribution for 10% H human blood flowing at three different programmed flow rates *Q*= 6 µl/hr, 12 µl/hr, and 18 µl/hr, for 15 -25 tests using samples from 6 different donors, flowing into straight microchannels. The 50 µm^2 corresponds to either 1 typical RBC viewed by its planform area, or up to 4 RBCs aggregating together, viewed from their sides.

Figure 5.5 presents the results of the average aggregate size plotted versus the programmed flow rate by the pump for the three microchannel geometries (one straight microchannel, and two bifurcating microchannels with 35° and 75° bifurcating angles). For the bifurcating microchannels, the measurements were performed upstream of the bifurcation and immediately downstream of the bifurcation over a length of 200 µm (illustrated in Figure 5.5 (a)). The results were compared using a two-way ANOVA test.

The results reveal a significant reduction in aggregate size with increasing flow rate for all microchannel geometries. At 6 µl/hr, the average aggregate size for all geometries ranges from 190-336 µm^2 with a mean size of 263 µm^2. Increasing the flow rate to 12 µl/hr reduces aggregate sizes for all geometries to between 183-205 µm^2 with a mean size of 193 µm^2. At the maximum flow rate used in this study, 18 µl/hr, the average aggregate sizes for all geometries were between 156-177 µm^2 with a mean size of 167 µm^2.

It can be noted that the standard deviation bars are wider at the lower flow rates indicating the existence of both small and large aggregates, while at the higher flow rates the bars are smaller. At low flow conditions, the associated shear rate is also low, allowing RBCs to stack together and

form large aggregates. Increasing the flow results in an increase in the shear rate, which cause the aggregates to break up, thus reducing their sizes. These results agree with the findings of Mehri et al. (2014) which investigated the RBC aggregate sizes for different shear rates and for different RBC hematocrit [34].

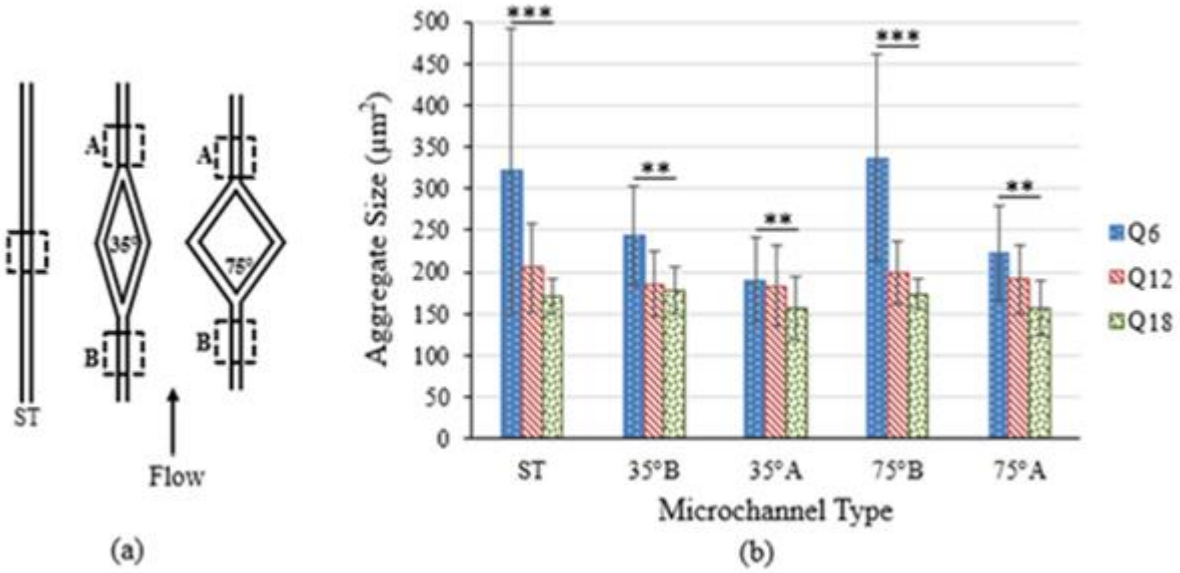

Figure 5.5: RBC aggregate size (μm^2) as a function of programmed flow rate *Q* (µl/hr) for the three different microchannel geometries. (a) The measurement positions are the straight microchannel midpoint, and before the bifurcation (B) and after the bifurcation (A) for the two bifurcating microchannels. (b)The aggregate size for three different microchannels, (ST) straight, 35º and 75º bifurcating microchannels, for 10-15 test of six different blood samples, (**) $P \leq 0.05$, (***) $P \leq 0.01$.

5.2.2 Effect of Microchannel Geometry on RBC Aggregate Size

The measurement locations for the aggregate sizes were the same as for the CFL thickness, described in Chapter 4: at the midpoint along the axis of the straight microchannel and both upstream and immediately downstream of the bifurcation in the two bifurcating channels. The average aggregate size measured at these locations in the three different microchannel geometries is shown in Figure 5.5. Results from the different geometries and at the same flow rate were compared using two-way ANOVA test. The statistical comparison between those different microchannels geometries did not detect any significant difference. These results indicate that the change of the bifurcating microchannel geometry has no significant influence on the aggregate sizes either upstream or downstream of a bifurcation, for constant flow rate in the physiological

range. When comparing the average aggregate size before and after the bifurcation, however, a reduction in the aggregate size after the bifurcation is observed, but, the difference was not significant. As was explained in Chapter 4, this reduction can be attributed to presence of the bifurcation (the flow rate in each branch was half of that upstream and downstream of the bifurcation), and also to the change in the hematocrit distribution within and between the branches. These changes influenced the aggregation within the bifurcation, resulting in smaller sized aggregates, which were carried downstream of the bifurcation.

5.2.3 Effect of Aggregation Index (AI) on RBC Aggregate Size

Investigating the influence of the AI on the RBC aggregate size helps to quantify the effect of individual variation in blood aggregability between samples from different donors. AI was measured for the fresh whole blood. Four different blood samples from different volunteers were used. The average aggregate size was plotted at the three programmed flow rates, as shown in Figure 5.6. The results show that the AI measurement of the whole blood has no influence on the aggregate size. This was unexpected, but one explanation is that the measured AI was influenced by the hematocrit of the whole blood sample, which varied from 40-45 % (systemic hematocrit) between subjects. Blood of high hematocrit has higher aggregation index [64].

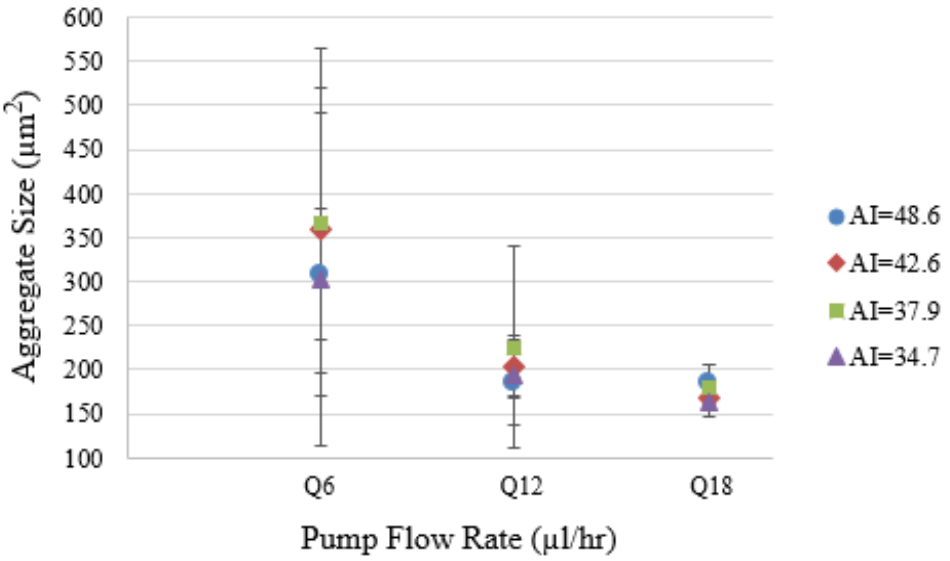

Figure 5.6: The RBC aggregate size as a function of the programmed pump flow rate *Q* (μl/hr) for 4 different blood samples with different aggregation index (AI).

This experimental work, however, was performed with 10% H blood, a typical hematocrit level found at the microscale (much lower than the systemic hematocrit). The measurement of the AI for the 10% H samples was not possible, however, because the low concentration RBCs let too much light passes through the sample, resulting in saturation of the light transmitted in the aggregometer, and erroneous readings.

5.2.4 Effect of RBC Aggregation on CFL Formation

It has been well established in the literature that RBC aggregation influences CFL formation, however, no physical explanation has been provided. Based on the droplet migration theory, we hypothesize that RBC aggregation enhances RBC migration toward the centerline of the vessel, leaving a wider CFL, or plasma layer void of cells.

In Chapter 4, the CFL thickness was measured for different flow rates and different geometries. In this chapter, the aggregate size was measured under the same conditions and geometries as for the CFL measurements. In Figure 5.7 the results of the CFL thickness and RBC aggregate size were plotted versus the three programmed pump flow rates. The regression line equation for CFL thickness versus flow rate is expressed as: y=-0.084x+2.39, with R^2=0.51, p_a= 0.0008 and p_b< 0.0001; the regression line equation for RBC aggregate size versus flow rate is expressed as: y=-12.45 x+381.88, with R^2=0.28, p_a= 0.0234 and p_b< 0.0001. p_a and p_b are the probability of the slope and intersect of the regression line, respectively.

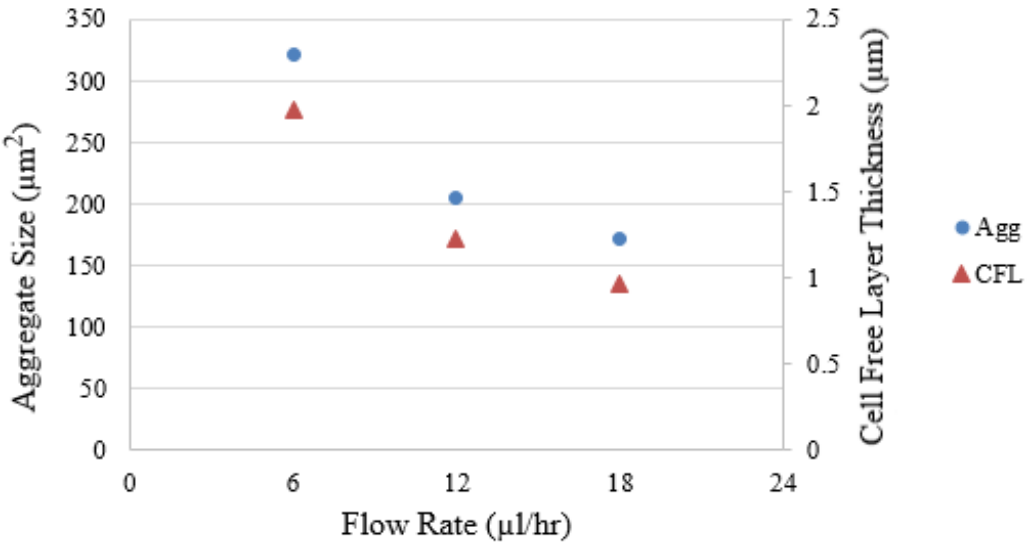

Figure 5.7: RBC aggregate size (µm^2) and CFL thickness (µm) as a function of the programmed flow rate Q (µl/hr), averaged for six different blood samples flowing in straight microchannels.

These results suggest a linear correlation for both CFL thickness and RBC aggregate size with the flow rate. It also confirms the significant effect of flow rate on both measurements. It was noticed that the reduction trends of both RBC aggregate size and the CFL thickness with the flow increase are nearly parallel, revealing a strong correlation between the aggregate size and the thickness of the CFL.

The results in Figure 5.7 can be explained based on the mechanism of particle migration which was discussed in Chapter 2, Section 2.6. At lower flow rate the corresponding shear rate is also low and therefore the neighbouring RBCs are able to form aggregates of large sizes. This increase in the size enhances the lift force that acts on the cells and drives them away from the wall towards the centerline, with the migration velocity (u_{mig}) away from the wall proportional to the 4th power of the particle radius (of either individual RBCs or aggregates) and proportional to the squared magnitude of shear rate (i.e. $u_{mig} \propto \gamma^2 * r^4 / y^2$). Thus, an increase in the aggregate sizes at this lower flow rate strongly affects the migration and results in a larger CFL thickness. Considering the cell-cell interaction or shear-induced diffusion, which drives the cells away from the central high concentration region, at this low shear rate the diffusion D is relatively low, since $D \propto \gamma * r^2$. (i.e. the forces due to diffusion are less sensitive to increases in particle size than the inward migrating forces are).

Increasing the flow rate increases the shear rate, which lowers the chance for neighbouring RBCs to form large aggregates. Furthermore, the increased shear breaks up larger aggregates to smaller ones. This reduction in particle size reduced the migration velocity towards the centerline allowing the RBCs to spread over a wider range in the microchannel, and therefore reducing the thickness of the CFL.

These quantitative results confirm the theory in the literature suggesting that RBC aggregation enhances CFL formation. They also show a good agreement with *in vivo* experiments of Ong et al. 2010 [5] when comparing aggregating and non-aggregating blood samples, as their results showed that CFL formation was enhanced by a combination of flow reduction and RBC aggregation.

5.3 Conclusion

Experiments were performed on 10% H blood samples flowing into three microchannel geometries at three flow rates. Flowing blood was imaged with a high-speed camera and using a

custom image processing technique, described in Section 3.4.2. The RBC aggregates size was measured for each case. Based on the results of this work, blood flow rate was the key factor that influenced RBC aggregation. Increasing the flow rate caused a significant reduction in the RBC aggregate size. It was hypothesized that the RBC aggregation may be affected by the vessel or microchannel morphology; the results, however, showed that the microchannel geometry has no significant influence on the RBC aggregate size, at the employed range of flow rates. Comparing the RBC aggregate sizes to the measured aggregation indices (AI) of the whole blood samples showed no manifest relation. This was attributed to the difference in the original hematocrit and plasma properties of whole blood samples, which were collected from different adult volunteers.

The RBC aggregation results in this chapter were used to interpret CFL formation under the same flow conditions and same microchannel geometries. The quantitative measurements of aggregate sizes and CFL thickness near the microchannel wall presented a clear relationship suggesting that larger aggregate size enhanced RBC migration velocity toward the centreline and hence resulted in larger CFL thickness.

Based on the well-known fact that the shear rate plays an important role on the aggregation and disaggregation of RBCs, the results of CFL thickness and RBC aggregate size demand quantitative measurements of the actual flow rate and the associated shear rate. In the next chapter, the actual flow rate and shear rate will be measured from the velocity profiles and related to aggregate size and corresponding CFL thickness.

Chapter 6

Velocity Profile and Wall Shear Rate Measurements Using Micro-PIV

This chapter presents the experimental flow velocity profile measurements for DI water and 10% H human blood using the same flow rates and two microchannel geometries as employed for the measurements of CFL thickness and RBC aggregate size. The measurement of the flow velocity profile is essential for the estimation of important hemodynamic parameters such as flow rate, wall shear rate, and maximum velocity. The experimental procedure is briefly summarized here. The shear rate is the main factor influencing RBC aggregation; it is also hypothesized to influence RBC migration away from the wall, which consequently leads to alteration of the CFL at the wall. The shear rate measurements are discussed with respect to the results for CFL thickness and RBC aggregate size from the previous chapters.

6.1 Experimental Set-up and Procedure

To account for the variability in non-Newtonian behaviour of different blood samples, it is preferred to obtain a well-known Newtonian fluid velocity profile as a reference to ensure accurate measurements. For this, we used DI water as a Newtonian reference fluid.

The velocity profile measurements were performed for DI water and 10% H human blood each flowing in a PDMS straight microchannel and a bifurcating microchannel with 35° bifurcating angle (Figure 3.1) at three different programmed flow rates. For the bifurcating microchannel, the flow was recorded at: 1) the parent microchannel before the bifurcation (B), 2) within the bifurcation (Bif) and 3) after the bifurcation (A).

Velocity profile measurements were performed using the μPIV set-up illustrated in Figure 3.4. Human blood was cleaned and re-suspended in its native plasma at 10% H. The procedures for blood cleaning and preparation were described in detail in Section 3.2. In this experimental work, the working fluid, either DI water or human blood, was seeded with the fluorescent particles and injected into the rectangular PDMS microchannels (with an aspect ratio h/w~0.34) via a micro syringe pump (Nexus3000, Chemyx Inc., USA), at programmed flow rates of 6 μL/hr, 12 μL/hr, or 18 μL/hr. By programming the *x*-*y*-*z* stage, the velocity measurement was performed in different planes across the microchannel depth. This step ensured performing the measurement at the center-plane of the microchannel. The center-plane of the microchannel is defined as the location

where the velocity is maximum [89]. At each discrete level, a set of 100 image pairs of the flow were acquired using the CCD camera. Each set of images was processed via cross-correlation to obtain velocity vectors, which were averaged to obtain the average velocity profile [62,75]. The image processing was explained in depth in Section 3.4.3. Figure 6.1 depicts an experimental three-dimensional velocity profile (constructed from 2D velocity profile measurements at different planes across the channel depth) for DI water flowing at 18 µl/hr into the straight PDMS microchannel of 100 µm by 34 µm.

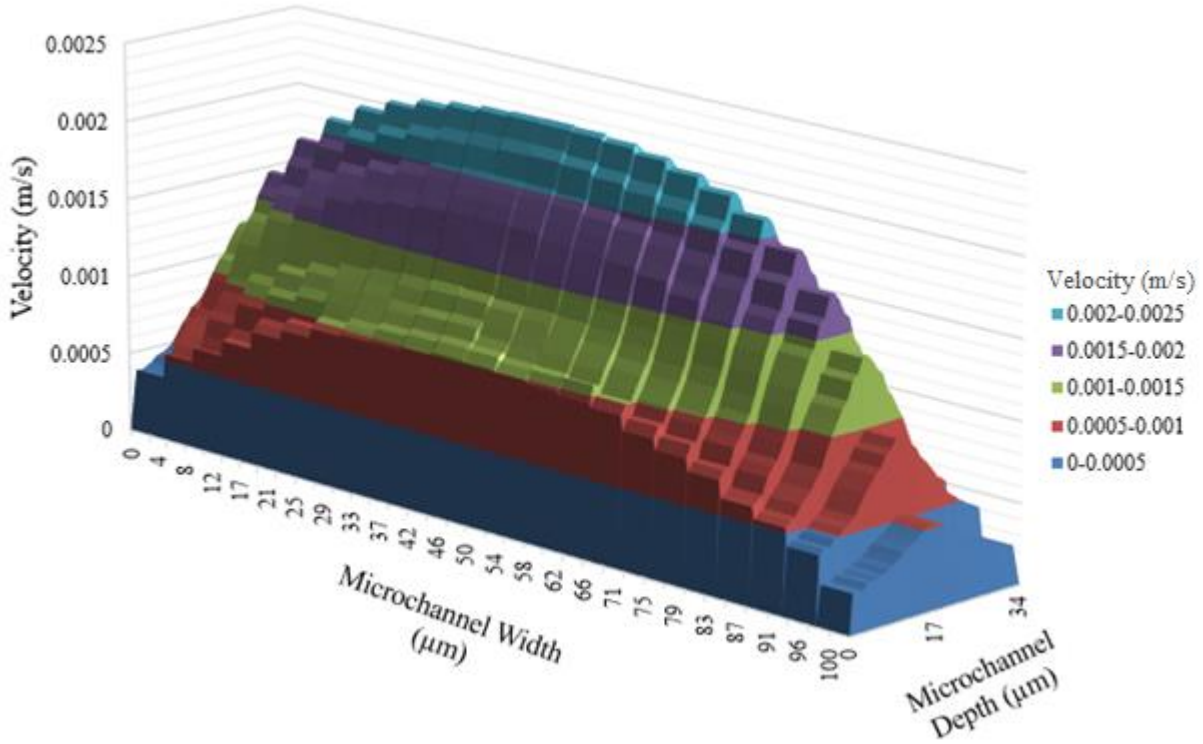

Figure 6.1: 3D velocity profile, constructed from 2D velocity profiles measured across the channel depth, for DI water flowing at 12 µl/hr into a straight PDMS microchannel of 100 µm by 34 µm.

Using the center-plane (2D) experimental velocity profile, the actual flow rate (Q_{calc}), the maximum velocity at the centerline (u_{max}) and the shear rate at the walls (γ_w) were determined using Equations 3.10 and 3.13. For a detailed explanation of the flow rate calculation, refer to Section 3.4.3.

6.2 Results and Discussion

The calculated flow rate was lower than the programmed flow rate in both cases with DI water and 10% H blood, as shown in Figure 6.2. This discrepancy is expected due to the system compliance. Also, the flexible nature of the PDMS may results in microchannel deformation under flow [35,90]. Hardy et al. 2008 reported pressure drops to be up to 35% less than the pressure drop when using a rigid-walled channel [90]. Similarly, the results of Pitts and Fenech, 2013 showed flow decreases of approximately 40% less than the programmed flow rates [35].

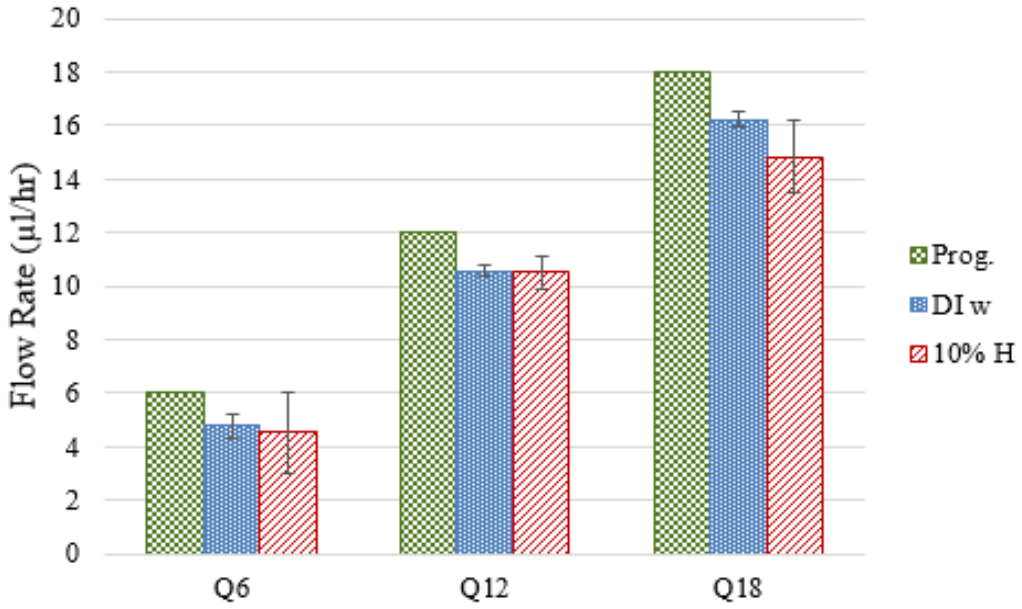

Figure 6.2: The programmed flow rates of the syringe pump (Q_{prog}) and actual calculated flow rates (Q_{calc}) for DI water and 10% H blood flowing into 34 µm by 100 µm straight PDMS microchannels. The results are the average of four DI water experiments and five 10% H blood experiments.

In this experimental work, rigid tubing was used in order to reduce compliance. The reduction in the flow rate was about 14% for DI water and about 18% for 10% H blood. In other words, the measured flow rates were 86% and 82% of the programmed pump flow rate for DI water and 10% H blood respectively. Another factor that could affect the results is the choice of the center-plane velocity profile. If this center-plane velocity profile was not actually at the center, deviation of every one micron (across the channel depth) can produce up to 5% reduction in calculated flow rate. The discretization step for the measurements was 1 µm for the DI water experiments and 2-3 µm for the 10% H blood experiments. This difference in the choice of the discretization step could have contributed to the larger standard deviation (SD) found for the blood measurements.

6.2.1 Theoretical and Experimental Velocity Profiles in Straight Microchannels

The programmed pump flow rates of 6 µl/hr, 12 µl/hr, and 18 µl/hr give theoretical maximum velocities of 0.916 mm/s, 1.83 mm/s, and 2.75 mm/s, respectively. The calculated flow rates (Q_{calc}) were considered as the actual flow rates, which were lower than the programmed flow rate by the syringe pump for both fluids (DI water and 10% H blood).

The center-plane theoretical velocity profiles for Newtonian fluid and the center-plane experimental velocity profiles for the DI water and 10% H blood, flowing into a straight PDMS microchannel at the three flow rates, are shown in Figure 6.3 and 6.4 respectively. The bars represent the standard deviation. The theoretical profiles were produced using Eq. 3.6 and the calculated value of the flow rates (Q_{calc}). In both figures (6.3 and 6.4), the experimental profiles are in good agreement with the theoretical profiles of Newtonian fluid, confirming that the calculated flow rates are accurate.

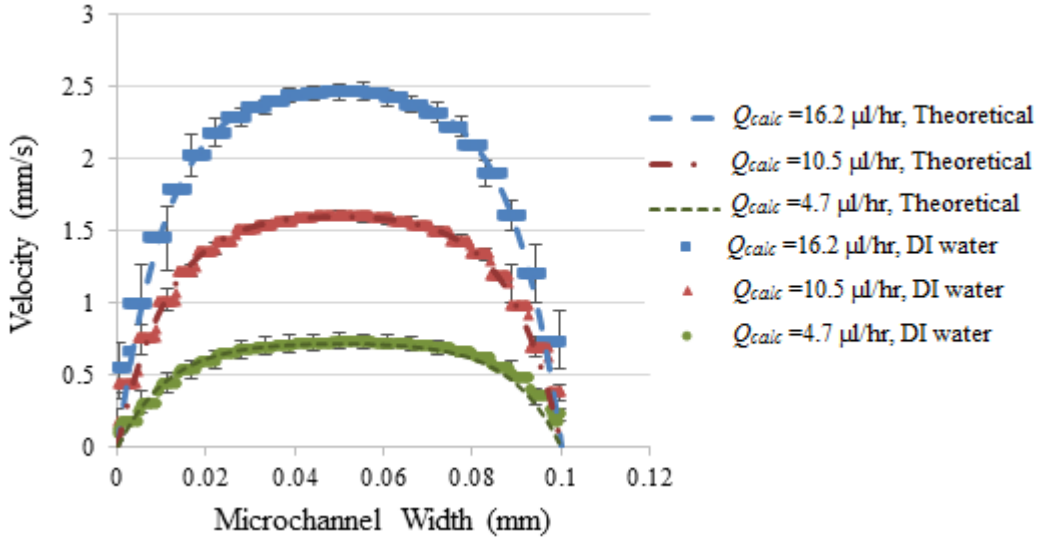

Figure 6.3: Center-plane theoretical velocity profiles (for Newtonian fluid) and experimental velocity profiles of DI water flowing into straight PDMS rectangular microchannels (34 µm x 100 µm), at calculated flow rates Q_{calc} = 16.2 µl/hr, 10.5 µl/hr, and 4.7 µl/hr. These results are the average of four experiments each.

When using DI water (Figure 6.3), the standard deviation of the velocity measurements was smaller than the standard deviation when using 10% H blood (Figure 6.4). This could be due to the difference of the florescent particle density and light intensity between the two fluids. DI water is Newtonian and the particles are distributed evenly, whereas the 10% H blood is non-Newtonian and the RBCs (which were larger than the fluorescent particles) affect the particles' distribution

and hence their light intensity, as was shown previously in Figure 3.10. Also, the presence of RBC aggregation increases the variability in the local velocity measurements between different blood samples [89].

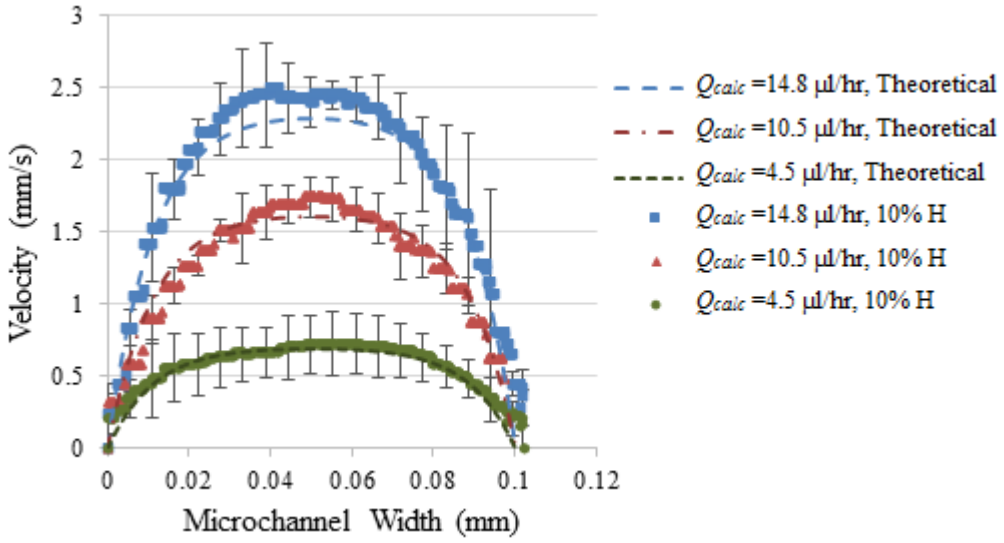

Figure 6.4: Theoretical velocity profiles (for Newtonian fluid) and experimental velocity profiles of 10% H blood flowing into straight PDMS rectangular microchannels (34 µm x 100 µm), at calculated flow rates Q_{calc} = 14.8 µl/hr, 10.5 µl/hr and 4.5 µl/hr. These results are the average of five experiments each done with different blood samples.

The radial variation of the shear rate (γ) was calculated by differentiating the velocity distribution with respect to the microchannel width, using Eq. 3.13. The theoretical and experimental shear rate profiles for DI water and 10% H blood are shown in Figures 6.5 and 6.6, respectively, for the three calculated flow rates Q_{calc} (µl/hr). The experimental shear rate profile for DI water was very close to the Newtonian theoretical profile (Figure 6.5). For the 10% H blood, at distances close to the wall (0 ~5 µm) the experimental shear rate profile was lower than the Newtonian theoretical profile. This was attributed to the presence of a two-phase flow: i.e. the presence of the CFL close to the wall and the RBC core in the centeral region. The velocity gradient within the CFL was much less than in the RBC core, causing the shear rate to be less there. The shear rate measurements in Figures 6.5 and 6.6 illustrate the well-known fact that the shear rate decreases toward the center of the microchannel. At the centered region, RBC aggregation is promoted due to the lower shear there, compared to that near the wall.

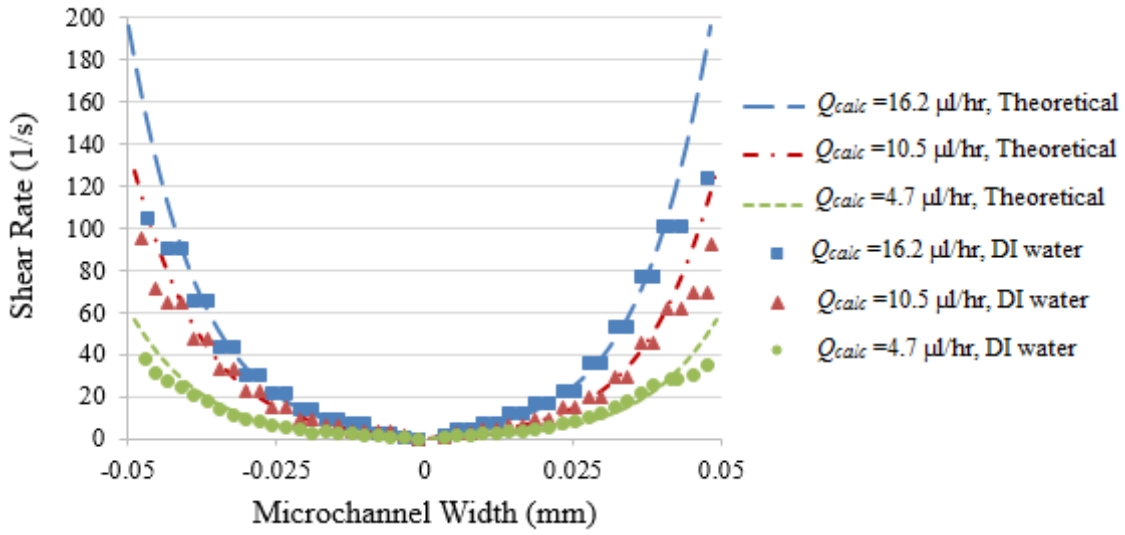

Figure 6.5: Theoretical shear rate distribution (for Newtonian fluid) and experimental shear rate distribution for DI water flowing into straight PDMS microchannels (100 µm by 34 µm), at calculated flow rates Q_{calc} = 16.2 µl/hr, 10.5 µl/hr, and 4.7 µl/hr. The shear rate results were averaged from four experiments each.

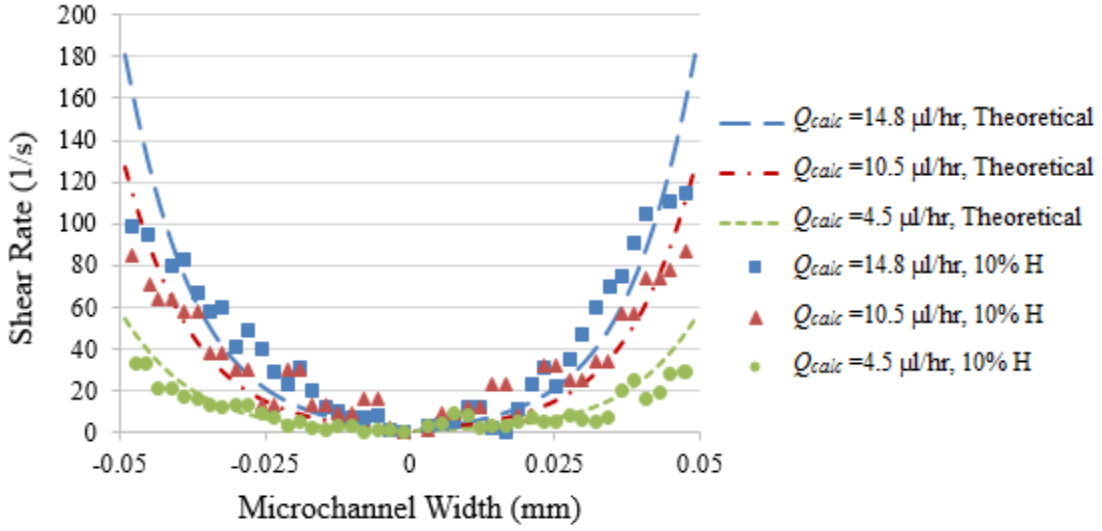

Figure 6.6: Theoretical shear rate profiles (for Newtonian fluid) and experimental shear rate profiles for 10% H blood. Shear rate distribution for 10% H blood flowing into straight PDMS microchannels (100 µm by 34 µm), at calculated flow rates Q_{calc} = 14.8 µl/hr, 10.5 µl/hr and 4.5 µl/hr. The shear rate results were averaged from five experiments each.

The velocity profile was characterized with both the shape factor *k* and the skewness *S*. These two terms were explained in Section 3.4.3. The shape factor of the theoretical velocity profile for the used microchannel of cross-section 34 µm x 100 µm was 4.0, while the skewness was zero.

The characterization of the experimental velocity profiles for DI water and 10% H blood is presented in Table 6.1, which lists the values of calculated flow rate (Q_{calc}), the maximum velocity (u_{max}), the shear rate at the wall (γ_w), shape factor (k) and skewness (S) at the programmed flow rates Q_{prog}= 6 µl/hr, 12 µl/hr and 18 µl/hr. Standard deviations are also listed for u_{max}, γ_w, k and S.

Table 6.1: Velocity profile results for both DI water and 10% H blood in straight microchannels, where Q_{prog} is the programmed flow rate by the syringe pump, Q_{calc} is the calculated flow rate, u_{max} is the maximum velocity and γ_w is the shear rate at the wall, k is the shape factor and S is the skewness. SD represents the standard deviation for u_{max}, γ_w, k and S, respectively. The results represent an average of four measurements using DI water, and five measurements, using different blood samples.

Fluid	Q_{prog} µl/hr	Q_{cal} µl/hr	u_{max} mm/s	SD	γ_w s^{-1}	SD	k	SD	S %	SD
DI	6	4.7	0.73	0.058	30.90	2.15	4.05	0.15	1.49	2.1
DI	12	10.5	1.60	0.031	70.36	2.60	4.17	0.16	0	0
DI	18	16.2	2.46	0.049	102.9	3.90	4.12	0.22	2.21	1.5
10% H	6	4.5	0.73	0.08	26.84	13.85	3.72	0.55	2.9	2.26
10% H	12	10.5	1.73	0.16	56.71	16.60	2.89	1.06	1.24	1.7
10% H	18	14.8	2.5	0.23	90.24	50.33	3.18	1.17	1.59	1.92

It is clearly shown, by the value of $k > 2$, that both fluids produce blunt profiles, whereas the parabolic profile has $k = 2.0$. The k value for DI water velocity profiles is about 4, very close to theoretical, for the range of used flow rates, which verify the accuracy of the measurements, while the k value for 10% H blood is lower than theoretical (between 2.9 and 3.7), indicating that the profile is less blunt than for water. The measurements using 10% H blood resulted in higher standard deviation than the measurements made with DI water. The non-homogeneous nature of the blood, as it consists of suspended cells, contributes to this deviation. This non-homogeneity is increased by the tendency of the RBCs to migrate away from the wall and form aggregates of different sizes. RBC aggregation reaches a maximum at lower flow rates. RBC migration causes the increased sharpness of the velocity profile at the sides, while RBC aggregation blunts (or flattens) the profile at the center. RBC migration and aggregation also influence the distribution of the fluorescent particles and hence the velocity profile measurements. The lowest flow rate (4.5

µl/hr) produces a greater *k* value (indicating a blunter profile, i.e. a larger flattened region at the center), which confirms the effect of aggregation on the shape factor. There is no statistical difference between all the measurements in Table 6.1 for both fluids (DI water and 10% H Blood). Figure 6.7 illustrates the experimental velocity profiles of 10% H blood, averaged from five experiments, and the fitted profiles to calculate *k* value by minimizing the difference between each two curves. This figure shows good agreement between the experimental and fitted profiles.

The skewness of the experimental velocity profiles (listed in Table 1) for both fluids using the straight microchannel was less than 3%, which can be considered close to zero (the theoretical value).

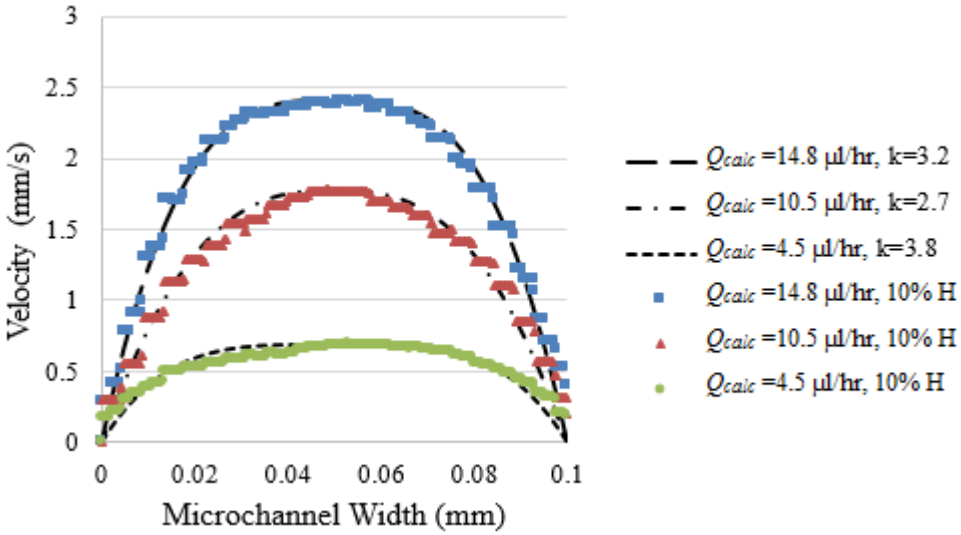

Figure 6.7: The experimental velocity profiles of 10% H blood (the average of five experiments) and the fitted profiles using the *k* value, for three calculated flow rates Q_{calc} = 4.5 µl/hr, 10.5 µl/hr, and 14.8 µl/hr.

6.2.2 Experimental Velocity Profile of 10% H Blood in Bifurcating Microchannels

In this experimental work, in addition to the measurements made in a straight microchannel, the velocity profile was measured within a bifurcating microchannel. The velocity profile measurements were performed upstream and downstream of the bifurcation in a microchannel of 35° bifurcating angle, as well as within the daughter branches. Figure 6.8 illustrates the velocity profile measurement locations within the bifurcating PDMS microchannel with 34 µm by 100 µm cross-section. Figure 6.9 depicts the velocity profiles at the three locations: before the bifurcation (B), within the daughter branch (Bif), and after the bifurcation (A) at the programmed flow rate of 12µl/hr.

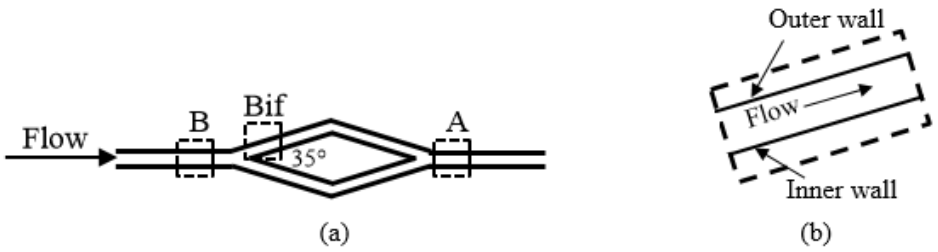

Figure 6.8: The velocity profile measurement locations using bifurcating microchannel. (a) The three measurement locations - before the bifurcation (B), within the daughter branch (Bif), and after the bifurcation (A) - of a bifurcating PDMS microchannel (34 µm by 100 µm cross-section); (b) the inner and outer wall locations in the bifurcation.

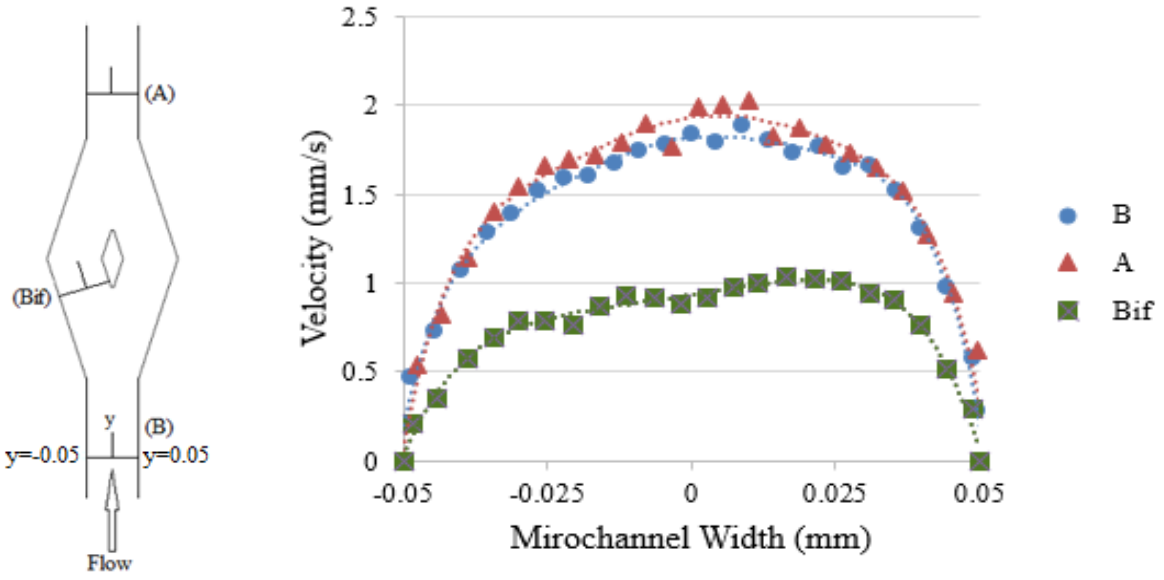

Figure 6.9: The velocity profiles of 10% H blood flowing into microchannel of 35° bifurcation at 12µl/hr pump flow rate, and at three locations: before the bifurcation (B), after the bifurcation (A) and within the daughter branch (Bif).

The velocity profile in the parent channel was nearly symmetric, but as the flow moved into the daughter branch, the location of maximum velocity moved toward the bifurcation apex [91]. Due to the centrifugal force caused by the directional change of the flow, the velocity profile was dramatically skewed toward the inner wall of the daughter branch [92], however, the velocity profile recovered its shape shortly after the bifurcation (at location A).

The velocity profile results for 10% H blood flowing into the 35° bifurcating microchannels for the three measurement locations are summarized in Table 6.2. This table includes values of the

maximum velocity (u_{max}), the shear rate at the wall (γ_w), shape factor (k) and skewness (S) at the programmed flow rates of 6 µl/hr, 12 µl/hr and 18 µl/hr. Standard deviations are also listed for u_{max} , γ_w, k and S. There was no significant difference found between the measurements made before the bifurcation (B) and those after the bifurcation (A). The results of the locations before the bifurcation (B) and after the bifurcation (A) were similar to those the straight channel, which confirm the accuracy of the measurements. These results also confirm that the bifurcation has no significant influence on the flow in the straight parts upstream or downstream of it.

Table 6.2: The velocity profile results for 10% H blood flowing into the 35° bifurcating microchannels, where Q_{prog} is the programmed flow rate by the syringe pump, u_{max} is the maximum velocity, γ_w is the shear rate at the wall, k is the shape factor and S is the skewness. The results represent the average of five experiment using different blood samples.

Fluid	Q_{prog} µl/hr	u_{max} mm/s	SD	γ_w s^{-1}	SD	k	SD	S %	SD
B	6	0.73	0.17	30.93	10.99	4.00	1.19	5.4	1.4
	12	1.58	0.17	59.43	7.66	3.87	0.39	6.2	1.9
	18	2.6	0.34	91.16	54.4	4.03	1.44	3.1	2.3
A	6	0.66	0.17	24.86	15.46	3.06	0.31	4.9	3.6
	12	1.77	0.18	70.0	13.13	4.01	0.67	5.6	3.5
	18	2.04	1.9	83.96	40.45	4.3	0.99	3.6	2.9
Bif	3	0.65	0.10	20.0	3.52	3.67	0.60	7.4	4.9
	6	1.12	0.08	36.03	6.66	3.33	0.62	14.6	5.4
	9	1.54	0.16	49.97	19.1	4.61	1.10	16.0	4.6

The shape factor of the velocity profile did not show any significant change between the three locations and was similar to the straight microchannel results. In the bifurcation, the flow and average velocity were reduced to roughly half of that in the mother microchannel; this is because the branches have the same cross-section dimensions as the mother channel, and the flow from the latter divides into the two branches. It has been previously reported that the divided flow results in uneven hematocrit between the two branches [1].

Figure 6.10 illustrates the velocity profile skewness results for the bifurcating microchannel, at the three locations (B, Bif and A) and for the three flow rates. For all flow rates, the average skewness of velocity profiles before and after the bifurcation was less than 5 %. This figure shows that within the bifurcation the velocity profile is skewed, the skewness towards the inner wall increases from about 7% - 16% with the flow rate increase. This skewness can be explained as follows: RBCs having the highest velocity moves from the center of the parent channel towards the bifurcation apex and flow close to the inner wall of the bifurcation [91]. The change in the flow direction in the bifurcation enforced RBCs to flow away from the outer wall and tend to collide with the inner wall [54]; this engenders large CFL at the outer wall. The formation of a CFL at the outer wall of the bifurcation (demonstrated in Chapter 4) and the asymmetric distribution of the hematocrit in the bifurcation may also have contributed to the skewed velocity profile. [51]. The RBC aggregation and non-uniform viscosity can also result in skewing the velocity profile [51].

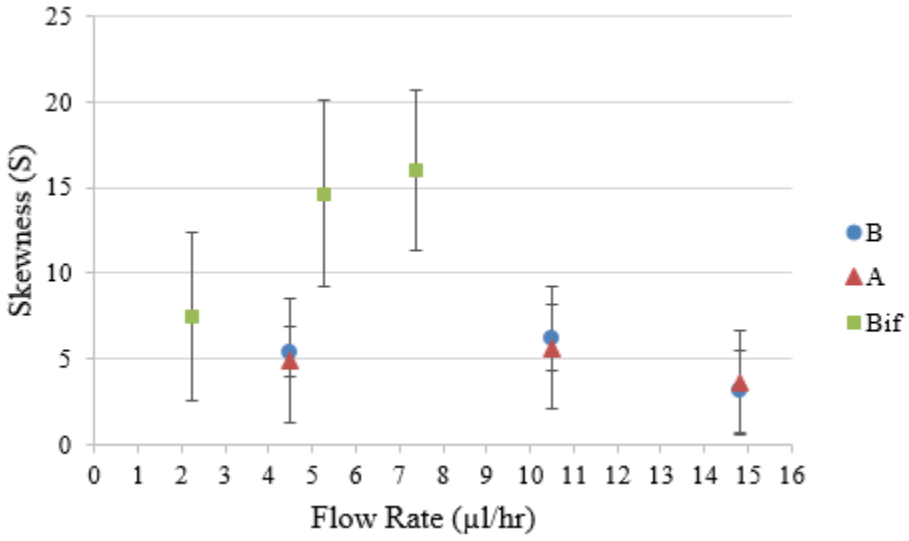

Figure 6.10: The velocity profiles skewness of 10% H blood flow in the bifurcating microchannel of 35° and 34 µm by 100 µm cross-section, at three locations; before the bifurcation (B), after the bifurcation (A) and within the daughter branch (Bif). The calculated flow rates, for mother microchannel Q_{calc} = 4.5 µl/hr, 10.5 µl/hr, and 14.8 µl/hr.

It has been previously reported that the velocity profile downstream of a bifurcation returns to uniformity (i.e. zero skewness) after several diameters and that the hematocrit redistribution takes about 10 diameters to recover [51]. The bifurcating branches of the channel used in this study, however, were not sufficiently long to measure this recovery.

The measurements of the wall shear rate (taken as the average from both sides) at the three locations (B, A and Bif), for the three calculated flow rates are shown in Figure 6.11. As expected, it is clearly shown that increasing the flow rate results in higher shear rates at the wall at all measurement locations. At the bifurcation, the shear rate was about half of the parent branch shear and it retrieved its level downstream of the bifurcation. Comparing before and after the bifurcation, no difference was detected, since the wall shear rate measurement was performed close to the wall where the CFL region exists. This finding is correlated to the results of Chapter four, where there was no significant difference found in the CFL formation between the B and A locations.

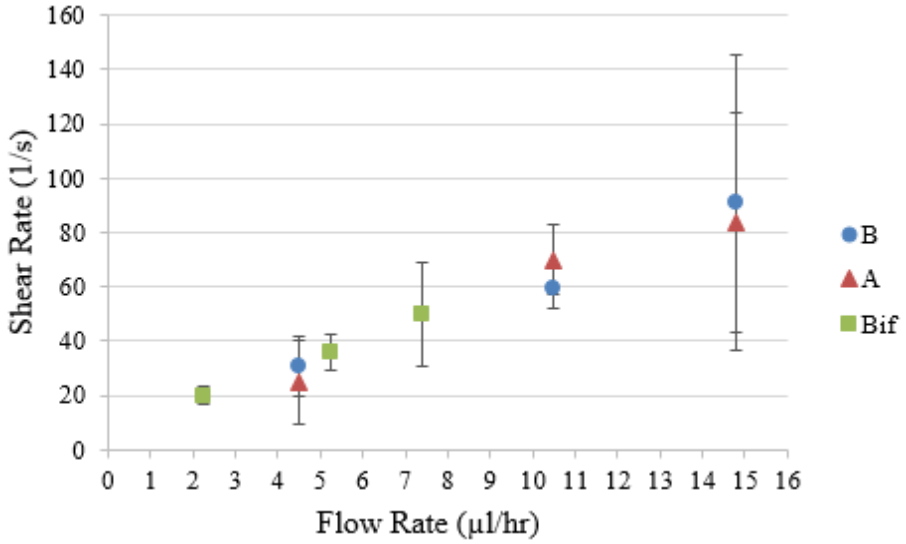

Figure 6.11: The wall shear rate (the average of both sides) vs. actual flow rate Q_{calc}. in a 35° bifurcating microchannel (34 µm x 100 µm cross-section), at three locations: before the bifurcation (B), after the bifurcation (A) and within the daughter branch (Bif). The actual flow rates in the mother channel were Q_{calc} = 4.5 µl/hr, 10.5 µl/hr, and 14.8 µl/hr.

6.2.3 The Influence of Wall Shear Rate on CFL Thickness and RBC Aggregation Size

Using the blood velocity profile measurements, the results of the shear rate at the wall were related to the CFL thickness measurement and RBC aggregate size performed in this experimental study (in Chapters four and five). Figure 6.12 illustrates the average CFL thickness as a function of the measured wall shear rate, and Figure 6.13 illustrates the average RBC aggregate size as a function of the measured wall shear rate for different blood samples. Figure 6.12 shows a reduction of the CFL thickness as the shear rate increases, this trend was expected and can be explained using Figure 6.13, where it shows that low shear rates enabled neighbouring RBCs to form aggregates of

larger size, this size is reduces at higher shear rate. Based on the theory of the droplet migration presented by Hudson (2003) [43], this increase in the aggregate size enhances the RBCs migration away from the wall towards the centerline and engenders a larger CFL adjacent to the microchannel walls. The mechanism of cell migration was discussed in Chapter 2, Section 2.6. The migration velocity (u_{mig}) away from the wall towards the centerline is proportional to the 4th power of the particle radius (of either individual RBCs or aggregates) and proportional to the squared magnitude of shear rate (i.e. $u_{mig} \propto \gamma^2 * r^4 / y^2$), where y is the distance between the wall and the center of cells. Thus, the increase in the size of RBC aggregates at this lower shear rate enhanced the migration and resulted in a larger CFL thickness. In contrast, the cell-cell interaction or shear-induced diffusion causes the cells to flow from the high concentration region at the center toward the wall, at the low shear rate level, the diffusion D is relatively low, since $D \propto \gamma * r^2$. (i.e. the forces due to diffusion are less sensitive to increases in aggregate size than the inward migrating forces are).

Increasing the shear rate, associated with the flow rate increase, prevented neighbouring RBCs to form large aggregates. In addition, the increased shear broke up larger aggregates to smaller ones. This reduction in RBC aggregate size at increased levels of shear rate reduced the migration velocity towards the centerline and hence diminished the CFL thickness.

At high levels of shear rates, however, the shear rate is the dominant factor governing the RBC migration — the effects of RBC aggregation are negligible (RBC aggregation occurs only at low shear rate levels [21]). Therefore, increasing the shear rate leads to increased RBC migration velocity ($u_{mig} \propto \gamma^2 * r^4 / y^2$), thus enhancing the CFL formation.

The effect of the wall shear rate on the RBC aggregate size distribution is shown in Figure 6.14. The results of the aggregate size distribution were averaged from 35-45 tests using six different blood samples. This figure shows that at the lowest wall shear rate (approximately 29 s^{-1}) larger aggregates were formed with 32% being larger than 300 μm^2. When the wall shear rate was increased to approximately 58 s^{-1}, this number fell to only 9%, and at the highest wall shear rate (approximately 91 s^{-1}), only 2.5% of the aggregates were larger than 300 μm^2.

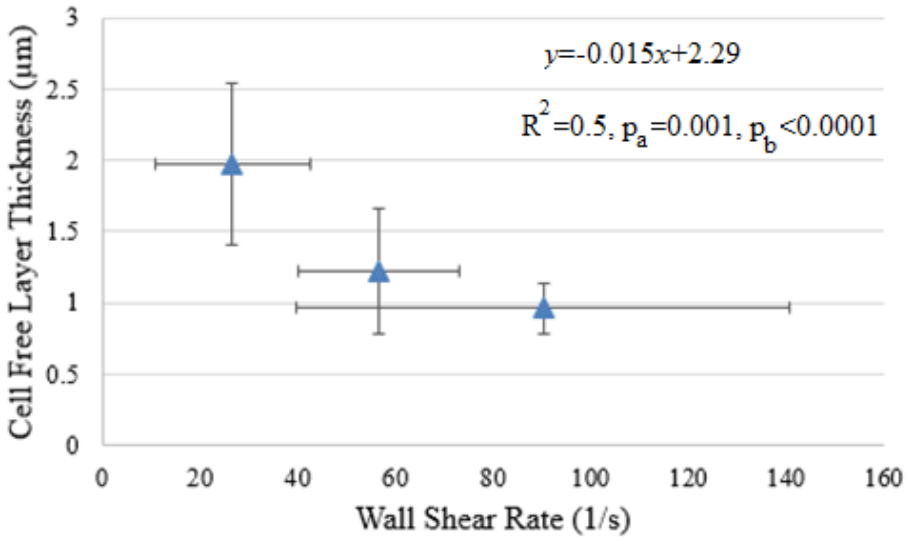

Figure 6.12: The CFL thickness as a function of the measured wall shear rate γ_w, for 10% H blood flowing in straight PDMS microchannels of 34 µm x 100 µm cross-section, using different blood samples. R^2 is the coefficient of determination, p_a and p_b are the probabilities for the slope and the intersect of the regression line, respectively.

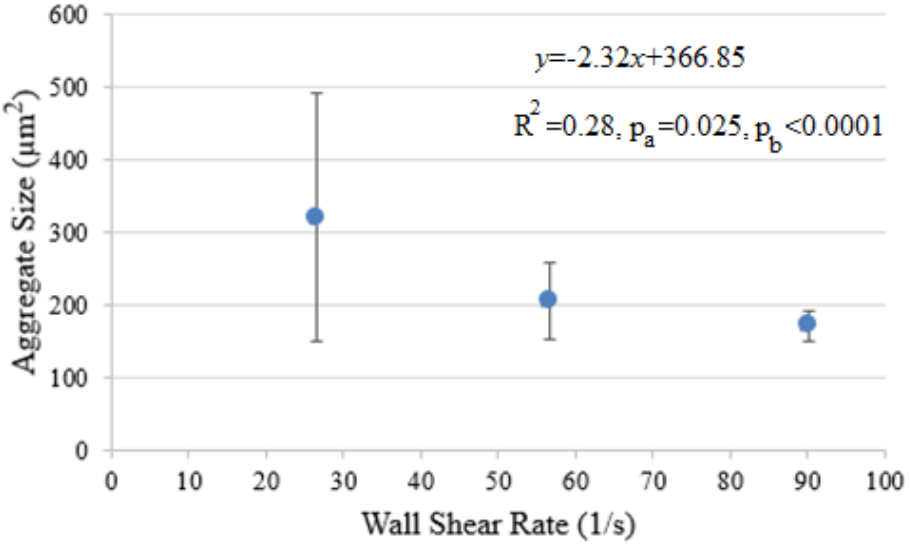

Figure 6.13: The RBC aggregate size as a function of the measured wall shear rate γ_w, for 10% H blood flowing in straight PDMS microchannels of 34 µm x 100 µm cross-section, using different blood samples. R^2 is the coefficient of determination, p_a and p_b are the probabilities for the slope and the intersect of the regression line, respectively.

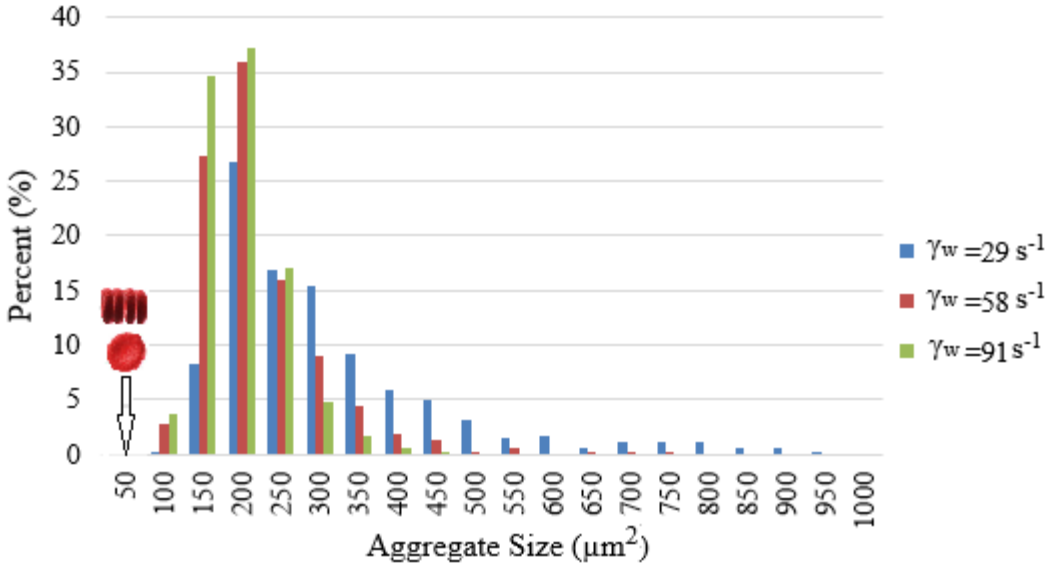

Figure 6.14: The average aggregate size distribution for 10% H blood flowing under different wall shear rates γ_w (s^{-1}). The results was averaged from 35-45 tests, using six different blood samples. For reference, the 50 μm^2 bin corresponds to either the size of a single typical RBC, viewed from its planform area, or that of approximately 4 RBCs aggregating together, viewed from their sides.

These results are in good agreement with the previous studies: Mehri et al. 2013 concluded that larger aggregate sizes are formed at lower shear rates [34] and the findings of Ong et al. 2010 and Maeda et al. 1996 confirmed that RBC aggregation enhances the CFL formation adjacent to the wall, when comparing aggregating and non-aggregation blood [5,7]. The results presented here (Figures 6.12 - 6.14) provide quantitative information on the RBC aggregate size and the associated width of the CFL as well as their relation with the wall shear rate.

6.3 Conclusion

In this chapter, the velocity profile measurements were obtained using µPIV. DI water and 10% H human blood samples were seeded with fluorescent particles, which enabled performing the velocity measurements close to the wall from which the wall shear rates were estimated. DI water was used as a Newtonian reference fluid to ensure the accuracy of the measurements when using non-Newtonian 10% H blood. First, the velocity profile measurements were used to calculate the actual flow rate, which was lower than the programmed flow rate due to the system compliance and deformation of the PDMS microchannels. Then, the shear rate distribution within the microchannel was calculated in order to determine the shear rate at the wall. The shear rate was

maximum at the location closest to the wall and reduced toward the microchannel center, however, when using 10% H blood the presence of CFL produced lower wall shear rate than the theoretical case for Newtonian fluid. The measured velocity profiles were characterized using the shape factor and the skewness parameters for different flow rates and for straight and bifurcating microchannel geometries. Lastly, wall shear rates were used to interpret the results from the CFL and the aggregate size measurements, which were performed in the previous chapters (Chapters four and five, respectively). These measurements provided a quantitative information about the blood flow hemodynamics (e.g. the actual flow rate and wall shear rate) and related the wall shear rate to the average RBC aggregate size, elucidating their influence on the CFL formation. This study is the first one to incorporate the theory of droplet migration to elucidate the mechanism of RBC migration and to link the magnitude of the shear rate and the size of the RBC aggregation to the thickness of the CFL formed adjacent to the microchannel walls.

Chapter 7
Conclusions and Recommendations

7.1 Summary of Results

This research studied the behaviour of blood flowing in microchannels of different geometries: one straight microchannel and two bifurcating microchannels, under different flow rates. 10% H blood suspensions were introduced into each microchannel at a constant flow rate using a high precision syringe pump. Microchannels of 100 µm by 34 µm were fabricated from PDMS, which is biocompatible and suitable for making simple and complex geometries.

First, measurements of the cell-free layer (CFL) thickness were performed using micro particle image velocimetry (µPIV) coupled with a high-speed camera, which enabled visualization of the red blood cells (RBCs) core and the microchannel walls, where the CFL zone presents in-between. The high-speed camera images (bright light images) were processed using a customized MATLAB program, which detected the RBC core at the microchannel center and the location of the microchannel walls. The CFL area (between the RBC core and the walls) was calculated, and its average thickness was determined.

Second, measurements of the RBC aggregate size were performed for the same flow rates and same geometries. The bright light images were used to detect the RBC aggregates based on their projected area using a custom-made MATLAB program.

Last, measurements of the blood flow velocity profile were performed using micro particle image velocimetry (µPIV). For these measurements, the working fluid was seeded with fluorescent particles. The movement of these particles was recorded using a CCD camera. The fluorescent images ware processed with cross-correlation to determine the particles displacement, which was averaged in space and time to determine the velocity profile. The velocity profile was then used to deduce the actual flow rate, the central maximum velocity and the shear rate.

All three measurements (CFL thickness, RBC aggregate size and velocity profile) were each performed at three different flow rates: 6 µl/hr, 12 µl/hr, and 18 µl/hr, which were programmed by the syringe pump. Six blood samples, from six different adult volunteers, were used for the CFL and aggregate size studies, and five blood samples, also from different adult volunteers, were used for the velocity measurements.

These experimental measurements provided quantitative results of the CFL thickness, RBC aggregate size and wall shear rate at a range of physiological flow rates and hematocrit that occur in the microcirculation.

From this work, the influence of flow rate on the blood flow characteristics (CFL formation, RBC aggregate size and shear rate) was investigated, and the direct comparison between different microchannel geometries clarified the effect of microchannel geometries on these characteristics.

The CFL thickness was plotted as a function of flow rate. In the straight channel, the cell-free layer thickness on the opposing sides of the microchannel was effectively symmetric for all employed flow rates and, therefore, the average thickness between both sides provided a good approximation. The blood flow rate was found to have a significant effect on the formation of the CFL adjacent to the vessel or microchannel wall. Increasing the flow rate lead to a reduction in the thickness of the CFL. This decrease in the CFL could enhance the exchange and delivery rate in some applications such as in blood oxygenation either *in vivo* or in an extracorporeal membrane oxygenation device, and in organs-on-a-chip *in vitro*.

No significant influence of the microchannel geometry on the average CFL thickness was found when comparing the results obtained in the straight microchannel and in the two bifurcating microchannels, upstream and downstream of the bifurcations. Branched and interconnected microchannel networks, however, can be beneficial *in vivo* and *in vitro* by providing alternate flow paths, in the event of a channel blockage, and also by increasing fluid mixing. At the bifurcation, the RBCs flowed close to the inner wall of the bifurcation, resulting in an undetectable CFL at the inner wall and a larger CFL at the outer wall of the branch. This asymmetrical variation of the CFL was attributed to an uneven distribution of RBCs (hematocrit) within the branches.

The results also showed that the aggregation indices (AI) of the whole blood samples were correlated with the CFL thickness, which was attributed to the associated increase in the RBC aggregation with AI. Further investigation of the CFL formation and its relation with RBC aggregation was made to clarify this observed trend.

To quantify the effect of the RBC aggregation on the CFL formation, measurements of the RBC aggregate size were performed, for the different flow rates and different microchannel geometries. It was found that the blood flow rate was the main factor that affected RBC aggregation. At low flow rate, RBCs formed aggregates of large sizes due to the reduced shear rate which allowed RBCs to bridge together. By increasing the flow rate, the RBC aggregate size was

reduced, of course, due to the increase in the associated shear rate, which caused aggregates to break up and prevented new ones to form. This reduction in the RBC aggregate size was significant when increasing the flow from the lowest to the highest flow rate for all of the microchannel geometries used herein. It was hypothesized that the RBC aggregation may be affected by the vessel geometry; i.e. in our case, by the bifurcation. The results, however, showed that the microchannel bifurcation has no significant influence on the RBC aggregate size when comparing the aggregates upstream and downstream of the bifurcation to those in the straight microchannel. However, at the lower flow rate, it was clearly seen that the average aggregate size was reduced after the bifurcating when compared to upstream of the bifurcation, which indicated that the presence of the bifurcation caused the aggregates to break apart, whereas, at the increased flow rates, the aggregate sizes were already small, hence no obvious difference could be seen.

The RBC aggregation results were correlated to the measured thickness of the CFL, under the same flow condition and same microchannel geometries. The quantitative measurements of the RBC aggregate size and the CFL thickness revealed an evident relationship that the larger aggregate sizes resulted in larger CFL thickness near the microchannel wall. These results confirm the theory that the migration of particles away from the wall towards the centerline is correlated with the applied shear rate and the particles' size [43]. It is important to note that in blood rheology, the increase in the shear rate reduces the RBC aggregation, thus reducing the size of the RBC aggregates which consequently diminished the thickness of the CFL adjacent to the wall.

The velocity profile measurements were performed using DI water (as a reference Newtonian fluid) and the 10% H blood which is considered as a non-Newtonian fluid at the micro-scale. Different whole blood samples have different protein concentrations, different hematocrits and hence different properties. The velocity profiles of the Newtonian fluid were used as a reference to ensure the measurement accuracy. The use of fluorescent particles as tracers allowed for accurate shear rate measurements at the wall. First, the velocity profiles were used to calculate the actual flow rate, this calculated flow rate (Q_{calc}) was lower than the programmed flow rate by the syringe pump (Q_{prog}), for both fluids (DI water and 10% H blood). This variance in the flow rate was due to the system compliance and PDMS microchannels deformation. Plotting the measured velocity profiles and the Newtonian theoretical velocity profiles produced using the calculated flow rates (Q_{calc}) showed a good agreement for both fluids, which confirmed the measurement accuracy, i.e. the accuracy of the calculated flow rate. The shear rate distribution within the channels was plotted

versus the channel width. As expected, the shear rate was reduced toward the microchannel center. In case of the 10% H blood, lower shear rate was measured at the walls when compared with the theoretical profiles for Newtonian fluid. This was attributed to the formation of the CFL adjacent to the walls, where the velocity gradient within this CFL is much less than in the RBC core.

The velocity profiles were characterized by the shape factor (k) and skewness (S). It was found that the microchannel cross-section was the main determinant affecting the velocity profile shape at this scale and flow rates. For all cases the velocity profiles were relatively blunt with $k > 2$ (where k for a parabolic profile =2). The average skewness of the velocity profiles, in the straight parts of the microchannels, was less than 5%, which considered close to the theoretical case, while within the bifurcation the velocity profile was skewed up to 16% toward the inner wall. This was, in part, due to the upstream condition, in which the velocity of the RBC core was maximum at the center of the mother channel. At the bifurcation, the RBC core divided resulting in an uneven RBC distribution within each branch, with the highest concentration of RBCs (maintaining their higher velocity) located close to the inner wall. The velocity profile, however, retrieved the symmetric shape downstream after the bifurcation.

Finally, the actual flow rate ($Q_{calc.}$) and the wall shear rate results were related to the measurements of the CFL thickness and RBC aggregate size. Both CFL thickness and aggregate size were significantly reduced with increasing flow rate and shear rate. This can be explained using the theory for droplet migration which defined two opposing effects: 1) the lift forces acting on the cells driving them to inward migration, where $u_{mig} \propto \gamma^2 * r^4 / y^2$, and 2) cell-cell interaction that increases cell dispersion and movement towards the wall, where $D \propto \gamma * r^2$ [43].

Under low shear rate conditions and in the presence of the plasma proteins such as fibrinogen or dextran, RBCs are able to stack together forming aggregates or rouleaux. The aggregation process results in an increase in the effective particle size of the cell clusters (i.e. increase in their radius r), these cells then experience stronger lift forces that drive them away from the wall toward the center of the microchannel. This inward migration engendered larger CFL near the wall.

The increase in the flow rate naturally resulted in increased shear rate, which reduces the chance for the neighbouring RBCs to stack together and also causes the large aggregates to break up reducing the particle size. This reduction in the size lowers the inward migration and results in a reduced CFL. Furthermore, this increase in the shear rate also increases the collisions between RBCs which cause cells to move away from the center and towards the walls [5], reducing the

CFL thickness. Based on this findings, the effects of the shear rate on the CFL would be dependant on the range of shear rate experienced by the cells, taking into account the effect of RBC aggregation.

7.2 Summary of Contributions

The outcomes of this experimental work contribute to improving the understanding of blood flow behaviour under physiological conditions found in the microcirculation. In particular, the findings provide clarification and insights into the influence of the blood flow rate and microchannel geometry or bifurcation on blood flow characteristics (e.g., RBC aggregation and CFL formation). Both RBC aggregation and CFL formation are flow rate and geometry dependent. RBC aggregation, which is strongly influenced by the shear rate, affects the RBC migration, CFL thickness and hence the local viscosity of blood in microvessels. The CFL directly contributes to the exchange process between the flowing RBCs and the surroundings tissues, as it is a barrier between the RBC core and the vessel walls. The condition where the CFL is minimum is preferred, as this reduces the distance between the flowing RBCs and the surrounding cells or tissues and enhances the exchange rate.

This is the first study that provides quantitative information and links the CFL thickness and RBC aggregate size for blood flowing into straight and bifurcating microchannels, over a range of physiological hematocrits and flow rates occuring in microcirculation. It was important to match these conditions at which some important blood phenomenon, such as RBC aggregation, only occur [73].

The major accomplishments of this work are:

1- Quantifying the effect of flow rate on CFL thickness in microchannels of straight and bifurcating geometries.
2- Quantifying the microchannel geometry influence on CFL formation.
3- Quantifying the flow rate influence on RBC aggregate size of flowing blood into the same geometries used in CFL measurements.
4- Quantifying the microchannel geometry influence on RBC aggregate size.
5- Relating the measured aggregate size to CFL thickness for a range of flow rate.
6- Correlating CFL thickness and RBC aggregate size to the wall shear rate.

These findings provided measured values for the CFL at the micro-level and at physiological conditions of flow rate and hematocrit. Figure 7.1 illustrates the CFL results from this study and previous studies.

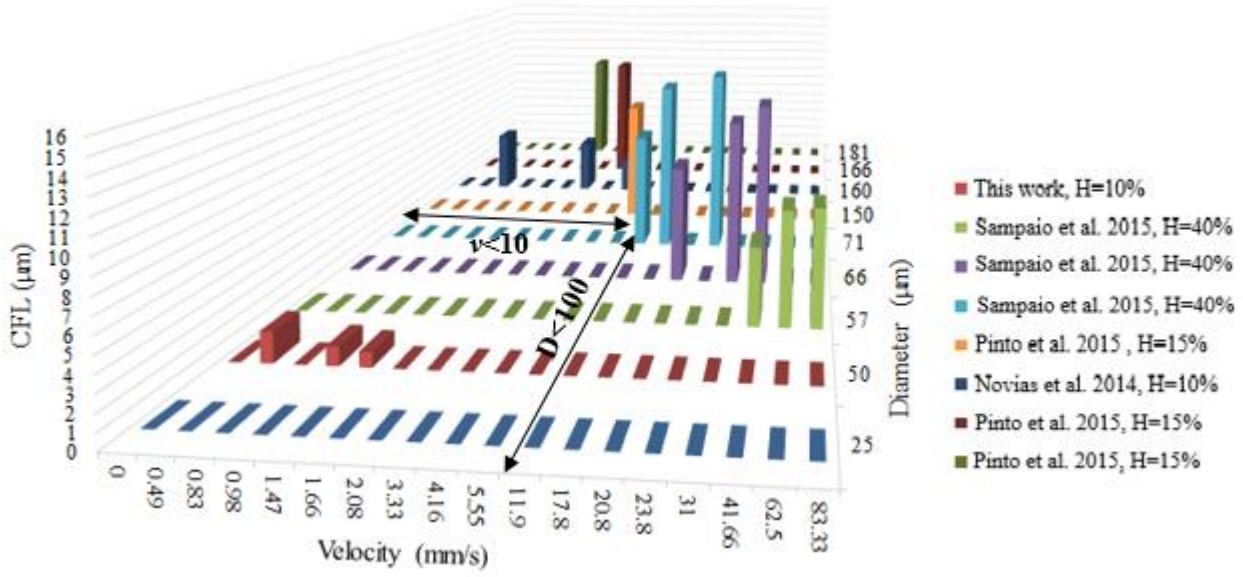

Figure 7.1: The CFL measurements performed in this work (using 10% H blood flowing into straight microchannels) are compared with previous *in vitro* studies of: Sampaio et al., 2015, Pinto et al., 2015, and Novias et al., 2014. The CFL thickness (µm) is plotted as a function of the average velocity (mm/s) and as a function of the microchannel diameter (µm).

In this work, and for the first time, the shear rate was also measured at the walls and related to CFL thickness and RBC aggregate size. The results showed a significant reduction in CFL thickness and RBC aggregate size when increasing the wall shear rate.

The results improve the understanding of CFL formation in the microcirculation, where the thickness of this layer is comparable to the vessel diameter and therefore CFL influences blood properties, such as viscosity, as well as the physiological processes, such as gas exchange.

Furthermore, the results could be used to enhance the design and performance of microfluidic devices used for medical diagnosis, monitoring or treatment, where the separation of plasma from whole blood is an important step. Results may also aid to develop the design and the performance of some microfluidic applications for research such as lab on a chip and organ on a chip. For example, this research can be used to improve the design and the performance of the artificial lung or blood oxygenator, e.g. the oxygen transfer rate to blood flowing into the microchannels of the device. Also, the results may be used to implement a mathematical model of microcirculation.

7.3 Recommendations for Future Work

This experimental study provided information about the CFL formation developed at the walls of microchannels, the RBC aggregate size and the applied wall shear rate. In particular, this study investigated the influence of the flow rate and microchannel geometries on these parameters.

The set-up used for this research could be used to investigate the effects of flow rate and channel geometry on the oxygen transfer to blood cells. For this, blood suspensions could be exposed to oxygen (indirectly) while passing through the channels, this process known as blood oxygenation. The blood oxygen levels could then be measured at the channel inlet and outlet under varying flow rates and in varying channel geometries. Performing blood oxygenation, using the three different geometries under the three flow rates employed in this work, would allow investigating the influence of the flow rate and the microchannel geometry on the oxygen transfer rate, e.g. blood oxygenation in microfluidic flow.

The CFL measurements and the aggregate size measurements acquired in this present study would help to interpret the results of the blood oxygenation study. The outcome of that study could be used in the development of the design and the performance of some artificial organs (e.g. the artificial lung to improve the blood oxygenation rate).

Another suggestion for future work is the use of a synthetic plasma instead of the autologous plasma (e.g. PBS) for blood flow applications. This would help reduce the variability in the aggregation levels between different blood samples drawn from different volunteers; however, in this case, dextran would have to be added to the blood suspensions in order to induce aggregation (in the absence of aggregation-inducing proteins in the plasma), and this may influence the RBC properties (e.g. size and conformation) [93].

Additionally, increasing the blood hematocrits to a concentration higher than 10% H would improve the exchange rate between RBCs and targeted cells, as the number of RBCs increases. The increase in the hematocrit, however, inherently makes more difficult the visualisation of the CFL and its measurement at the microscale [37,50].

Furthermore, reducing the microchannel width to smaller than 100 μm would make the channel more square (1:1 aspect ratio), which is a closer approximation to the round shape of the capillary.

Also, the size reduction would increase the surface area/volume ratio, which would help in increase the RBC exposure in applications involving exchange of gas, drugs or nutrients.

Further investigation is needed in order to better understand and clarify the variance between the *in vivo* and *in vitro* blood flow phenomena. *In vivo,* the vessels are irregular in shape and diameter, having frequent bifurcations and junctions, which may affect the RBCs' distribution across the vessel. Additionally, the presence of the endothelial cell layer at the inner vessel walls may influence the blood flow *in vivo*, by altering the flow resistance [39].

References

1. Secomb TW. Blood flow in the microcirculation. Annual Review of Fluid Mechanics. 2017;49:443–61.
2. Namgung B, Liang LH, Kim S. Physiological significance of cell-free layer and experimental determination of its width in microcirculatory vessels. Visualization and Simulation of Complex Flows in Biomedical Engineering, Lecture notes in computational vision and biomechanics. 2014;12:75–87.
3. Baskurt OK, Meiselman HJ. Blood rheology and hemodynamics. Seminars in Thrombosis and Hemostasis. 2003;29(5):435–50.
4. Li X, Popel AS, Karniadakis GE. Blood–plasma separation in Y-shaped bifurcating microfluidic channels: a dissipative particle dynamics simulation study. Physical Biology. 2012;9:1–12.
5. Ong PK, Namgung B, Johnson PC, Kim S. Effect of erythrocyte aggregation and flow rate on cell-free layer formation in arterioles. AJP- Heart and Circulatory Physiology. 2010;298(6):H1870–8.
6. Kim S, Kong RL, Popel AS, Intaglietta M, Johnson PC. Temporal and spatial variations of cell-free layer width in arterioles. American journal of Physiology, Heart and circulatory Physiology. 2007;293(3):H1526–35.
7. Maeda N, Suzuki Y, Tanaka J, Tateishi N. Erythrocyte flow and elasticity of microvessels evaluated by marginal cell-free layer and flow resistance. The Amerecan Physiology Society. 1996;H2454–61.
8. Novais S, Pinho D, Bento D, Pinto E, Yaginuma T, Fernandes CS, et al. Cell-free layer measurments in complex geometries: contractions and bifurcations. Visualization and Simulation of Complex Flows in Biomedical Engineering, Lecture notes in computational vision and biomechanics. 2014;12:119–32.
9. Ishikawa T, Fujiwara H, Matsuki N, Yoshimoto T, Imai Y, Ueno H, et al. Asymmetry of blood flow and cancer cell adhesion in a microchannel with symmetric bifurcation and confluence. Biomedical Microdevices. 2011;13(1):159–67.
10. Pinto E, Faustino V, Rodrigues RO, Pinho D, Garcia V, Miranda JM, et al. A rapid and low-cost nonlithographic method to fabricate biomedical microdevices for blood flow analysis. Micromachines. 2015;6(1):121–35.

11. Mielczarek WS, Obaje EA, Bachmann TT. Microfluidic blood plasma separation for medical diagnostics : is it worth it ? Lab on a Chip. Royal Society of Chemistry; 2016;16:3441–8.
12. Aleksander S. Popel, Johnson PC. Microcirculation and hemorheology. Fluid Mechanics. 2005;37:43–69.
13. Lee Waite, Fine J. Applied Biofluid Mechanics. New York: McGraw-Hill; 2007.
14. Chandran KB, Yoganathan AP, Rittgers SE. Biofluid Mechanics: The Human Circulation. CRC Press, editor. Boca Raton, Florida: Taylor & Francis Group; 2007.
15. Pries AR, Fritzsche A, Ley K, Gaehtgens P. Redistribution of red blood cell flow in microcirculatory networks by hemodilution. Circulation Research. 1992;70(6):1113–21.
16. Wong KHK, Chan JM, Kamm RD, Tien J. Microfluidic models of vascular functions. Annual Review of Biomedical Engineering. 2012;14:205–30.
17. Kaliviotis E, Sherwood JM, Balabani S. Partitioning of red blood cell aggregates in bifurcating microscale flows. Scientific Reports. 2017;7(44563):1–13.
18. Hysi E, Saha RK, Kolios MC. Simultaneous photoacoustic detection of red blood cell aggregation and oxygenation. IEEE International Ultrasonics Symposium Proceedings. 2012;1398–401.
19. Baskurt O, Neu B, Meiselman HJ. Red Blood Cell Aggregation. Taylor& Fr. FL: CRC Press; 2011.
20. Vennemann P, Lindken R, Westerweel J. In vivo whole-field blood velocity measurement techniques. Experiments in Fluids. 2007;42:495–511.
21. Sherwood JM, Kaliviotis E, Dusting J, Balabani S. Hematocrit, viscosity and velocity distributions of aggregating and non-aggregating blood in a bifurcating microchannel. Biomechanics and Modeling in Mechanobiology. 2012;1–15.
22. Fuerstman MJ, Lai A, Thurlow ME, Shevkoplyas SS, Stone A, Whitesides GM. The pressure drop along rectangular microchannels containing bubbles. The Royal Society of Chemistry. 2007;1479–89.
23. Fung Y. C. Biomechanics Circulation. 2nd ed. New York: Springer- Verlag; 1997.
24. Sia SK, Whitesides GM. Microfluidic devices fabricated in poly(dimethylsiloxane) for biological studies. Electrophoresis. 2003;24:3563–76.
25. Tateishi N, Maeda N, Shiga T. A method for measuring the rate of oxygen release from

single microvessels. Circulation Research. 1992;70(4):812–9.

26. Lipowsky HH. Microvascular rheology and hemodynamics. Microcirculation. 2005;12:5–15.
27. Radenovic A. Microfluidics lab on chip. Advanced Bioengineering Methods Laboratory Microfluidics Lab on Chip. :1–27.
28. Yang B, Wang Y, He W. Application of micro-PIV on the microscale flow and a modified system based on ordinary 2-D PIV. Advanced Materials Research Vol. 2012;346:657–63.
29. Potkay JA. A high efficiency micromachined artificial lung. Transducers. 2009;2234–7.
30. Potkay JA, Magnetta M, Vinson A, Cmolik B. Bio-inspired , efficient , artificial lung employing air as the ventilating gas. The Royal Society of Chemistry. 2011;11:2901–9.
31. Lima R, Wada S, Tanaka S, Takeda M, Tsubota K. Velocity measurements of blood flow in a rectangular PDMS microchannel assessed by confocal micro-PIV system. :278–81.
32. Zhou J, Ellis AV, Voelcker NH. Recent developments in PDMS surface modification for microfluidic devices. Electrophoresis. 2010;31:2–16.
33. Lima R, Wada S, Tanaka S, Takeda M, Ishikawa T. In vitro blood flow in a rectangular PDMS microchannel: experimental observations using a confocal micro-PIV system. Biomedical Microdevices. 2008;10(2):153–67.
34. Mehri R, Laplante J, Mavriplis C, Fenech M. Investigation of blood flow analysis and red blood cell aggregation. Journal of Medical and Biological Engineering. 2013;34(5):469–74.
35. Pitts KL, Fenech M. High speed versus pulsed images for micro-particle image velocimetry : a direct comparison of red blood cells versus fluorescing tracers as tracking particles. Physiological Measurement. 2013;34:1363–74.
36. Kuang C, Zhao W, Yang F, Wang G. Measuring flow velocity distribution in microchannels using molecular tracers. Microfluid Nanofluid. 2009;7:509–17.
37. Garcia V, Dias R, Lima R. In vitro blood flow behaviour in microchannels with simple and complex geometries. Applied Biological Engineering- Principles and practice. 2012;393–417.
38. Fedosov DA, Caswell B, Popel AS, Karniadakis GE. Blood flow and cell-free layer in microvessels. Microcirculation. 2010;17(8):615–28.
39. Katanov D, Gompper G, Fedosov DA. Microvascular blood flow resistance : Role of red blood cell migration and dispersion. Microvascular Research. 2015;99:57–66.

40. Secomb TW, Pries AR. Blood viscosity in microvessels : Experiment and theory. Comptes Rendus Physique. Elsevier Masson SAS; 2013;14(6):470–8.
41. Basu H, Dharmadhikari AK, Dharmadhikari JA, Sharma S, Mathur D. Tank treading of optically trapped red blood cells in shear flow. Biophysical. 2011;101(7):1604–12.
42. Hariprasad DS, Secomb TW. Two-dimensional simulation of red blood cell motion near a wall under a lateral force. physical Review. 2014;90:53014-1-053014–7.
43. Hudson SD. Wall migration and shear-induced diffusion of fluid droplets in emulsions. Physics of Fluids. 2003;15(5):1106–13.
44. Bishop JJ, Popel AS, Intaglietta M, Johnson PC. Rheological effects of red blood cell aggregation in the venous network : a review of recent studies. Biorheology. 2001;38:263–74.
45. C.G. Caro, Pedley TJ, Schroter RC, Seed WA. The Mechanics of the Circulation. 2nd ed. Cambridge, United Kingdom: Cambridge University Press; 2011.
46. Kim S, Ong PK, Yalcin O, Intaglietta M, Johnson PC. The cell-free layer in microvascular blood flow. Biorheology. 2009;46:181–9.
47. Goldsmith H. Red cell motions and wall interactions in tube flow. Federation Proceedings. 1971;30(5):1578–88.
48. Tina Rieper, Paul Cvancara, Claas Muller HR. Simplified analysis method of cell-free layers in blood flows as tool for the optimization of gas exchange devices. Microfluid Nanofluid. 2014;17:1071–8.
49. Sampaio D, Lopes D, Semiao V. Horse and dog blood flows in PDMS rectangular microchannels: experimental characterization of the plasma layer under different flow conditions. Experimental Thermal and Fluid Science. Elsevier Inc.; 2015;68:205–15.
50. Lauri J, Bykov A, Fabritius T. Quantification of cell-free layer thickness and cell distribution of blood by optical coherence tomography layer thickness and cell. 2016;21(4).
51. Sherwood JM, Dusting J, Kaliviotis E, Balabani S. The effect of red blood cell aggregation on velocity and cell-depleted layer characteristics of blood in a bifurcating microchannel. Biomicrofluidics. 2012;6(24119):1–18.
52. Cerdeira T, Lima R, Oliveira M, Tshikawa T, T Y. Determination of the cell-free layer in circular PDMS microchannels. 2010;40–3.
53. Pinto E, Taboada B, Rodrigues R, Faustino V, Pereira A, Lima R. Cell-free layer (CFL)

analysis in a polydimethysiloxane (PDMS) microchannel : a global approach. WebmedCentral. 2013;4(8):1–20.

54. Lima R, Oliveira MSN, Ishikawa T, Kaji H, Tanaka S, Nishizawa M, et al. Axisymmetric polydimethysiloxane microchannels for in vitro hemodynamic studies. Biofabrication. 2009;1(3):1–7.
55. Kim S, Kong RL, Popel AS, Intaglietta M, Johnson PC. A computer-based method for determination of the cell-free layer width in microcirculation. Microcirculation. 2006;13:199–207.
56. Ong PK, Jain S, Namgung B, Woo YI, Sakai H, Lim D, et al. An automated method for cell-free layer width determination in small arterioles. Physiological Measurement. 2011;32:N1–12.
57. Baskurt OK, Meiselman HJ. Erythrocyte aggregation : basic aspects and clinical importance. Clinical Hemorheology and Microcirculation. 2013;53:23–37.
58. Popel AS, Johnson PC, Kamemeva M V., Wild MA. Capacity for red blood cell aggregation is higher in athletic mammalian species than in sedentary species. The American physiological Society. 1994;0161–7567:1790–4.
59. A clasic, gold standard: The Westergren method for ESR meassurement. RR Mechatronics Masters of Measurment. 2015;
60. Chien S and Jan K. Ultrastructural basis of the mechanism of rouleaux formation. Microvascular Research. 1973;5(2):155–66.
61. Shuqi C, Gregory B, Benjamin G, Yona M, Saul Y. Monitoring of red blood cell aggregability in a flow-chamber by computerized image analysis. Clinical Hemorehology and Microcirculation. 1994;14(4):497–508.
62. Jayavanth S, Singh M. Computerized analysis of erythrocyte aggregation from sequential video-microscopic images under gravitational sedimentation. Science Direct. 2004;25:67–74.
63. Foresto P, Arrigo MD, Carreras L, Cuezzo RE, Valverde J, Rasia R. Evaluation of red blood cell aggregation in diabetes by computarized image analysis. Medicina. 2000;60:570–2.
64. Shin S, Yang Y, Suh JS. Measurement of erythrocyte aggregation in a microchip stirring system by light transmission. Clinical Hemorheology and Microcirculation.

2009;41(3):197–207.

65. Tuma RF, Duran WN, Ley K. Microcirculation. 2nd ed. Oxford, UK; 2008.
66. Anastasiou AD, Spyrogianni AS, Paras S V. Experimental study of pulsatile blood flow in micro channels. International Congress of Chemical and Process Engineering. 2010;1–17.
67. Papaioannou TG, Stefanadis C. Vascular wall shear stress : basic principles and methods. Hellenic Journal of Cardiology. 2005;46:9–15.
68. Tangelder GJ, Slaaf DW, Muijtjens AMM, Arts T, Egbrink MGA oude, Reneman RS. Velocity profiles of blood platelets and red blood cells flowing in arterioles of the rabbit mesentery. Circulation Research. 1986;59(5):505–15.
69. Tangelder GJ, Slaaf DW, Arts T, S.Reneman R. Wall shear rate in arterioles in vivo : least estimates from platelet velocity profiles. Heart and Circulatory Physiology. 1988;254:H1059–64.
70. Sheriff J, Bluestein D, Girdhar G, Jesty J. High-shear sensitized platelets to subsequent low-shear condition. Annual review of biomedical engineering. 2010;38(4):1442–50.
71. Grobelnik B. Blood flow. University in Ljubljana- Faculty of Mathematics and Physics. 2008;1–17.
72. Mielnik MM, Saetran LR. Micro particle image velocimetry – an overview. :1–8.
73. Bishop JJ, Nance PR, Popel AS, Intaglietta M, Johnson PC. Effect of erythrocyte aggregation on velocity profiles in venules. Heart and Circulatory Physiology. 2001;280:H222-236.
74. Williams SJ, Park C, Wereley ST. Advances and applications on microfluidic velocimetry techniques. Microfluid Nanofluid. 2010;8:709–26.
75. Incropeera FP, DeWett DP, Bergman TL, Lavine AS. Introduction to Heat Transfer. 5th ed. USA: John Wiley& Sons; 2007.
76. Vollmer AP, Probstein RF, Gilbert R, Thorsen T. Development of an integrated microfluidic platform for dynamic oxygen sensing and delivery in a flowing medium. The Royal Society of Chemistry. 2005;5:1059–66.
77. Kniazeva T, Epshteyn AA, Hsiao JC, Kim ES, Kolachalama VB, Charest JL, et al. Performance and scaling effects in a multilayer microfluidic extracorporeal lung oxygenation device. The Royal Society of Chemistry. 2012;12:1686–95.
78. Negative tone photoresist formulations 2-25. Micro Chem. :1–4.

79. Kniazeva T, Hsiao JC, Charest JL, Borenstein JT. A microfluidic respiratory assist device with high gas permeance for artificial lung applications. Biomed Microdevices. 2011;13:315–23.
80. Burgess KA, Hu H, Wagner WR, Federspiel WJ. Towards microfabricated biohybrid artificial lung modules for chronic respiratory support. Biomed Microdevices. 2009;11:117–27.
81. Lee J, Kung M, Kung H, Mockros L. Microchannel technologies for artificial lungs: (3) open rectangular channels. American Society for Artificial Internal Organs. 2008;54(4):390–5.
82. Sreenivasan R, Bassett EK, Hoganson DM, Vacanti JP, Gleason KK. Biomaterials ultra-thin , gas permeable free-standing and composite membranes for micro fl uidic lung assist devices. Biomaterials. Elsevier Ltd; 2011;32(16):3883–9.
83. Pitts KL, Mehri R, Mavriplis C, Fenech M. Micro-particle image velocimetry measurement of blood flow : validation and analysis of data pre-processing and processing methods. Measurment Science and Technology. 2012;23:1–9.
84. Wereley ST, Meinhart CD. Recent advances in micro-particle image velocimetry. The annual Review of Fluid Mechanics. 2010;42:557–76.
85. Tabeling P. Introduction to Microfluidics. Oxford, UK: Oxford University Press; 2005.
86. Beebe DJ, Mensing GA, Walker GM. Physics and applications of microfluidics in biology. The Annual Review of Biomedical Engineering. 2002;4:261–86.
87. Son Y. Determination of shear viscosity and shear rate from pressure drop and flow rate relationship in a rectangular channel. Polymer. 2007;48:632–7.
88. Yalcin O, Wang Q, Johnson PC, Palmer AF, Cabrales P, Lowrie WG. Plasma expander viscosity effects on red cell-free layer thickness after moderate hemodilution. Biorheology. 2011;48(2011):277–91.
89. Chayer B, Pitts KL, Cloutier G, Fenech M. Velocity measurement accuracy in optical microhemodynamics : experiment and simulation. 2012;33:1585–602.
90. Hardy BS, Uechi K, Zhen J, Kavehpour HP. The deformation of flexible PDMS microchannels under a pressure driven flow. Lab on a Chip. 2009;935–8.
91. Hademenos GJ, Massoud TF. Biophysical mechanisms of stroke. Stroke. 1997;28(10):1–32.
92. Yang XL, Liu Y, So RMC, Yang JM. The effect of inlet velocity profile on the bifurcation

COPD airway flow. Computers in Biology and Medicine. 2006;36:181–94.

93. Xu X, Wang RK, Elder JB, Tuchin V V. Effect of dextran-induced changes in refractive index and aggregation on optical properties of whole blood. Physics in medicine and biology. 2003;48(9):1205–21.

Appendix

Appendix: A

Table A1: Literature data of CFL measurements *in vitro* [8–10,49].

Paper/reference	Figure	Blood type	Vessel shape	Plasma type	Aggregation	Syudy in	Hematocrit (H)	Width (w)	Hight (h)	Hydrolic diameter (D_h)	Flow rate (Q)	Velocity ($v=Q/Area$)	Shear rate ($\gamma=v/D_h$)	Wall Shear rate ($\gamma_w=3Q/2w*h^2$)	CFL	CFL/radius
							%	µm	µm	µm	µl/hr	mm/s	1/s	1/s	µm	%
Pinto 2015	10	Ovine	Rectangular	Saline	Dextran 40	*In vitro*	5	300	100	150	600	5.5	37.0	83	12.9	17.3
								500	100	166.6	600	3.3	20	50	11.7	14.1
								1000	100	181.8	600	1.6	9.1	25	16.7	18.4
							10	300	100	150	600	5.5	37.0	83	9.6	12.8
								500	100	166.6	600	3.3	20	50	10.8	13.0
								1000	100	181.8	600	1.6	9.1	25	10.0	11.0
Ishikawa	5	Human	Rectangular	Saline	Dextran 40	*In vitro*	10	75	40	52.1	3.6	0.33	6.38	12.5	4.1	15.7
Novias 2014	7	Sheep	Rectangular	Buffer	Dextran 40	*In vitro*	5	400	100	160	120	0.8	5.2	12.5	8.2	10.3
								400	100	160	300	2.0	13.0	31.2	5.5	6.9
								400	100	160	600	4.1	26.0	62.5	6.4	8.0
							10	400	100	160	120	0.8	5.2	12.5	4.8	6.0
								400	100	160	300	2.0	13.0	31.2	4.1	5.1
								400	100	160	600	4.1	26.0	62.5	2.8	3.5
							15	400	100	160	120	0.8	5.2	12.5	4.8	6.0
								400	100	160	300	2.0	13.0	31.2	4.1	5.1
								400	100	160	600	4.1	26.0	62.5	2.8	3.5
Sampaio 2015	8	Horse	Rectangular			*In vitro*	40	100	40	57.1	600	41.6	729	1562	5.2	18.4
								100	40	57.1	900	62.5	1093	2343	7.3	25.7
								100	40	57.1	1200	83.3	1458	3125	7.7	27.0
								200	40	66.6	600	20.8	312	781	8.0	24.1
								200	40	66.6	900	31.2	468	1171	11.6	35.0
								200	40	66.6	1200	41.6	625	1562	12.6	37.9
								350	40	71.7	600	11.9	165	446	8.6	24.0
								350	40	71.7	900	17.8	248	669	12.5	34.9
								350	40	71.7	1200	23.8	331	892	13.5	37.8

Table A2: Literature data of CFL measurements *in vitro* [48–52].

Paper/reference	Figure	Blood type	Vessel shape	Plasma type	Aggregation	Syudy in	Hematocrit (H)	Width (w)	Hight (h)	Hydrolic diameter (D_h)	Flow rate (Q)	Velocity ($v=Q/Area$)	Shear rate ($\gamma=v/D_h$)	Wall Shear rate ($\gamma_w=3Q/2w*h^2$)	CFL	CFL/radius
							%	µm	µm	µm	µl/hr	mm/s	1/s	1/s	µm	%
Sampaio 2015	9	Dog	Rectangular			*In vitro*	45	160	40	64	27.6	1.19	18.7	44.9	4.1	13.1
								160	40	64	58.0	2.51	39.3	94.4	4.3	13.6
								160	40	64	302	13.1	204	491	4.9	15.3
								160	40	64	599	26.0	406	975	5.7	17.8
								160	40	64	1194	51.8	810	1944	6.4	20.1
								160	40	64	1797	78.0	1219	2926	6.2	19.5
Rieper 2014	11	Human	Rectangular	Saline		*In vitro*	20	1000	100	181.8	36000	100	550	1500	0	0
								1000	100	181.8	48240	134	737	2010	1.9	2.1
								1000	100	181.8	60120	167	918.5	2505	1.9	2.1
								1000	100	181.8	72000	200	1100	3000	2.4	2.6
								1000	100	181.8	84240	234	1287	3510	2.4	2.6
Rieper 2014	12	Human	Rectangular	Saline		*In vitro*	25	1000	100	181.8	36000	100	550	1500	0	0
								1000	100	181.8	48240	134	737	2010	0	0
								1000	100	181.8	60120	167	918.5	2505	0.89	0.98
								1000	100	181.8	72000	200	1100	3000	0.89	0.98
								1000	100	181.8	84240	234	1287	3510	1.5	1.6
Cerdeira 2009	5	Human	Circual		Dextran 40	*In vitro*	3			73	3.0	0.2	2.73	5.75	22.3	61.3
							13			73	3.0	0.2	2.73	5.75	11.6	31.9
							23			73	3.0	0.2	2.73	5.75	10.1	27.7
							37			73	3.0	0.2	2.73	5.75	6.1	16.7
Lauri 2016	1	Human	Rectangular	PBS		*In vitro*	45	2000	200	363.6	100	0.06	0.19	0.52	11.6	6.3
								2000	200	363.6	200	0.13	0.38	1.04	5.9	3.2
								2000	200	363.6	300	0.2	0.57	1.56	4.9	2.7
								2000	200	363.6	400	0.27	0.76	2.08	4.7	2.6
								2000	200	363.6	500	0.34	0.95	2.6	3.5	1.9
Sherwood 2012	12	Human	Rectangular	PBS	Dextran 2000	*In vitro*	25	100	40	57.1	3.5	0.24	4.2	9.11	18	63
								100	40	57.1	3.5	0.24	4.2	9.11	8	28

Table A3: Literature data of CFL measurements *in vivo* [5–7].

Paper/reference	Figure	Blood type	Vessel shape	Plasma type	Aggregation	Syudy in	Hematocrit (H)	Width (w)	Hight (h)	Hydrolic diameter (D_h)	Flow rate (Q)	Velocity ($v=Q/Area$)	Shear rate ($\gamma=v/D_h$)	Wall Shear rate ($\gamma_w=3Q/2w*h^2$)	CFL	CFL/radius
							%	µm	µm	µm	µl/hr	mm/s	1/s	1/s	µm	%
Maeda 1996	4	Human in rabbit	Circular			*In vivo*	16			9.0		1	109.9	230.8	1.1	25.4
										13.2			75.7	159.0	1.7	26.4
										17.7			56.3	118.3	2.5	29.2
										25.8			38.7	81.3	3.6	28.5
										35.6			28.0	58.8	4.2	23.6
Maeda 1996	5	Human in rabbit	Circular			*In vivo*	8			30		1	33.3	70	5.3	35.8
							16						33.3	70	4.2	28.3
							30						33.3	70	2.0	13.8
							45						33.3	70	1.1	7.8
Ong 2010	3	Rat	Circular			*In vivo*	40			20-60			318	669		8.7
													135	283		9.55
													17	35.5		10.5
					Dextran 500		38			20-60			318	669		8.5
													135	283		9.2
													17	35.5		13.1
Kim 2007	8	Rat	Circular			*In vivo*	42			72.3		8.6	118	249	2.7	7.4
										49.2			174	366	3.1	12.8
										45.3			189	397	2.3	10.1
										30.8			278	585	2.1	13.6
										25.2			339	713	2.5	20.2
										24.8			345	725	1.8	14.7
										22.2			386	811	1.2	11.3
										15.1			568	1193	1.6	21.5
Kim 2007	8	Rat	Circular		Dextran 500	*In vivo*	41			70.3		6.8	96.5	202	3.2	9.0
										61			111	234	2.2	7.3
										53			128	269	2.3	8.9
										53.8			126	265	2.9	10.7
										31			219	460	2.1	13.5
										22.8			297	624	2	17.4
										19.2			352	741	2.8	29.0
										18.2			373	784	0.93	10.2

Table A4: Literature data of CFL measurements from simulation [4,38,39].

Paper/reference		Blood type	Vessel shape	Plasma type	Aggregation	Syudy in	Hematocrit (H)	Width (w)	Hight (h)	Hydrolic diameter (D_h)	Flow rate (Q)	Velocity ($v=Q/Area$)	Shear rate ($\gamma=v/D_h$)	Wall Shear rate ($\gamma_w=3Q/2w*h^2$)	CFL	CFL/radius
							%	µm	µm	µm	µl/hr	mm/s	1/s	1/s	µm	%
Li 2012	Table 2		Rectangular			simulation	10	40	10	16	0.496	0.344	21.5	51.7	5.4	68.3
							20	40	10	16	0.496	0.344	21.5	51.7	4.1	51.6
							30	40	10	16	0.496	0.344	21.5	51.7	2.7	34.7
							40	40	10	16	0.496	0.344	21.5	51.7	2.1	26.7
Fedosov 2010	Figure 10a & Table 2		Circular			simulation	15			10	0.17	0.61	61	128	2.4	48.2
							30				0.13	0.47	47	98	1.9	39.2
							45				0.08	0.28	28.6	60	1.1	23.7
							15			20	1.3	1.17	58.6	123	4.2	42.2
							30				1.0	0.93	46.6	97	2.7	27.8
							45				0.63	0.56	28.3	59	1.5	15.9
							15			40	10.0	2.23	55.7	117	5.1	25.8
							30				5.2	1.16	29.1	61	3.1	15.9
							45				5.0	1.11	27.7	58	1.7	8.8
Katanov 2015	Figure 7		Circular		No	simulation	15			20			19.0	39.9	4	40
													40.4	84.9	4.4	44.1
													83.3	175	4.6	46.9
													128	270	4.6	46.9
													173	364	4.8	48.1
							30						14.2	29	2.4	24.0
													31.7	66.6	2.8	28.0
													69.0	145	2.9	29.9
													153	321	3.1	31.9
							45						9.5	19.9	1.3	13
													21.4	45	1.3	13.9
													51.5	108	1.7	17.1
													84.1	176	1.8	18
													117	246	1.8	18.8
Katanov 2015	Figure 7		Circular		Yes	simulation	15			20			6.3	13.3	4.7	47.9
													39.6	83.3	4.7	47.9
													84.1	176	4.7	47.9
													175	368	4.9	49.2
							30						15.8	33.3	3	30
													27.7	58.3	3.1	31.8
													33.3	69.9	3.1	31.8
													73.0	153	3.2	32.8
													153	321	3.2	32.9
							45						11.1	23.3	1.7	17.1
													23.8	50	1.8	18
													54.7	115	1.8	18.9
													123.8	260	1.9	19.9